

Ion Migration in Lead Halide Perovskite Solar Cells

Lucie Mc Govern



Ph.D. Thesis, University of Groningen, December 2021

Lucie Mc Govern

Ph.D. Examining Committee:

Prof. L.J.A. Koster

Prof. T. Savenije

Prof. E.L. Von Hauff

Dr. L. Protesescu

Dr. E. Hutter

The work described in this thesis was performed between January 2018 and December 2021 at AMOLF, Science Park 104, 1098 XG Amsterdam, The Netherlands and financed by the Netherlands Organization for Scientific Research (NWO).

Printed by Ridderprint.

Cover design and painting by Dr Nasim Tavakoli, inspired by Rothko.

A digital version of this thesis can be downloaded at <http://amolf.nl>.

ISBN: 978-94-92323-62-0



university of
 groningen

Ion Migration in Lead Halide Perovskite Solar Cells

PhD thesis

to obtain the degree of PhD at the
 University of Groningen
 on the authority of the
 Rector Magnificus Prof. C. Wijmenga
 and in accordance with
 the decision by the College of Deans.

This thesis will be defended in public on

Thursday 28 April 2022 at 16.15 hours

by

Lucie Mc Govern

born on 28 December 1993
 in Paris, France

Supervisors

Prof. B. Ehrler
Prof. E.C. Garnett

Assessment Committee

Prof. L.J.A. Koster
Prof. T. Savenije
Prof. E.L. Von Hauff

CONTENTS

1	Introduction	1
1.1	The role of solar cells in the energy transition	1
1.2	Perovskite solar cells	3
1.3	The issue of extrinsic instability...	6
1.4	... and intrinsic stability, a closer look at ion migration . .	8
1.5	The transient ion drift technique	12
1.6	Outline of this thesis	16
2	The case of MAPbBr₃ versus MAPbI₃ - Suppression of methylammonium migration and reduction of halide migration	19
2.1	Introduction	20
2.2	Results and discussion	21
2.2.1	MAPbBr ₃ solar cell device configuration	21
2.2.2	TID measurement shows bromide migration in MAPbBr ₃	23
2.2.3	Quantification of bromide migration characteristics	24
2.2.4	Comparing ion migration patterns in MAPbBr ₃ and MAPbI ₃	25
2.3	Conclusion	28
2.4	Appendix	29
2.4.1	Solar cell fabrication and performance	29
2.4.2	Capacitance measurements	30
3	A mix of halides - Reduced barrier for ion migration in mixed MAPb(Br_xI_{1-x})₃ perovskites	37
3.1	Introduction	38
3.2	Results and discussion	39
3.2.1	Mixed-halide solar cell fabrication	39
3.2.2	Capacitance measurements of the mixed-halide solar cells	40
3.2.3	Quantification of ion migration characteristics . . .	41
3.3	Conclusion	48

3.4	Appendix	49
3.4.1	Solar cell device fabrication	49
3.4.2	Electrical measurements	51
3.4.3	Fitting procedure	56
4	The impact of grain size - Activation energy and migration pathways in MAPbBr₃ solar cells	59
4.1	Introduction	60
4.2	Results and discussion	61
4.2.1	Varying the grain size in MAPbBr ₃ solar cell devices	61
4.2.2	Transient ion drift characterisation	64
4.2.3	Activation energy increase, constant mobile ion density and diffusion coefficients	65
4.2.4	Geometrical modelling	68
4.2.5	Trap states	70
4.3	Conclusion	71
4.4	Appendix	72
4.4.1	Device fabrication and characterisation	72
4.4.2	Capacitance measurements	73
4.4.3	Model of ion migration pathways	78
5	2D or not 2D - Reduced ion migration by addition of a 2D layer, comparing PEA, FEA and mixed PEA/FEA	83
5.1	Introduction	84
5.2	Results and discussion	85
5.2.1	2D/3D device fabrication, with FEA, PEA and mixed FEA/PEA as 2D spacer molecules	85
5.2.2	Thermal admittance spectroscopy and transient ion drift characterisation	87
5.2.3	Quantification of the ion migration characteristics	89
5.2.4	Halide migration in the 2D/3D perovskites	91
5.3	Conclusion	94
5.4	Appendix	96
5.4.1	Device fabrication	96
5.4.2	Electrical measurements	96
5.4.3	Fitting procedure	97
	Bibliography	101
	Summary	127

Samenvatting	131
List of publications	135
Acknowledgements	139
About the author	153

1 INTRODUCTION

1.1 THE ROLE OF SOLAR CELLS IN THE ENERGY TRANSITION

Climate emergency is happening before our eyes. The depth and intensity at which the planet Earth will be hit, and the severity of the threat to humanity might to this day be unknown, but the forces behind it are already set in motion. As stated in the latest IPCC report, “Global surface temperature will continue to increase until at least the mid-century under all emissions scenarios considered¹.” In 2015, in an unprecedented international effort to address the climate crisis, the Paris agreements brought together 191 states to agree on maintaining the temperature rise to a maximum of 2 °C.

The IPCC report in 2020 unfortunately casts a shadow to this prospect, as “global warming of 1.5 °C and 2 °C will be exceeded during the 21st century unless deep reductions in carbon dioxide (CO₂) and other greenhouse gas emissions occur in the coming decades¹.” The urgency to reduce greenhouse gas emissions has thus never been so high. To get a grasp of the challenge ahead of us, we can observe the annual global CO₂ emission per year, presented in Figure 1.1. This shows an exponential increase in CO₂ emissions since the mid-19th century, with emission peaks exceeding 40 billion tons per year in 2018 and 2019.

The energy sector represents over 70 % of the global greenhouse gas emissions² (see Figure 1.2). To reduce these greenhouse gases emissions, a global shift in the energy sector is thus needed. This shift is called the green energy transition, and it is defined by the IRENA (International Renewable Energy Agency) as the “pathway toward transformation of the global energy sector from fossil-based to zero-carbon by the second half of this century”³.

An essential lever in that direction is the development and upscaling of the renewable energy sector, to dramatically increase these energies’ share in the energy mix. Renewable energy sources such as solar, wind, geothermal or biomass energy indeed differ from fossil fuels - oil, natural gas and coal - in that they are naturally replenished on a human

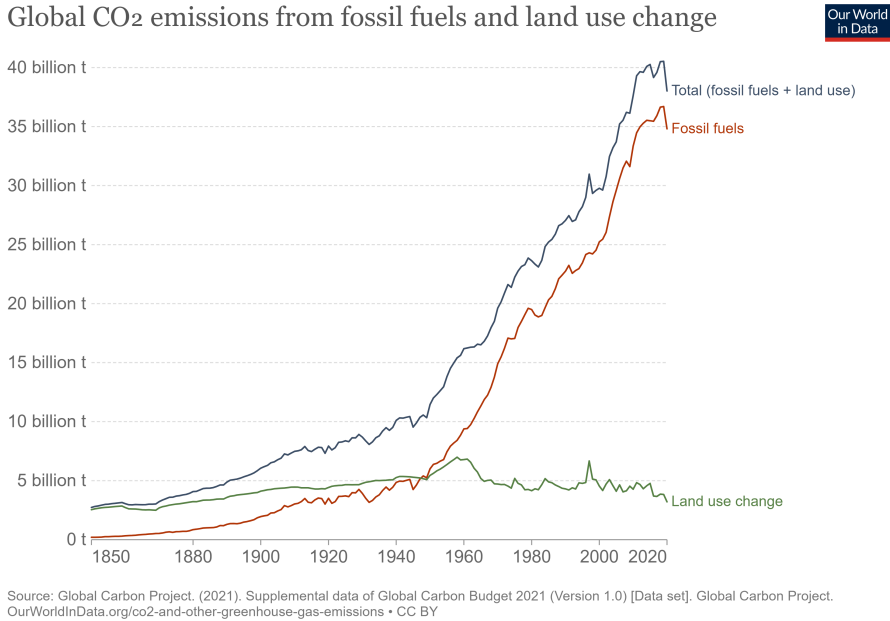


FIGURE 1.1. Annual CO₂ emissions worldwide, from 1850 to 2019. Reproduced from reference 2.

timescale. This allows for regular and prolonged use of energy, without compromising the availability of these energy resources for future generations.

The PhotoVoltaic (PV) sector is specifically promising with its total of 773 GW of installed capacity worldwide, of which 138 GW (18%) were installed in 2020 alone⁴. With solar PV becoming the lowest cost-option for electricity generation in many parts of the world, policy support in the form of public investment is growing, as well as private investments.

At its core, a solar cell is a device which transforms solar energy into electrical energy. To do so, a solar cell consists of a photosensitive “active” layer, necessary to absorb photons from the solar spectrum. In semiconductors, these photons are absorbed and give rise to excitons, which are pairs of electrons and holes. The electrons and holes must then be transported through the active layer to their respective electrodes, where the current can be extracted.

Nowadays, silicon PV represents the highest share within the PV sector. While this technology might be efficient and reliable, the maximum theoretical efficiency limit of this technology has already been reached,

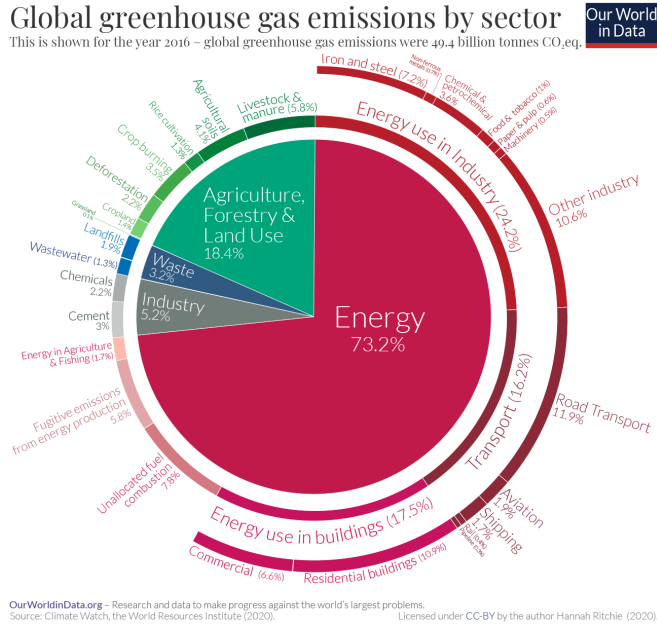


FIGURE 1.2. Global greenhouse gas emissions by sector, showing the energy sector as main contributor - data from 2016. Reproduced from reference 2.

and the silicon solar panels are not very flexible, making them unsuitable for proper integration in a variety of landscapes. The development of new PV materials with higher efficiencies, lower costs and with desirable properties such as material flexibility is a constant drive in research. In recent years, a specific type of material has attracted a lot of attention, namely the perovskite solar cells. With efficiencies rising dramatically in just a decade, these materials hold high promises in the PV sector.

1.2 PEROVSKITE SOLAR CELLS

The term “perovskite” describes a crystallographic structure. It was first used in 1839 by the German scientist Gustav Rose to name the mineral CaTiO_3 ⁵. Gustav Rose discovered this new mineral rock in the Ural mountains in Russia, and the word itself is an homage to the Russian mineralogist Lev von Perovski. In such a crystallographic structure, a monovalent A-cation sits in the centre of corner-sharing octahedra composed of divalent B-cations and monovalent X-anions. With its high bandgap of 3.8 eV ⁶, the original perovskite CaTiO_3 behaves as an insu-

lating material.

The first use of a perovskite structure in a solar cell device was shown by Miyasaka *et al.* in 2009⁷. There, the two studied perovskites were MAPbI₃ and MAPbBr₃, coining the name of “organometal” perovskite, later labelled hybrid perovskites because of the mixed nature between the organic A ion and the inorganic B and X ions. In these structures, the inorganic framework consists of lead (Pb²⁺) as the divalent B-cation, and a halide species (X⁻) as the monovalent X-anion, leading to the general term of lead halide perovskites (see Figure 1.3). The A-cation can either be a methylammonium (MA⁺) molecule or a bulkier formadimium (FA⁺) molecule⁸ in the case of hybrid lead halide perovskites, or a cesium (Cs⁺) cation⁹ in the case of all-inorganic lead halide perovskites. Contrary to the oxide perovskites, the bandgap of these lead halide perovskites falls into the visible range, making them suitable for solar cell and LED applications.

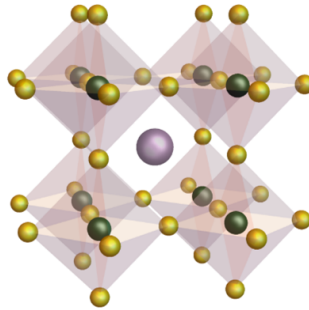


FIGURE 1.3. Perovskite ABX₃ crystallographic structure, with A the monovalent cation shown in purple, B the divalent cation shown in green, and X the monovalent anion in yellow. In lead halide perovskites, the B-cation is Pb²⁺ and the X-anion is a halide, either I⁻, Br⁻ or Cl⁻.

From the initial demonstration in a solar cell device in 2009, lead halide perovskite solar cells have shown an outstanding growth in Power Conversion Efficiencies (PCEs) over the recent decade, a trend which is unprecedented in the PV sector. The National Renewable Energy Laboratory (NREL) chart, which collects the record efficiencies of all PV devices, shows this dramatic increase (see Figure 1.4).

Part of the reason for the great success of lead halide perovskites comes from their bandgap tunability, where a simple modification of the halide species allows for a large variation in the bandgap energy: for example, in the methylammonium-based lead halide perovskites, the

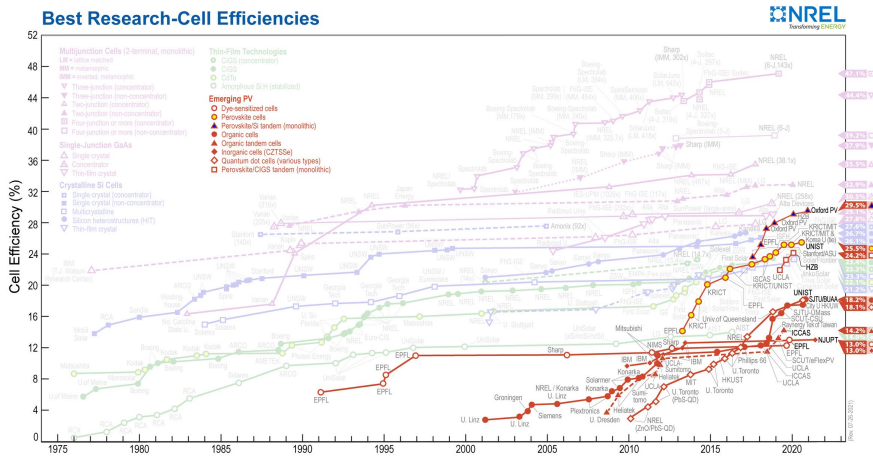


FIGURE 1.4. NREL chart presenting the record efficiencies of each of the PV technologies. The very rapid increase of the emerging PV sector over the last decade is shown in red, where perovskites play a crucial role. Reproduced from reference 10.

bandgap can span all the way from 1.6 eV for $X = \text{I}$ to 2.9 eV for $X = \text{Br}$. An illustration of this bandgap tunability in the field of LED devices is shown in Figure 1.5.

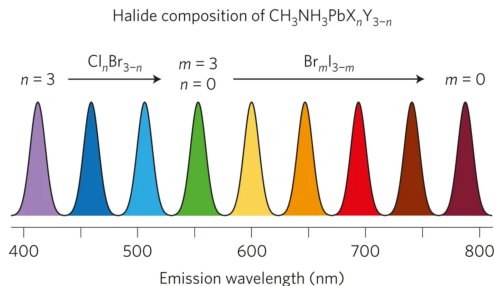


FIGURE 1.5. Bandgap tunability of the MAPbX_3 perovskites series. Reproduced from reference 11.

Lead halide perovskites also present the key benefit of facile preparation, as they can be made with a variety of deposition techniques, ranging from wet chemistry (spin coating, drop casting, inkjet printing etc) to physical deposition by thermal evaporation. Low cost, reproducibility and large-scale homogeneity of the prepared perovskite layers are all key factors to consider for mass scale production of this technology.

Finally, a last key for the success of lead halide perovskites comes from their defect insensitivity. As mentioned above, perovskite layers can easily be prepared by a variety of fabrication methods. The resulting films often present high densities of structural defects, which could potentially reduce the efficiency of the resulting devices. In lead halide perovskites however, these defects have shallow energy levels¹² and thus do not contribute to non-radiative recombination of the electrons and holes. This defect insensitivity is essential to understand both the long carrier diffusion lengths (above 1 μm)¹³ and the high effective carrier mobilities (around 20 $\text{cm}^2 \text{V}^{-1} \text{s}^{-1}$)¹⁴ in these materials. The nature of the defects will be explored further in section 1.3.

Lead halide perovskite devices thus offer key benefits in terms of bandgap tunability, facile preparation methods, and outstanding efficiencies. There is however a major challenge ahead: while silicon PV panels last for more than 25 years, the lead halide perovskite devices are comparatively very unstable. If we want these devices to take their full part within the solar technology portfolio to contribute to the increase of carbon-neutral energy capacities, this instability issue should thus be clearly addressed.

1.3 THE ISSUE OF EXTRINSIC INSTABILITY...

The instability of lead halide perovskites is not surprising, considering the low activation energy required in the reaction process from precursors to perovskite, $\text{CH}_3\text{NH}_3\text{X}(\text{s}) + \text{PbX}_2(\text{s}) \rightarrow \text{CH}_3\text{NH}_3\text{X}_3(\text{s})$. Using solution calorimetry, Ivanov *et al.* found the standard enthalpies of formation to be on the order of 5 kJ/mol, for the whole halide series, $\text{X} = \text{I}, \text{Br}, \text{Cl}$ ¹⁵. Interestingly, the standard Gibbs free energy of $\text{CH}_3\text{NH}_3\text{X}_3$ is negative, which is commonly interpreted as an indication for the stability of the hybrid perovskite compared to its constituent halides. However, the main stabilisation factor is found to be the entropic contribution, which is larger than the small enthalpic contribution^{15,16}. This situation makes the intrinsic stability of the lead halide perovskites less straightforward than the negative Gibbs free energy might initially suggest. Indeed, while in most reactions, the enthalpic contribution is considered the thermodynamically driving factor for the degradation reaction, in some specific cases, such as reactions involving gaseous phases, high temperatures or dissociation processes, and especially when the enthalpic contribution is low, the entropic factor can play a decisive role¹⁶. This is particularly

relevant for lead halide perovskites, which have been observed to degrade into the volatile gaseous phases of CH_3X and NH_3 ¹⁷, and CH_3NH_2 and HX ¹⁸. Thermal stress is thus one of the prominent environmental factors affecting lead halide perovskites stability. Another source of degradation for perovskites is humidity^{19,20}, which can lead both to the formation of hydrated phases of the perovskite crystal, and/or to the desorption of the AX species, further degrading the perovskite layer into separate phases of AX and PbX_2 . Other environmental damaging factors include oxygen exposure^{21,22} and UV radiation^{23,24} (see Figure 1.6).

While all of these environmental factors can lead to perovskite degradation, mitigation strategies have been developed: these include encapsulation strategies²⁵ but also passivation strategies in the bulk of the perovskite, in the grain boundaries or at the interfaces with the transport layers²⁶.

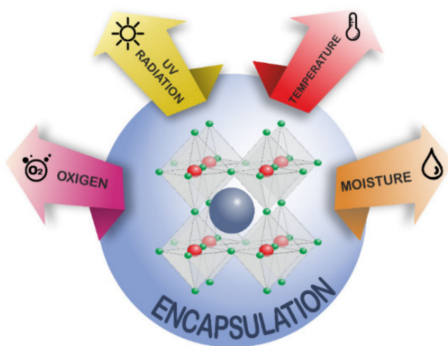


FIGURE 1.6. Schematic representation of different external factors affecting the stability of lead halide perovskites. Reproduced from reference 27.

Contrary to the most commonly-used PV materials, which are based on pure covalent bonding, the bond in lead halide perovskites also exhibits some ionicity¹². Bearing in mind that ionic bonds are weaker in nature than covalent bonds, this helps to rationalize both the soft structure of the lead halide perovskites^{28,29}, and the low formation energies for defects to occur in the lattice^{12,30,31}. Some of the most common defects include Schottky defects, which are point defects formed when oppositely charged ions leave their lattice sites. Schottky defects occur in stoichiometric units so as to keep the charge balance in the perovskite lattice. In lead halide perovskites, these defects are associated with the formation of methylammonium vacancies, lead vacancies and halide vacancies³². The high concentration of these defect vacancies within the

perovskite lattice is an important contributing factor to ion migration within the perovskite devices. On top of the extrinsic instability issues mentioned above, ion migration thus poses a fundamental intrinsic instability challenge for perovskite solar cells.

1.4 ... AND INTRINSIC STABILITY, A CLOSER LOOK AT ION MIGRATION

Ion migration is the process whereby an ion moves from its original position in the perovskite lattice to a new position within the perovskite lattice. This process happens through a hopping mechanism and can either be vacancy-mediated or interstitial-mediated. DFT calculations³³ show that the vacancy-mediated process has a lower activation energy, making it the most probable process within the lead halide perovskites. Schematic examples of vacancy-mediated ion migration of the halide ion, lead ion and methylammonium ion are shown in Figure 1.7 and 1.8. When calculating the respective migration energies of each of the individual ions MA^+ , Pb^{2+} and I^- in the case of MAPbI_3 , Eames *et al.* find values of 0.84 eV, 2.31 eV and 0.58 eV, respectively³³. Based on these calculations, the most mobile species should therefore be the halide species, while the lead ion is assumed to be the least mobile of the ionic species within the perovskite lattice.

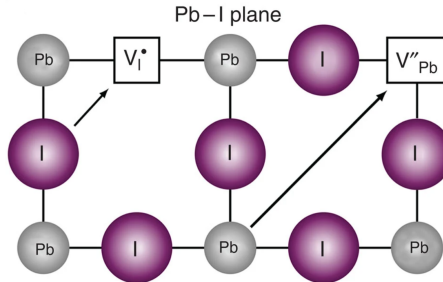


FIGURE 1.7. Schematic representation of ion migration of the iodide and lead ionic species towards their respective vacancies in the perovskite crystal lattice. Reproduced from reference 33.

Azpiroz *et al.* also use DFT simulations to calculate the migration activation energies in MAPbI_3 and MAPbBr_3 . In line with the results from Eames *et al.*, they also find $E_a(\text{X}^-) < E_a(\text{MA}^+) < E_a(\text{Pb}^{2+})$ as the general trend, but the values are comparatively lower, with E_a

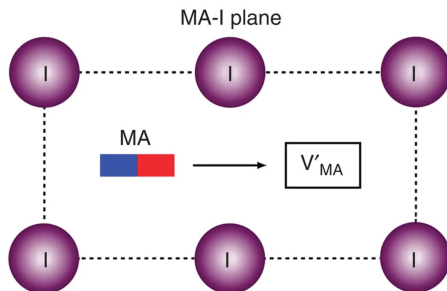


FIGURE 1.8. Schematic representation of ion migration of the methylammonium ionic species towards the methylammonium vacancy site in the perovskite crystal lattice. Reproduced from reference 33.

$(X^-) < 0.1\text{ eV}$ for both the iodide and bromide ions³⁴. Quantitatively, the results from DFT calculations thus differ and depend on specifics of the calculation model and computation arithmetic³⁵, but qualitatively they still provide very insightful trends, useful for comparison between specific conditions. For example, Meggiolaro *et al.* find a lower formation energy for the formation of ion vacancies at the surface rather than in bulk³⁶, while Haruyama *et al.* find that the substitution of MA^+ by the bulkier FA^+ cation increases the migration energies for both the halide ion and the A-cation³⁷. DFT simulations screen systems on the order of 100 atoms, for timescales in the range of picoseconds³⁸. To model larger systems and/or longer timescales, Molecular Dynamics (MD) simulations are more commonly adopted. Using classical MD, Balestra *et al.* study ion diffusion from the halide species in the all-inorganic CsPbX_3 perovskites, and are able to distinguish the influence of the vacancy concentration from the influence of the migration activation energies³⁹. In the methylammonium-based mixed-halide perovskites, Ruth *et al.* use Monte Carlo simulations to show that halide migration is a vacancy-mediated process in these systems⁴⁰. Modelling of ion migration in lead halide perovskites thus offers a wealth of information in terms of defect formation energies and ion migration energies, which together can help rationalise some of the experimental findings.

Experimentally, there are two main avenues for the observation of ion migration in lead halide perovskites. The first avenue consists of the imaging and elemental characterisation techniques, which help visualise and characterise the ion migration processes^{35,41}, for instance in terms of the nature of the migrating ions and their localisation within the perovskite layers. One of the clearest visualisation of the ion mi-

gration process was achieved by Luo *et al.*, who used a combination of nano X-Ray Fluorescence (XRF) and spatially resolved PL and were able to directly observe the migration of the bromide ion in a MAPbBr_3 single crystal⁴² (see Figure 1.9). Regarding the localisation of the mobile ions within the perovskites layer, Huang *et al.* used a combination of Kelvin Probe Force Microscopy (KPFM) and conductive atomic microscopy, and suggested that the mobile ions could aggregate near the device interfaces⁴³. Yun *et al.* further used KPFM to show the enhancement of ion migration in the grain boundaries versus the bulk of the grains, in both formadium and methylammonium lead halide perovskites⁴⁴. Using time-of-flight secondary-ion mass spectrometry, Zhang *et al.* could also study the degradation of MAPbI_3 and FAPbI_3 and profile the spatial distributions of the elements throughout full device stacks. They found that the iodide ion could transfer into the Hole Transport Material (HTM) and even through it to the silver electrode, and that degradation occurred faster in MAPbI_3 compared to FAPbI_3 ⁴⁵.

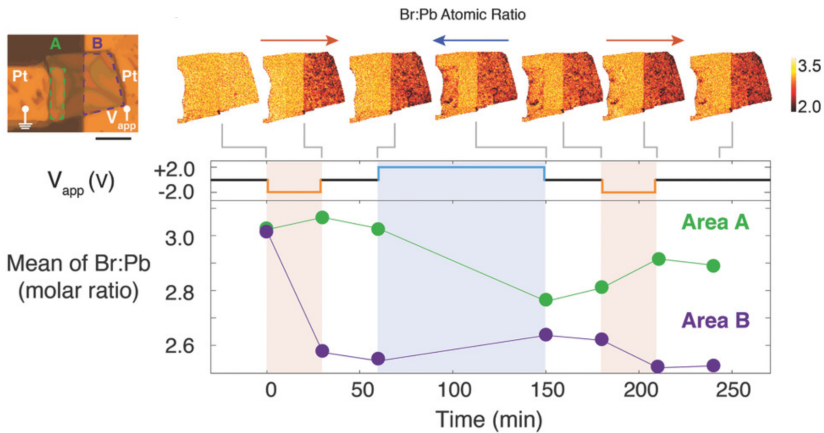


FIGURE 1.9. Nano-XRF measurement of the changes in elemental distribution in a $\text{CH}_3\text{NH}_3\text{PbBr}_3$ single crystal under bias. Reproduced from reference 42.

Imaging and elemental techniques are thus critical to visualise the ion migration process, in order to probe which ions are moving within the devices and where they travel to. This set of techniques can also be used to study specific parameters of interest (such as film preparation conditions^{46,47}, grain passivation effects⁴⁸, etc.) and probe local variations within the perovskite layers, for instance bulk migration versus grain boundary migration. They do, however, lack to a large extent the quantification of the ion migration processes at hand, and are better at

characterising the migration processes from the heavy halide or cesium ions compared to the lighter organic cations such as MA^+ and FA^+ .

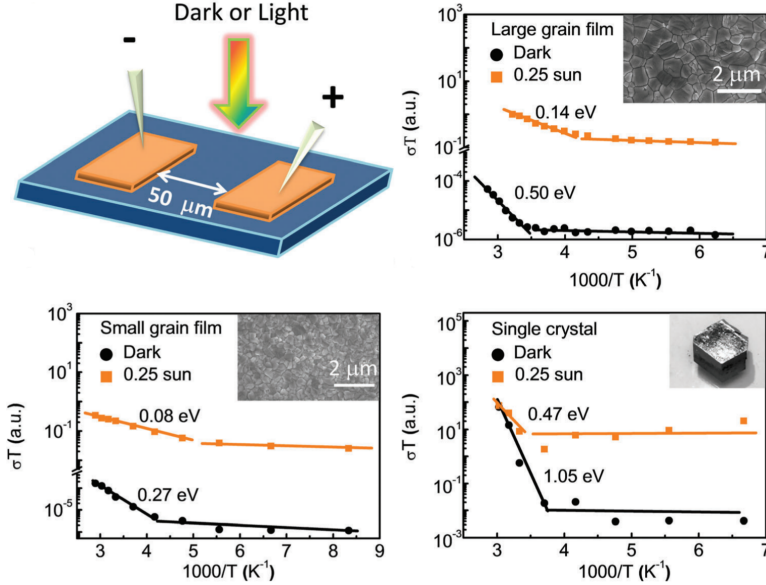


FIGURE 1.10. Quantification of the ion migration activation energy in MAPbI_3 solar cells of various grain sizes, using temperature-dependent conductivity measurements. Reproduced from reference 49.

The second avenue of experimental techniques are temperature dependent transients measurements, such as conductivity and impedance measurements^{35,41}. In these techniques, a physical property related to ion migration is measured at various temperatures. The characteristic timescales of the migration process are then recovered for each of these temperature transients, and finally, the activation energy for ion migration can be calculated by using the Arrhenius equation. Using impedance measurements, Bag *et al.* could compare the ion migration activation energy in pure MAPbI_3 with that of the mixed cation system $\text{MA}_x\text{FA}_{1-x}\text{PbI}_3$, finding $E_a(\text{MAPbI}_3) < E_a(\text{MA}_x\text{FA}_{1-x}\text{PbI}_3)$ ⁵⁰, while Xing *et al.* used temperature-dependent conductivity measurements to compare the migration activation energy in single crystals with those found for polycrystalline perovskite films of various grain sizes. There, they find an activation energy E_a for ion migration under dark conditions of 1.05 eV in the single crystal, of 0.50 eV in the films with large grains, and of 0.27 eV in the films with small grains (see Figure 1.10), i.e. a de-

crease in activation energy for the films with smaller grains⁴⁹. This set of temperature-dependent transient techniques thus offers a key quantification benefit as they can be used to determine the migration activation energy. They do, however, lack the possibility of distinguishing which ionic species is migrating and thus often consider the range of possible ionic migration processes as a single averaged process. Besides this key issue of ion species discrimination, parameters other than the migration energy alone might be key to describe and understand the ion migration processes at play, such as the density of mobile ions or their diffusion coefficient. To fill in these gaps, we find Transient Ion Drift (TID) to be a suitable measurement technique to study the ion migration processes in lead halide perovskites.

1.5 THE TRANSIENT ION DRIFT TECHNIQUE

In this thesis, we make use of the TID technique to measure, quantify and analyse the ion migration processes taking place in lead halide perovskite solar cell devices.

TID relies on the application of a voltage bias to collapse the depletion layer within the perovskite semiconductor. The ions then diffuse through the device until they are homogeneously distributed. When releasing the voltage pulse, the ions will drift towards the electrode following the built-in electric field across the perovskite layer, changing the depletion width⁵¹. Considering the perovskite cell as a parallel-plate capacitor, this ion drift therefore leads to a change in the thickness of the dielectric layer (the depleted part of the perovskite layer). The evolution of capacitance over time thus results in a measurement of the ion dynamics. A more detailed description is provided below.

In Figure 1.11, we see a simplified scheme of the different steps taking place in the perovskite device during the TID measurement. In the first step, shown in Figure 1.11a, the device is in steady-state conditions and the ions are close to the electrodes of reverse polarity, where they accumulate. We then apply a voltage pulse V_0 to the device, which redistributes the electrostatic field across the perovskite layer, changing the bands, as illustrated in Figure 1.11b. In TID measurements, V_0 is chosen close to the built-in voltage V_{BI} of the device, such that the perovskite layer is fully depleted after application of this bias. The ions then start diffusing within the layer (Figure 1.11c-d) until they are fully homogenised, and flat band conditions are reached (Figure 1.11e). At

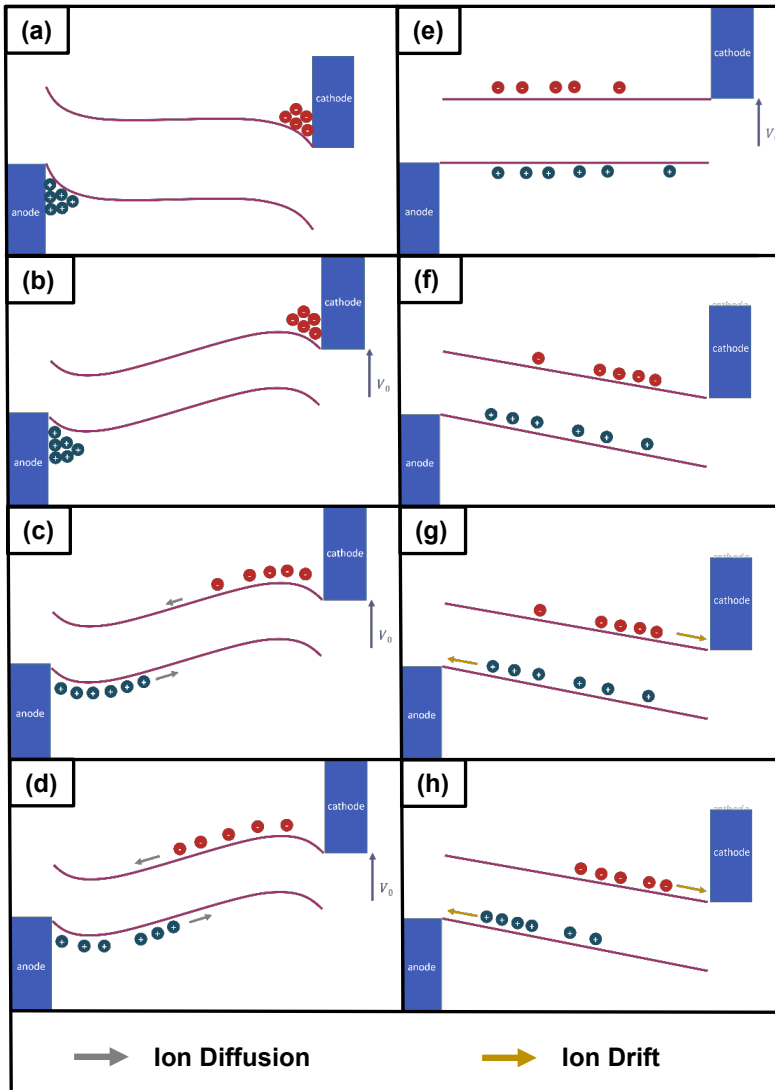


FIGURE 1.11. Schematic illustration of the different steps taking place in the perovskite layer of the solar cell device, after application of a voltage bias V_0 , and successive release of this bias. After application of the voltage pulse, the depletion layer in the device is fully collapsed and the mobile ions diffuse within the perovskite layer, until they reach steady-state conditions. Then, the pulse is released, and the ions drift back to their original position – this is the time during which we record the ion drift dynamics with TID. Design inspired by M. Futscher⁵¹.

that point, we can say that the device has reached its new steady-state conditions. We then release the voltage pulse V_0 , which results in the bands shifting by discharging of the capacitor (Figure 1.11f), and the ions starting to drift (Figure 1.11g-h) until they reach their initial position, accumulating at the electrodes (Figure 1.11a).

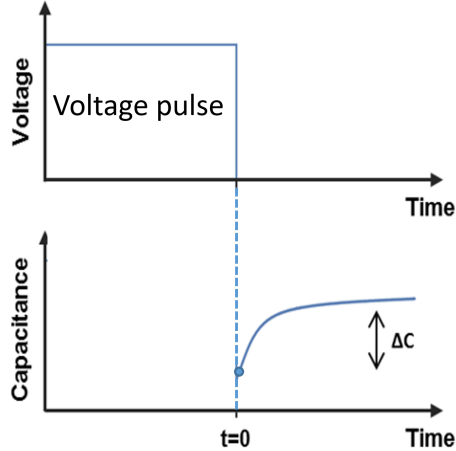


FIGURE 1.12. Measurement sequence of the TID technique. Design inspired by M. Futscher.

The measurement sequence is shown in Figure 1.12: a voltage pulse is first applied to the device, after which the capacitance of the sample is recorded as a function of time. Capacitance is thus recorded from the release of the voltage pulse, which we label $t = 0$ (shown in Figure 1.11f), to the moment when the device reaches its steady-state conditions (shown in Figure 1.11a.). Capacitance is measured by applying a small perturbation voltage $V_{AC} \sim 20$ mV to the perovskite device and measuring its impedance. The impedance signal is then converted to capacitance assuming a simple circuit model⁵².

TID allows for the discrimination of ion migration from a cation or an anion species. This can be determined by the sign of the capacitance transients. Specifically, in the case of a p-type semiconductor, a decay in capacitance transients signals anion migration and a rise in capacitance transients signals cation migration - and vice-versa in the case of an n-type semiconductor⁵³. We recently found that this determination hinges on the assumptions made in the analysis (perovskite doping, only one depletion layer, ion drift dominant over diffusion), which might not be fulfilled in some devices. Three key parameters can be quantified with

TID: the activation energy for ions to migrate, E_a , the ion diffusion coefficient prefactor, D_0 , and the mobile ion concentration, N_{ion} . These can be extracted using the following fitting procedure.

We first fit the capacitance transients to Equation 1.1, where $C(t, T)$ is the capacitance at time t and temperature T , $C_\infty(T)$ is the steady-state capacitance at temperature T , $\Delta C_n(T)$ is the amplitude of the process n in the transient at temperature T and τ_n is the lifetime of process n .

$$C(t, T) = C_\infty(T) + \sum_n \Delta C_n(T) \exp\left(\frac{-t}{\tau_n}\right) \quad (1.1)$$

Specifically, $C_\infty(T)$ is extracted from the measurements directly from the steady-state capacitance, before the algorithm is allowed to find the best values for $\Delta C_n(T)$ and τ_n . As Equation 1.1 shows, the fit function can be adapted to contain any number of exponential terms needed to resolve the full dataset of capacitance transients, where each of these exponential terms represents one specific ion migration process n , with its own mobile ion concentration $N_{ion(n)}$, diffusion coefficient $D_{0(n)}$ and migration activation energy $E_{a(n)}$.

Once we have extracted τ_n , it can be rewritten as a function of the activation energy $E_{a(n)}$ and of the ion diffusion coefficient prefactor $D_{0(n)}$, following Equation 1.2:

$$\tau_n = \frac{k_B T \epsilon \epsilon_0}{q^2 N_D D_{0(n)}} \exp\left(\frac{-E_{a(n)}}{k_B T}\right) \quad (1.2)$$

where k_B is the Boltzmann constant, ϵ is the perovskite permittivity, ϵ_0 is the vacuum permittivity, q is the elementary charge and N_D is the doping density. Using Equation 1.2, we thus retrieve both $D_{0(n)}$ and $E_{a(n)}$ for each of the n processes.

Finally, the fitted $\Delta C_n(T)$ parameters are used to determine the ion concentration $N_{ion(n)}(T)$ using Equation 1.3:

$$N_{ion(n)}(T) = 2 N_D \frac{\Delta C_n(T)}{C_\infty(T)} \quad (1.3)$$

This fitting procedure thus allows for quantification of $N_{ion(n)}$, $D_{0(n)}$ and $E_{a(n)}$, key parameters characterising the ion migration processes taking place in the lead halide perovskite solar cells studied within this thesis.

The following chapters illustrate the evolution of the fitting procedure to the TID datasets obtained, from single temperature transient fitting

(Chapter 2), to global transient fitting - i.e. fitting all temperature transients from a specific TID dataset in a “single” global step - (Chapters 3 and 4), and global transient fitting in combination with a genetic algorithm approach (Chapter 5). These different methods all rely on the same set of equations, themselves based on the same assumptions, which are detailed below.

To write the previous set of equations, several assumptions are necessary. We first assume that the electric field is mostly determined by the doping density, and that the ions only pose a small perturbation, i.e. that the depletion width is mostly governed by the electronic charge carriers, and only slightly affected by the migration of ions. We also assume that the electric field after application of the voltage pulse varies linearly within the perovskite bulk^{54,55}, that the total ion density is conserved, and that the diffusion is negligible against drift.

With this powerful technique, both able to distinguish anion migration from cation migration and capable of quantifying the relative contributions to ion migration - in terms of activation energy, diffusion coefficient and mobile ion density - we can explore a wide range of perovskite materials and shed light on the underlying ion migration processes.

1.6 OUTLINE OF THIS THESIS

The research question driving this thesis is the following: "How can we reduce ion migration in lead halide perovskite solar cells?". We aim to answer this question by studying a range of different factors which might affect ion migration in these solar cells.

We first look at the effect of the perovskite composition, with two study cases: first, comparing the ion migration processes in the pure-halide systems of MAPbBr₃ and MAPbI₃ (Chapter 2); second, looking at the effect of the halide ratio in the mixed-halide MAPb(Br_xI_{1-x})₃ perovskites (Chapter 3). We then explore the effect of crystallinity, by studying the impact of the grain size on ion migration in MAPbBr₃ solar cells (Chapter 4). Finally, we also explore the effect of the dimensionality of the perovskite, by adding a thin 2D perovskite layer on top of a 3D perovskite and studying how this affects ion migration in these 2D/3D heterostructures (Chapter 5).

2 THE CASE OF MAPbBr₃ VERSUS MAPbI₃

SUPPRESSION OF METHYLAMMONIUM MIGRATION AND REDUCTION OF HALIDE MIGRATION

Solar cells based on metal halide perovskites often show excellent efficiency but poor stability. This degradation of perovskite devices has been associated with the migration of mobile ions. MAPbBr₃ perovskite materials are significantly more stable under ambient conditions than MAPbI₃ perovskite materials. In this chapter, we use transient ion drift to quantify the key characteristics of ion migration in MAPbBr₃ perovskite solar cells. We then proceed to compare them with those of MAPbI₃ perovskite solar cells. We find that in MAPbBr₃, bromide migration is the main process at play and that contrary to the case of MAPbI₃, there is no evidence for methylammonium migration. Quantitatively, we find a reduced activation energy, a reduced diffusion coefficient, and a reduced concentration for halide ions in MAPbBr₃ compared to MAPbI₃. Understanding this difference in mobile ion migration is a crucial step in understanding the enhanced stability of MAPbBr₃ versus MAPbI₃.

This chapter is based on the following publication⁵⁶:
Lucie McGovern, Moritz H. Futscher, Loreta A. Muscarella and Bruno Ehrler, "Understanding the Stability of MAPbBr₃ versus MAPbI₃: Suppression of Methylammonium Migration and Reduction of Halide Migration", *Journal of Physical Chemistry Letters*, vol. 11, no. 17, pp. 7127–7132, 2020.

2.1 INTRODUCTION

Perovskite solar cells, with solution-based, cheap synthesis methods and a rapid increase in power conversion efficiency, are a promising candidate for future solar cells. Record efficiencies of 25.2% and 29.2% for single-junction and perovskite/silicon tandem configurations¹⁰ are already competitive with those of existing technologies. However, a major hurdle for commercialization remains, the degradation of high-efficiency perovskite materials under a range of environmental factors. Humidity^{57–59}, illumination^{60–63}, and thermal stress^{63,64} have all been shown to degrade the power conversion efficiency of the devices over time. Ion migration has been identified as one of the main drivers for degradation⁶⁵.

The stability of metal halide perovskites is composition-dependent. For example, MAPbI₃ is more sensitive to all of the environmental factors mentioned above than MAPbBr₃⁶⁶. Some mechanisms have been proposed to explain this stability enhancement. In terms of material degradation, decomposition studies link the enhanced stability of MAPbBr₃ to a predominance of the reversible decomposition reaction $\text{CH}_3\text{NH}_3\text{PbX}_3(\text{s}) \rightleftharpoons \text{CH}_3\text{NH}_2(\text{g}) + \text{HX}(\text{g}) + \text{PbX}_2(\text{s})$, compared to the irreversible decomposition pathway $\text{CH}_3\text{NH}_3\text{PbX}_3(\text{s}) \rightleftharpoons \text{NH}_3(\text{g}) + \text{CH}_3\text{X}(\text{g}) + \text{PbX}_2(\text{s})$, in contrast to MAPbI₃ that exhibits both types of decomposition⁶⁷. More recently, the decomposition reaction $4\text{CH}_3\text{NH}_3\text{PbX}_3 + \text{O}_2 \rightleftharpoons 4\text{PbX}_2 + 2\text{X}_2 + 2\text{H}_2\text{O} + 4\text{CH}_3\text{NH}_2$ has been shown to slow upon substitution of iodide with bromide⁶⁸.

In terms of ion migration, theoretical predictions for MAPbBr₃ suggest that the stronger Pb–Br bond^{69–72} could increase the halide ion defect formation energy⁷³ and thereby suppress the degradation caused by ion migration. Migration of the bulky MA⁺ ion might also be inhibited by steric hindrance, because the lattice constant of MAPbBr₃ is smaller^{74,75}, and/or by stronger hydrogen bonding to the surrounding Pb–Br₆ octahedra. However, though ion migration is one of the causes of degradation of perovskite devices⁶⁵, many of its aspects remain poorly understood. It is in fact unclear if the ion migration is reduced in MAPbBr₃ compared to MAPbI₃, and which aspect of the mobile ions is affected.

Here we use transient ion drift (TID) to quantify the characteristics of mobile ions in MAPbBr₃. We identify the nature of mobile ions and their

activation energy, concentration, and diffusion coefficients and compare them to the characteristics of mobile ions in MAPbI₃⁷⁶. We find that the concentration of mobile bromide ions is on average 8 times lower than in their iodide counterpart in MAPbI₃, and that the bromide ions diffuse ~ 3 times slower, with an activation energy that is slightly lower than that of the migration of iodide. Halide migration is therefore greatly affected when tuning the halide composition. However, the halide composition does not affect solely the halide migration, as one might expect. A striking difference between the iodide and bromide perovskites lies in the methylammonium (MA⁺) migration. We measure a high density of migrating MA⁺ ions in the iodide perovskite. In stark contrast, MA⁺ migration is inhibited in the bromide perovskite. This difference might be one of the keys to their higher structural stability, because the A-site cations have been shown to be critical for the structural properties of perovskites^{77,78}. We hence assign the higher stability of the MAPbBr₃ perovskite in part to slower and fewer mobile halide ions, and in part to the suppression of MA⁺ cation migration.

We use TID, a capacitance-based technique, to measure the mobile ions in the perovskite diodes. While there are several techniques for measuring ion migration, TID allows for discrimination between anion and cation migration and independently measures the number density (N_{ion}) and diffusion coefficient (D) of mobile ions. With temperature-dependent measurements of the capacitance transients, TID further quantifies the activation energy (E_a) for ions that migrate. A more detailed discussion of the technique can be found in reference [51].

2.2 RESULTS AND DISCUSSION

2.2.1 MAPbBr₃ SOLAR CELL DEVICE CONFIGURATION

We fabricate a full solar cell as the diode for capacitance measurements and choose suitable contact layers such that the main contribution to the ion drift comes from the perovskite layer. The architecture of the solar cell is a planar p-i-n junction as shown in Figure 2.1a. For a direct comparison with our reported results on MAPbI₃⁷⁶, we use the same transport layers: NiO_x as the hole transport layer and C₆₀ and BCP as electron transport layers. We also prepare the MAPbBr₃ perovskite using a similar antisolvent technique, modified slightly to yield films of similar thickness and grain size. Figure 2.1b shows a top view scanning electron microscopy (SEM) image of such a MAPbBr₃ perovskite film formed on

top of NiO_x. The film features a good surface coverage and an apparent grain size (as estimated by SEM morphology) between 200 and 500 nm, comparable to the average 300 nm size of MAPbI₃ perovskite grains from our previous report. Cross-sectional SEM shows layers of (180 ± 20) nm as shown in Figure 2.1c, also comparable to our MAPbI₃ solar cells. With MAPbBr₃, the device shows a power conversion efficiency of 2.7% (Figure 2.1d), a value close to that of previous work with this simple architecture⁷⁹ (see Section 2.4.1). There is little hysteresis between the forward and reverse scans.

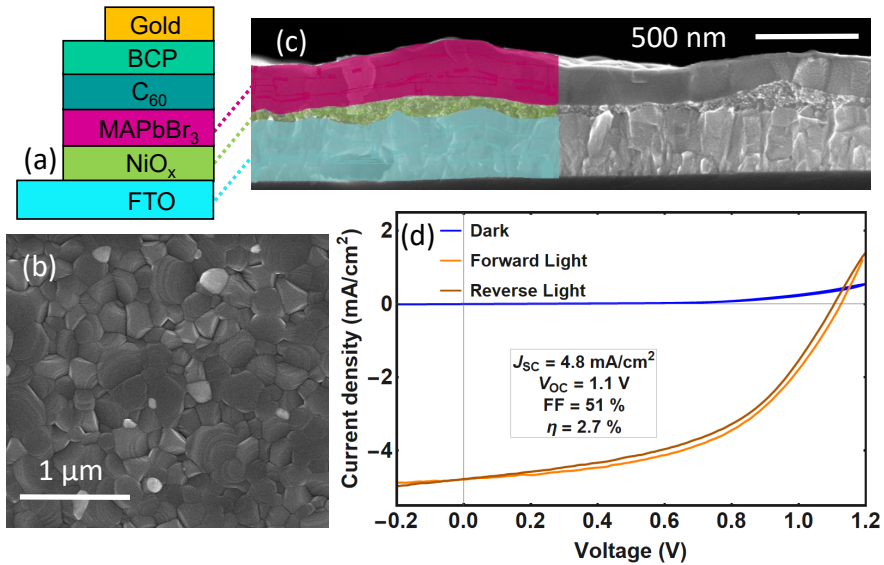


FIGURE 2.1. Inverted MAPbBr₃ device characteristics. (a) Solar cell architecture of the full device, with the MAPbBr₃ film sandwiched between a hole transport layer of NiO_x and an electron transport layer of C₆₀ and BCP. A fluoride tin oxide (FTO) bottom electrode and a gold top electrode complete the device, allowing for the extraction of the holes and electrons. (b) Top view SEM image of the MAPbBr₃ perovskite layer showing grains of 200 to 500 nm. (c) SEM cross-sectional image of the MAPbBr₃ perovskite layer on top of FTO and NiO_x. (d) Current–voltage characteristics measured in the dark and light, with a scan speed of 10 mV s⁻¹.

2.2.2 TID MEASUREMENT SHOWS BROMIDE MIGRATION IN MAPbBr₃

To measure the capacitance transients of the MAPbBr₃ solar cell device, we apply a voltage bias close to the built-in bias of the device (1.1 V) for 1 s to redistribute the ions. After the bias is released, the ions move back to the contacts and we record the resulting capacitance transients (Figure 2.2a; see Section S2.4.2 for experimental details). The relative capacitance change is presented in Figure 2.2b, with one transient every 10 K. We also repeat the whole measurement for a different filling voltage (1.4 V), as is presented in Figure 2.5.

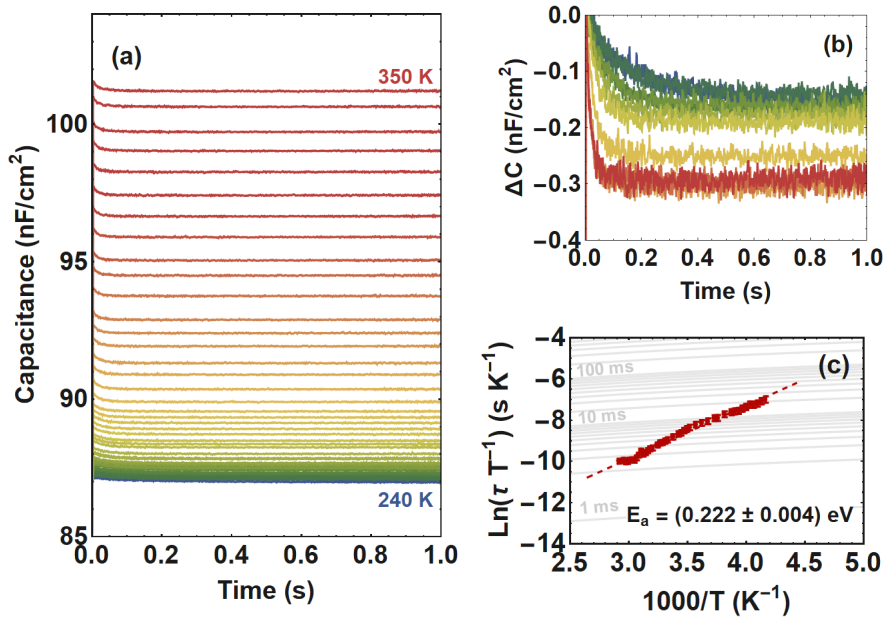


FIGURE 2.2. (a) Capacitance transient measurements of a MAPbBr₃ solar cell measured in the dark, with a DC voltage of 0 V and an AC voltage of 10 mV at 10^4 Hz, after applying a pulse of 1.1 V for 1 s. (b) Relative difference in capacitance $\Delta C = C(t) - C_{2.5 \text{ ms}}$ for the capacitance transients between 240 K and 340 K, in steps of 10 K. (c) Arrhenius plot showing the activation energy derived from this measurement.

The transients in panels a and b of Figure 2.2 show a small and rapid exponential decrease on the order of 10 ms, followed by a flat baseline when the system has reached its steady state. In TID of p-type semiconductors, we assign positive trends to the migration of cations and nega-

tive trends to the migration of anions. Hall measurements⁸⁰ suggest the p-type nature of MAPbBr₃. Additionally, both time-of-flight secondary ion mass spectroscopy (ToF-SIMS)⁸¹ and nanoprobe X-ray fluorescence (Nano-XRF)⁴² measure a time evolution of the spatial bromide concentration in MAPbBr₃ single crystals. We thus assign the negative feature present in the whole temperature range to bromide migration. As there is no apparent positive feature in the capacitance transients, we conclude that there is no or very little cation migration. If present at all, the mobile cation concentration must be below $1.5 \times 10^{13} \text{ cm}^{-3}$, the sensitivity threshold for this measurement (see Section 2.4.2). This is in contrast with our previous results for MAPbI₃, for which we found a combination of migration from the iodide (I⁻) anion and the MA⁺ cation⁷⁶, both with significant concentrations of mobile ions, $1 \times 10^{15} \text{ cm}^{-3}$ for I⁻ and $1 \times 10^{16} \text{ cm}^{-3}$ for MA⁺.

Substituting bromide for iodide in the MAPbX₃ (X = I or Br) framework thus leads to a significant suppression of MA⁺ migration. This effect was already hypothesized as a consequence of the structural contraction of the MAPbBr₃ framework⁶⁸ and/or the stronger hydrogen bonding between the lead halide octahedra and the MA⁺ cation^{68,82}. With regard to this second hypothesis, we note that although it has been evoked multiple times in the literature, the experimental data do not match but instead show an equal strength of hydrogen bonds whether using X = I, Br, or Cl in MAPbX₃⁸³⁻⁸⁵. We therefore infer that the lattice contraction is the origin of the suppression of MA⁺ migration, an assessment that matches the trend found in density functional theory (DFT) modeling³⁴. This means that the lattice unit cell size makes a major contribution to the enhanced stability of these systems. This finding sheds light on the possible origin of the increased stability of complex mixed-cation/mixed-halide perovskites compared to pure-halide materials, as well as the origin of the higher stability of compressed perovskites. In the future, a systematic study of ion migration versus pressure could determine the specific compression factor, i.e., the specific unit cell size, necessary to suppress cation migration.

2.2.3 QUANTIFICATION OF BROMIDE MIGRATION CHARACTERISTICS

To quantify bromide migration, we fit each capacitance transient to extract τ , the lifetime of the process (see Section 2.4.2). Determined over many temperatures, the extracted lifetimes are used in an Arrhenius plot

Activation energy (eV)	Diffusion coefficient at 300 K (cm ² s ⁻¹)	Concentration of mobile ions (cm ⁻³)
(0.25 ± 0.05)	(8.4 ± 3.9) × 10 ⁻¹⁰	(1.3 ± 0.7) × 10 ¹⁴

TABLE I. Characteristics of mobile ions in MAPbBr₃ averaged from four individual measurements.

to obtain E_a and D , as shown in Figure 2.2c and Figure 2.5c. Using the Equation for mobile ion density (see Equation 2.5 in Section 2.4.2), N_{ion} is also measured. The results are listed in Table I, averaging over two different filling voltages each for two solar cells.

2.2.4 COMPARING ION MIGRATION PATTERNS IN MAPbBr₃ AND MAPbI₃

To understand the increased stability of MAPbBr₃ compared to that of MAPbI₃, we compare changes in ion migration (Figure 2.3). We have already presented the data for iodide migration in MAPbI₃ in previous work,(21) and it is reproduced here for comparison.

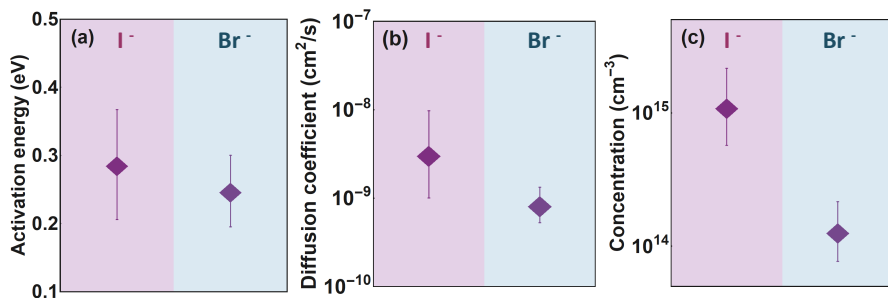


FIGURE 2.3. Comparison of mobile ions in MAPbBr₃ and MAPbI₃ showing (a) a reduced activation energy for bromide migration, (b) a reduced diffusion coefficient for bromide migration (at 300 K), and (c) a reduced density of bromide mobile ions. Error bars are the standard deviations of the weighted means.

Our initial hypothesis was an increase in the activation energy for bromide migration in MAPbBr₃, due to lead forming a stronger bond with bromide than iodide^{69–72}. Our results indicate the reverse trend, with an activation energy slightly decreasing from 0.29 eV for iodide migration to 0.25 eV for bromide migration. These values are close to experimental activation energies found by temperature-dependent hysteresis

measurements⁸⁶. We note that they differ, however, from DFT calculations by Lin *et al.*⁷³, a difference that may arise from the approximation their work uses, of a low-temperature phase with orthorhombic structure. The decrease in activation energy can potentially be rationalized by the smaller size of the bromide ion, possibly reducing the steric hindrance during the transition state of migration for bromide. Meggiolaro *et al.*³⁶ decompose the activation energy into the migration energy barrier $\Delta^\ddagger H^\circ$ and a DFE (defect formation energy) term, the latter accounting for the energy required to form the defect undergoing the jump. Using their finding that the lower limit for the DFE term to vanish is reached for ~ 250 nm grains, we can neglect DFE in our study. What these results serve to show is that the activation energy for ions to migrate is the result of an interplay of competing effects, in this case the steric hindrance versus the bond strength. These numbers can further help us to understand the halide migration mechanism. In fact, molecular dynamics (MD) modeling shows that in both MAPbI₃ and MAPbBr₃, the lowest activation energy for halide migration is through a vacancy-mediated hopping mechanism⁸⁶. The activation energies we measure are similar to the MD-simulated values, which helps us in elucidating the mechanism for halide migration in MAPbBr₃. A vacancy-mediated hopping pathway is likely dominating, as is the case in MAPbI₃^{33,37}.

We turn now to the comparison of the diffusion coefficients, which can be expressed through the following Equation⁵¹:

$$D = D_0 \exp\left(\frac{-\Delta^\ddagger G^\circ}{k_B T}\right) = \frac{v_0 d^2}{6} \exp\left(\frac{\Delta^\ddagger S^\circ}{k_B}\right) \exp\left(\frac{-\Delta^\ddagger H^\circ}{k_B T}\right) \quad (2.1)$$

where $\Delta^\ddagger G^\circ$, $\Delta^\ddagger H^\circ$, and $\Delta^\ddagger S^\circ$ are the changes in Gibbs free energy, enthalpy, and entropy of activation, respectively, for a single ion migration step, k_B is the Boltzmann constant, v_0 is the attempt-to-escape frequency, and d is the jump distance. We choose to follow the usual formalism that refers to the change in Gibbs free enthalpy as activation energy E_a . We measure a bromide diffusion coefficient at 300 K of $\sim 1 \times 10^{-9} \text{ cm}^2 \text{ s}^{-1}$, 3 times less than that of iodide, at $3 \times 10^{-9} \text{ cm}^2 \text{ s}^{-1}$. Following Equation 2.1, if we combine a reduction in both the bromide diffusion coefficient $D(\text{Br})$ and the bromide activation energy $E_a(\text{Br})$, we find that either the attempt-to-escape frequency, $v_0(\text{Br})$, the jump distance, $d(\text{Br})$, or the entropy term, $\Delta S(\text{Br})$, must decrease compared to their iodide counterparts ($v_0(\text{I})$, $d(\text{I})$, and $\Delta S(\text{I})$). The jump distance $d(\text{Br})$ is probably shorter than $d(\text{I})$ due to the smaller lattice constant in

the bromide perovskite, with $[1.2 d(\text{Br})]^2 \simeq d(\text{I})^2$. However, this change is counterbalanced by the increase in the attempt-to-escape frequency $v_0(\text{Br})$, with $v_0(\text{Br}) \simeq 1.5 v_0(\text{I})$, a value that we derive from the Raman and FTIR blue-shifts when moving from iodide to bromide^{83,84,87}. This suggests that the entropy term decreases for bromide compared to iodide, i.e., that $\Delta S^\circ(\text{Br}) < \Delta S^\circ(\text{I})$. Solution calorimetry measurements^{15,16} for the perovskite formation reaction show that the enthalpic and entropic contributions are indeed of opposite directions for both MAPbI₃ and MAPbBr₃. Though of a different nature - the changes considered in references [15] and [16] are about the entropy and enthalpy of reaction and not the entropy and enthalpy of activation - these results underline the importance of considering not only the enthalpic contribution but also the entropic contribution in determining the ion migration diffusion coefficient. Taken together, this means that even if the activation energy to migrate is lower for a bromide ion than for an iodide ion, the reduced diffusion coefficient suggests a smaller entropic gain for bromide migration, explaining the overall trend.

The third element that TID allows us to quantify is the concentration of mobile bromide ions. Here we measure an average concentration of $1.3 \times 10^{14} \text{ cm}^{-3}$, i.e. 8 times lower than the average concentration of mobile iodide ions in MAPbI₃, at $1.1 \times 10^{15} \text{ cm}^{-3}$. The lower density of mobile bromide ions will reduce any ion-induced degradation in MAPbBr₃. This lower density probably results from an increase in the energy to form bromide vacancies, which in turn decreases the number of bromide vacancies and thus reduces the number of sites to which bromide ions can migrate.

It is worth mentioning that the concentrations found in the literature still differ by many orders of magnitude, mainly due to the differences in the models used to interpret experimental data⁸⁸ (see Section 2.4.2). The results reported here are consistent with various experimental studies^{53,89-92} that show ion concentrations between 10^{14} and 10^{16} cm^{-3} . Studies that report significantly higher ion concentrations typically assume a complete screening of the electric field in the perovskite⁹³.

Comparing ion migration in MAPbBr₃ and MAPbI₃ thus results in a smaller amount of slower mobile bromide ions, and a striking absence of methylammonium migration. The reduction in mobile ion concentration for MA⁺ is on the order of at least 10^3 , and on the order of 10 for X⁻. Taken together, these results suggest two independent mechanisms for the formation of either methylammonium or halide vacancies, or a combination of two independent mechanisms together with a joint mech-

anism, such as the one proposed by Walsh *et al.* for Schottky defects: $\text{nil} \rightarrow V'_{\text{MA}} + V^{\bullet}_{\text{X}} + \text{MAX}^{32}$. Inhibiting these defect formation reactions is thus essential for enhancing the stability of the MAPbBr₃ perovskite.

2.3 CONCLUSION

We use TID to provide a direct and reliable comparison of ion migration between MAPbBr₃ and MAPbI₃. Our finding is that the activation energy for bromide migration is reduced, contrary to simple bond strength considerations. Despite the reduced activation energy, the diffusion of halides is slower, presumably because of a lower entropic change for ion migration. We note that previously the focus has often been on activation energy when studying ion migration. We show that in addition to the activation energy, it is crucial to consider the entropy change during migration to understand the diffusion of mobile ions. We also find 8 times fewer halide ions migrating in MAPbBr₃ than in MAPbI₃, probably a consequence of the higher vacancy formation energy. Finally, we show that bromide substitution inhibits MA⁺ migration, due to lattice contraction. This suppression of A-cation migration enhances the structural stability of pure-halide perovskites and could be further used as a tool for stabilization of more complex and efficient mixed-cation mixed-halide perovskites.

2.4 APPENDIX

2.4.1 SOLAR CELL FABRICATION AND PERFORMANCE

DEVICE FABRICATION The device fabrication closely follows the one we have established for MAPbI₃ devices in reference [76]. Laser patterned fluoride tin oxide (FTO) glass substrates were cleaned by ultra-sonication for 20 minutes subsequently in detergent, deionized water, acetone, and isopropanol, followed by UV ozone treatment for 15 minutes. Nickel oxide (NiO_x) precursor solution (0.3 M nickel(II) acetylacetonate (Sigma Aldrich) in ethanol) filtered with PTFE 0.45 μm was spun on the cleaned FTO glass at 4000 rpm for 15 seconds, dried at 150 °C for 1 minute and then annealed with a slow heating rate of 3 °C/min until a temperature of 350 °C was reached. The samples were then left at 350 °C for 1 h.

The MAPbBr₃ perovskite precursor solution was prepared by dissolving 1.1 M of methylammonium bromide (MABr, TCI) and lead(II) bromide (PbBr₂, Sigma Aldrich) with 1:1 molar ratio into a 4:1 DMF (anhydrous, Aldrich):DMSO (anhydrous, Aldrich) solvent mix. The dissolution took place overnight on a hot plate at 60 °C. After having cooled, 100 μL of the MAPbBr₃ precursor solution was spun onto the NiO_x-coated substrates at 6000 rpm for 30 seconds in a nitrogen-filled glove box. 15 seconds after the beginning of the rotation, 100 μL of chlorobenzene anti-solvent (anhydrous, Aldrich) was quickly dropped onto the substrate. After the MAPbBr₃ spinning process, the substrates were annealed at 100 °C for 1 h. Following this, 30 nm of C₆₀ (0.2 Å s⁻¹ rate), 8 nm of bathocuproine (0.2 Å s⁻¹ rate) and 120 nm of gold (0.1 Å s⁻¹ for the first 10 nm, then 1.0 Å s⁻¹ for the remaining 110 nm) were deposited on top of the MAPbBr₃ layer by thermal sublimation at pressures below 8 × 10⁻⁶ mbar.

IMAGING OF DEVICE The SEM images were taken with a FEI Verios 460 scanning electron microscope in the secondary electron mode. An acceleration voltage of 10 kV and a working distance of 4 mm were used and field immersion mode was applied for an optimized resolution. To obtain the cross-section of the device, the sample was cleaved in the center.

SOLAR CELL PERFORMANCE The measured V_{OC} of 1.1 V (Figure 2.1d) is much lower than the 2.3 V perovskite bandgap⁹⁴, an effect which is commonly attributed to the mismatch between the energy levels of the MAPbBr₃ perovskite and the transport layers surrounding it. Indeed,

the valence band minimum of MAPbBr₃ (5.9 eV)⁹⁴ and the work function of the NiO_x HTL (5.2 eV)⁹⁵ have an energy difference of $\simeq 0.7$ eV, while the conduction band maximum of MAPbBr₃ (3.6 eV)⁹⁴ and the work function of the C₆₀ ETL (3.9 eV)⁹⁶ have an energy difference of $\simeq 0.3$ eV, amounting to a total loss of $\simeq 1.0$ eV. To counteract this discrepancy, some groups have put efforts in the modification and engineering of interfaces leading to promising V_{OCs} above 1.6 eV⁷⁹. Such interfaces are an important pathway towards optimized devices but here they would prevent a direct one-to-one comparison with our previously reported MAPbI₃ solar cell.

2.4.2 CAPACITANCE MEASUREMENTS

GENERAL CONSIDERATIONS To avoid air exposure, the sample was loaded into a Janis VPF-100 liquid nitrogen cryostat inside a nitrogen-filled glovebox. Current-voltage, impedance spectroscopy, capacitance-voltage, and transient ion-drift measurements were performed at a pressure below 2×10^{-6} mbar, in the dark, using a commercially available DLTS system from Semetrol. To ensure thermal equilibrium, the temperature of the sample was held constant for at least 30 minutes before current-voltage, impedance spectroscopy, and capacitance-voltage measurements. The capacitance was modelled by a capacitor in parallel with a conductance. Capacitance transient measurements were performed from 240 K to 340 K in steps of 2 K with a temperature accuracy of 0.2 K. The sample was held at 240 K for 30 minutes before starting the transient ion-drift measurement.

IMPEDANCE AND MOTT-SCHOTTKY ANALYSIS To perform the TID measurement, we need to properly select the frequency of the AC voltage used to measure capacitance. To do so, we measure the impedance spectrum of our device. As seen in Figure 2.4a, the impedance shows three different regimes: at high frequencies (in this case above 10^5 Hz) the capacitance is limited by the series resistance of the device. At intermediate frequencies (in Figure 2.4a between 10^2 Hz and 10^4 Hz for the capacitance taken at 240 K) lies a plateau where the capacitance is determined by the depletion capacitance, here approximated to a parallel plate capacitor. The discontinuities stem from changes in the resistor over which the capacitance is measured. At low frequencies (in Figure 2.4a below 10^2 Hz for the 240 K capacitance) an additional component arises, and the measured capacitance increases in a fashion that is dependent on the temperature, a phenomenon linked to ion accumulation

at the interfaces^{54,55,89,91,97}. To perform our TID measurement, we thus choose a frequency of 10^4 Hz, in the intermediate frequency regime, where the measured capacitance is influenced neither by ion accumulation nor series resistance.

When measuring TID, we apply a voltage bias to collapse the depletion layer in the perovskite. In order to fully collapse the depletion layer, this voltage bias should be close to the built-in voltage V_{BI} . We determine V_{BI} through Mott-Schottky analysis using the following Equation, where A is the area of the capacitor.

$$\Delta C = A \sqrt{\frac{q \epsilon_0 \epsilon N_D}{2(V_{BI} - V)}} \quad (2.2)$$

In a Mott-Schottky plot, the inverse squared of the capacitance is plotted against voltage. The linear regime of the curve is fitted, then V_{BI} is the intercept of this fit with the x-axis. Figure 2.4b shows a V_{BI} of 1.3 eV for this solar cell architecture. We thus apply voltage pulses of 1.1 V and 1.4 V in our subsequent TID measurements. Two other parameters can be extracted from a Mott-Schottky plot: the density of electronic doping N_D , and the perovskite permittivity ϵ . Similar to our TID assumption, we assume again that the mobile ion density is smaller than the electronic doping density, such that the ions only pose a small perturbation. Within this framework, the electronic doping density N_D evolves with the applied voltage and is thus determined by the slope of the Mott-Schottky curve. On the contrary, at full depletion the perovskite permittivity ϵ does not evolve with the applied voltage, and is thus extracted from the capacitance value in the plateau regime, in our case at 0 V. The results for N_D and ϵ are given in the inset of Figure 2.4b. These values are used for solving Equation 2.4 and Equation 2.5. We note that this Mott-Schottky analysis assumes the validity of the depletion approximation for the perovskite solar cells measured⁹⁸. Indeed two slopes appear in the Mott-Schottky plot, one related to the depletion capacitance, the second to the chemical capacitance, due to charge-carrier injection at high forward biases. By considering only the slope at intermediate forward bias, we make sure we measure the depletion capacitance.

TRANSIENT ION DRIFT Three key parameters can be quantified by TID: the activation energy for ions to migrate, E_a , the ion diffusion coefficient prefactor, D_0 , and the mobile ion concentration, N_{ion} .

These can be extracted using the following set of equations, where

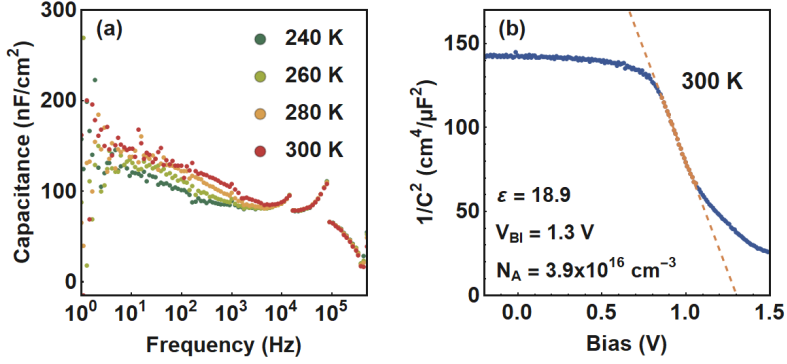


FIGURE 2.4. (a) Impedance spectroscopy measured in the dark at 0 V with an AC perturbation of 10 mV, (b) Mott-Schottky characteristics measured at 300 K in the dark with an AC perturbation of 10 mV at 10⁴ Hz.

$C(\infty)$ is the capacitance at steady-state, C_0 is the initial capacitance at time $t = 0$ after releasing the voltage pulse, ΔC is the magnitude of the transient, ϵ_0 is the vacuum permittivity, ϵ is the perovskite permittivity, q is the electric charge, and N_D is the electronic doping density. The assumptions of the model are detailed in Chapter 1.

$$C(t) = C(\infty) \pm \Delta C \exp\left(\frac{-t}{\tau}\right) \quad (2.3)$$

$$\tau = \frac{k_B T \epsilon_0 \epsilon}{q^2 D_0 N_D} \exp\left(\frac{E_a}{k_B T}\right) \quad (2.4)$$

$$\Delta C = C(\infty) - C_0 = C(\infty) \frac{N_{ion}}{2 N_D} \quad (2.5)$$

The fitting procedure goes as follows. To obtain the time constants for ion migration, each capacitance transient is fitted individually with a function containing between one and four exponential decay components. Within our chosen confidence level (p value > 0.05), most capacitance transients are fitted with a mono-exponential decay. These are shown in red in Figure 2.2 and in Figure 2.5. The obtained values for E_a , D_0 , and N_{ion} and their error bars are presented in Table I and Figure 2.3. The errors are calculated using the standard deviation of four measurements, each weighed by the error on its fit.

We note that the values presented in Table I in Section 2.2.3 are calculated under the assumption that the perovskite permittivity is

temperature-independent in the range considered, using the value found at 300 K. We also note that our values for the perovskite permittivity follow a similar trend to previous works^{99–103}, with an almost constant value from 240 K to 300 K as apparent from the almost constant capacitance at long times, see Figure 2.5. This assumption might, however, break for temperatures above 300 K. If we assume instead a temperature-dependent perovskite permittivity calculated from the steady-state capacitance, we find only small changes in the extracted values, where the activation energy changes from (0.25 ± 0.05) eV to (0.26 ± 0.10) eV, and the diffusion coefficient from $(8.4 \pm 3.9) \times 10^{-10}$ cm²s⁻¹ to $(8.7 \pm 4.2) \times 10^{-10}$ cm²s⁻¹.

We use Equation 2.5 to estimate the minimum sensitivity threshold to detect a migrating species, with $N_{ion}(min) = \frac{\Delta C}{C(\infty)} \times 2N_D \simeq 3.7 \times 10^{-4} \times 2N_D$ cm⁻³. Below this value – i.e. in this study below 1.5×10^{13} cm⁻³ – we are unable to detect a mobile ionic species. We would further not be able to detect an ionic species with a positive charge if it had a very similar activation energy and diffusion constant as the negative feature. The combination of these factors is highly unlikely, and we thus conclude that there is probably no mobile positively charged ion with a density above 1.5×10^{13} cm⁻³.

While fitting the data, we notice a discontinuity in the very first points measured, before the expected exponential decay arises. We hypothesize this effect to be due to a circuit overload in the first milliseconds. In our subsequent fitting procedure, we thus use the data from time 2.5 ms (point number 7 of the measurement) to time 1 s (point number 2042).

For a few filling voltages, the high-temperature fits do not match the Arrhenius trend. These fitted values are shown in blue in Figure 2.5. The component is slow ($50 \text{ ms} < \tau < 200 \text{ ms}$) and of low amplitude such that we are not able to assign an activation energy to this process. Because these arise only at high temperatures, and mostly at higher filling voltages, we hypothesize a reversible interfacial effect between the perovskite layer and the contact layers.

CAPACITANCE TRANSIENTS AND ARRHENIUS PLOT FOR A FILLING VOLTAGE OF 1.4 V In Figure 2.5 below, we show the capacitance transients and the Arrhenius plot for a MAPbBr₃ solar cell measured after applying a filling bias of 1.4 V for 1 s (as opposed to 1.1 V in Figure 2.2). From the Arrhenius plot, we extract the activation energy for the migration step $E_a = 0.220 \pm 0.05$ eV, and find that this value is equivalent to the one obtained when applying the 1.1 V filling bias, where

$$E_a = 0.222 \pm 0.04 \text{ eV.}$$

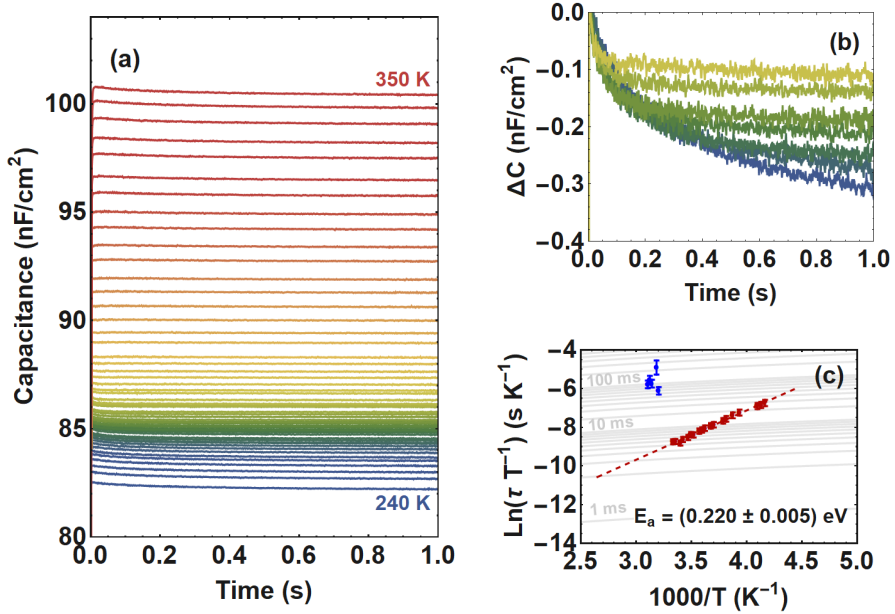


FIGURE 2.5. (a) Capacitance transient measurements of a MAPbBr₃ solar cell measured in the dark, with a DC voltage of 0 V and an AC voltage of 10 mV at 10⁴ Hz, after applying a pulse of 1.4 V for 1 s. (b) Relative difference in capacitance $\Delta C = C(t) - C_{2.5 \text{ ms}}$ for the capacitance transients between 240 K and 300 K. (c) Arrhenius plot showing the activation energy derived from this measurement, in red. In blue are the high-energy temperature points that we associate to a reversible interfacial effect between the perovskite and the contact layers.

3 A MIX OF HALIDES

REDUCED BARRIER FOR ION MIGRATION IN MIXED $\text{MAPb}(\text{Br}_x\text{I}_{1-x})_3$ PEROVSKITES

Halide alloying in metal halide perovskites is a useful tool for optoelectronic applications requiring a specific bandgap. However, mixed-halide perovskites show ion migration in the perovskite layer, leading to phase segregation and reducing the long-term stability of the devices. Here, we study the ion migration process in methylammonium-based mixed-halide perovskites with varying ratios of bromide to iodide. We find that the mixed-halide perovskites show two separate halide migration processes, in contrast to pure-phase perovskites which only show a unique halide migration component. Compared to pure-halide perovskites, these processes have lower activation energy, facilitating ion migration in mixed versus pure-phase perovskites, and have a higher density of mobile ions. Under illumination, we find that the concentration of mobile halide ions is further increased and notice the emergence of a migration process involving methylammonium cations. Quantifying the ion migration processes in mixed-halide perovskites shines light on the key parameters allowing the design of bandgap-tunable perovskite solar cells with long-term stability.

This chapter is based on the following publication¹⁰⁴:

Lucie McGovern, Gianluca Grimaldi, Moritz H. Futscher, Eline M. Hutter, Loreta A. Muscarella, Moritz C. Schmidt, Bruno Ehrler, "Reduced Barrier for Ion Migration in Mixed-Halide Perovskites", *ACS Applied Energy Materials*, vol. 4, no. 12, pp. 13431–13437, 2021.

3.1 INTRODUCTION

Perovskite solar cell efficiencies have increased rapidly in the past decade and now reach an impressive 25.5 % power conversion efficiency in single-junction cells, closely matching up with the 26.7 % record for silicon solar cells¹⁰. On top of these high efficiencies, another key advantage with perovskites lies in the bandgap tunability of the material, easily achievable through mixing of the A, B, and X elements composing the ABX_3 perovskite structure¹¹. For example, halide alloying has been shown to allow for a large variation in the bandgap, from 1.6 eV to 3.2 eV in methylammonium-based $MAPbX_nY_{3-n}$ perovskites - with (X,Y) consisting of either I, Br, or Cl. The main factor impeding large-scale commercialization of perovskite devices remains the issue of their stability in time, with only a handful of perovskite devices showing the necessary stability under accelerated lifetime conditions. In that regard, the more intrinsically stable the perovskite layer, the easier it will be to stabilize the full devices.

For mixed-halide systems, the instability is commonly observed through the photoinduced phase segregation process, in which light induces de-mixing of the perovskite composition, leading to the formation of iodide-rich and bromide-rich phases within the film¹⁰⁵. Photoinduced phase segregation relies on the migration of the halide species through the perovskite film, linking it to the larger topic of ion migration in perovskite solar cells. At its core, ion migration is a process by which ions from the lead halide $APbX_3$ structure become mobile and hop through the perovskite lattice. This leads to long-term stability issues, as the process might not be fully reversible^{106–108}. Combining bandgap tunability with long-term stability is crucial for the further development of perovskite devices. To this end, a better understanding of the ion migration process in mixed-halide systems is needed, to determine specific parameters of influence that can aid to mitigate or suppress this feature altogether.

During illumination, the observation of halide ion migration is easily accessible through monitoring of the photoinduced phase segregation, using UV/visible absorption, PL emission spectroscopy and/or transient absorption spectroscopy^{69,109–115}. In the absence of segregation however, which is the case when the cells are in the dark or when the mixing ratio

of bromide to iodide falls below the 0.2 threshold¹⁰⁵, we need other tools to characterize the ion migration processes at play. So far there have only been a limited number of studies focussing on these regimes, using AC impedance spectroscopy or DC polarisation measurements^{116,117}. While these works shed light on ion migration in mixed-halide perovskites, the full picture remains elusive, specifically whether the trends observed stem from iodide or bromide migration, and how to attribute the relative contributions to the ion migration process, in terms of migration activation energy, ion diffusion coefficient and concentration of mobile ions.

Transient Ion Drift (TID) can be used for ion migration measurements in dark as well as in light conditions, and provides a detailed description of the process, revealing the nature of the mobile ion (whether anion or cation), and allowing for the quantification of the activation energy E_a , diffusion coefficient D_{ion} and concentration N_{ion} of mobile ions^{51,118}. With this work, we aim to answer the following questions: i) how does the mixing ratio of bromide to iodide change the ion migration process for the perovskite devices; ii) how does light affect this ion migration process. To answer these questions, we prepare perovskite solar cells with varying ratios of bromide to iodide, measure the TID capacitance transients in these devices, and finally fit these transients in order to extract the ion migration characteristics E_a , D_{ion} and N_{ion} of the various mixed-halide perovskite compositions.

3.2 RESULTS AND DISCUSSION

3.2.1 MIXED-HALIDE SOLAR CELL FABRICATION

In order to study the effect of bromide to iodide ratio on the ion migration process, we prepare solar cell devices with the composition $\text{MAPb}(\text{Br}_x\text{I}_{1-x})_3$, and vary the x ratios ($x = 0.1, 0.2, 0.5$ and 0.7) following a synthesis described in Section 3.4.1. For reliable comparison with our previously-published pure halide devices^{56,76}, we use the same device structure (see Figure 3.1a). To characterize these devices, the dark IV curves are presented in Figure 3.1b. These curves show a hysteretic behaviour for most of the solar cells considered, an effect typically associated with the formation of interfacial charges between the perovskite and the transport materials⁸⁹. The main requirement for successful TID characterisation is a low series resistance, so that the measured signal can be related to the capacitance of the perovskite when a small AC voltage is applied. The series resistance is determined by fitting the Nyquist

plots (see Section 3.4.2) and is found to be below $20 \Omega \text{ cm}^2$ throughout the bromide to iodide ratios used in this study. The dark IV curves presented here are consistent with those found in the literature for devices with similar perovskite and transport materials²⁹.

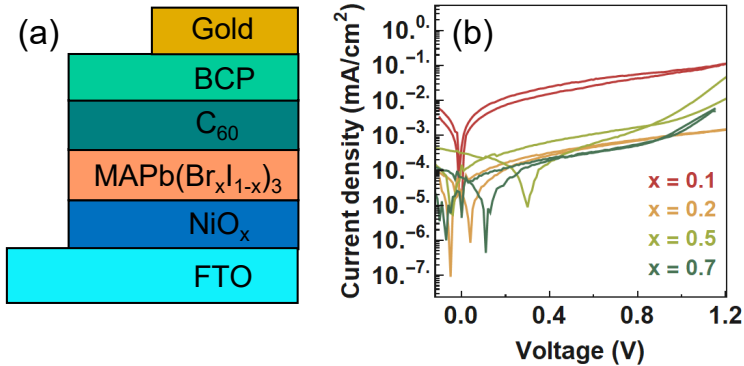


FIGURE 3.1. a P-i-n device architecture of the $\text{MAPb}(\text{Br}_x\text{I}_{1-x})_3$ perovskite solar cells, using $x = 0.1, 0.2, 0.5$ and 0.7 , and their corresponding (b) dark-IV curves measured with a scan speed of 10 mV s^{-1} , presented on a semi-log scale.

3.2.2 CAPACITANCE MEASUREMENTS OF THE MIXED-HALIDE SOLAR CELLS

TID is an electronic spectroscopy technique aimed at characterising ion migration processes in semiconductor devices^{51,118}. We measure the capacitance transients of the $\text{MAPb}(\text{Br}_x\text{I}_{1-x})_3$ perovskite solar cells at different temperatures after applying a voltage pulse of 1.5 V for 2 s (see Section 3.4.2). We note that we choose the 1.5 V voltage pulse such that it is both high enough to detect the ion dynamics with TID (see the comparison with TID after application of voltage biases of 1 V or 1.25 V in Section 3.4.2) while remaining below the threshold for electrically-induced phase segregation^{119,120}. The results are plotted in Figure 3.2 as the relative difference in capacitance, i.e. $\Delta C = C(t) - C_0$, with $C(t)$ the capacitance as a function of time and C_0 the capacitance at time $t = 0$. These transients already provide a qualitative picture of ion migration in these mixed-halide perovskite systems. In dark, we find that the capacitance decays for all the halide ratios considered. In p-type perovskites, negative capacitance transients are associated with migration

from an anion species. Since the only negatively charged species in ABX_3 is the X^- halide ion, this signals migration of a halide species. This assignment is similar to what we have previously found in both pure-halide perovskites, $MAPbI_3$ and $MAPbBr_3$ ^{56,76}. Note that the doping of the perovskite layer is a matter of active debate (assigned to n-type¹²¹, p-type¹²² and intrinsic¹²³). The observed feature could thus correspond to halide migration, but other assignments remain possible (cation or halide vacancy migration in an n-type material, cation vacancy migration in p-type material). The negative feature observed here shares many properties with halide migration observed directly^{42,49}, and we hence assign it to halide migration for the remainder of the discussion. For $x = 0.1$, there is a small positive signal visible for the highest temperatures, at 315 K and 330 K, but this positive trend remains very small compared to the main negative trend observed. We additionally measure the capacitance transients under illumination for $x = 0.1$ and 0.2. The devices with $x = 0.5$ and 0.7 could not be measured during illumination, because the light-induced phase segregation would change the sample in a non-reversible way during the capacitance measurements. The results under illumination show a different picture than those in the dark, where on top of the negative transient present at all temperatures, a new positive trend becomes clearly visible after 100 to 200 milliseconds, for the whole temperature range considered. Since we are considering p-type perovskites, we attribute this positive trend to cation migration. As lead migration is energetically unfavourable³³, we assign the feature to methylammonium cation migration. Finally, we also observe a general growth in the magnitude of the negative capacitance transients compared to dark conditions. Under light conditions, the relative capacitance difference is highest for $x = 0.2$, with $\Delta C = -10 \text{ nF cm}^{-2}$.

3.2.3 QUANTIFICATION OF ION MIGRATION CHARACTERISTICS

To obtain a more quantitative picture of the ion migration process, we fit the TID capacitance transients to the following Equation:

$$C(t, T) = C_\infty(T) + \sum_n \Delta C_n(T) \exp\left(\frac{-t}{p_{fit(n)} T \exp\left(\frac{E_{a(n)}}{k_B T}\right)}\right) \quad (3.1)$$

where $C(t, T)$ is the capacitance as a function of time and temperature, $C_\infty(T)$ is the steady-state value of the capacitance at a certain temperature T , $\Delta C_n(T)$ is the capacitance magnitude at temperature

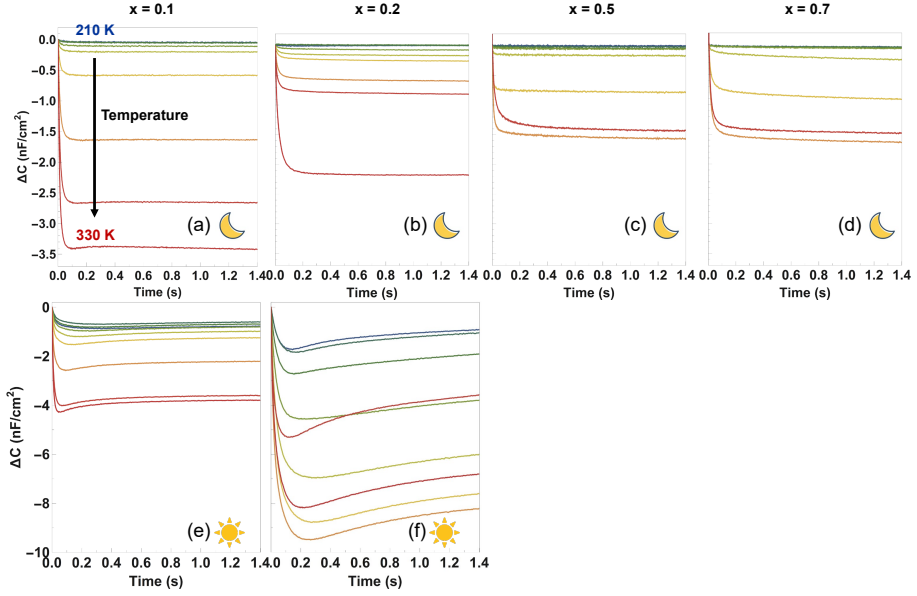


FIGURE 3.2. Relative difference in capacitance transients $\Delta C = C(t) - C_0$ of the $\text{MAPb}(\text{Br}_x\text{I}_{1-x})_3$ solar cells, measured with an AC voltage of 20 mV, after applying a voltage pulse of 1.5 V for 2 seconds, under dark conditions, for (a) $x = 0.1$, (b) $x = 0.2$, (c) $x = 0.5$ and (d) $x = 0.7$, and during illumination, for (e) $x = 0.1$, (f) $x = 0.2$. The transients shown here are taken at temperatures of 210 K, 225 K, 240 K, 255 K, 270 K, 285 K, 300 K, 315 K and 330 K. Light conditions correspond to a 405 nm CW laser shining directly on the considered pixel, with a power density of 1.59 W cm^{-2} .

T of the process n , $p_{fit(n)}$ is a fitted parameter for process n that depends on the diffusion coefficient, and $E_{a(n)}$ is the activation energy of the process n . Every migration pathway would correspond to an individual exponential decay, and for the mixed-halide perovskites we can fit the data with two or three decay traces, respectively under dark and illumination conditions.

The fit is obtained by using a global fit algorithm as described in Section 3.4.3. The values obtained for the ion migration activation energy, ion diffusion coefficient and density of mobile ions are shown in Figure 3.3. For comparison, we add the values for MAPbI_3 and MAPbBr_3 , reproduced from references [56, 76]. When fitting the capacitive transients, we find that we need 2 exponential contributions to correctly fit the negative peak, whether in dark or in light, and across the full composition range

from $x = 0.1$ to $x = 0.7$. This means that for methylammonium-based mixed-halide perovskites, there are 2 halide migration processes at play, either from the iodide and the bromide species, or from the combination of a grain boundary process with a bulk process, similar to what we have previously observed for MAPbBr₃ cells with varying grain size¹²⁴. This is in stark contrast with the single halide migration process happening in the pure-phase halide perovskites. The small positive peak present in dark for $x = 0.1$ is too low to be fitted, suggesting that the concentration of mobile methylammonium ions in this case is below 10^{14} cm^{-3} (considering the hypothesis of a high doping density of 10^{17} cm^{-3} , see Sections 3.4.2 and 3.4.3). To fit the capacitance transients taken under illumination, 3 exponential contributions are used, where 2 are assigned to the negative halide peak, and 1 to the positive methylammonium peak.

ION MIGRATION UNDER DARK CONDITIONS Looking at Figure 3.3a, we notice that both activation energies from the halide migration process are decreased in mixed-halide compositions compared to the single ion migration activation energies from the pure-halide compositions. Specifically, for the first process contributing to halide migration - with highest activation energy, labelled Halide (1) in Figure 3.3 - the activation energy is most decreased in the low-bromide regime, with $E_a = 157 \pm 3 \text{ meV}$ for $x = 0.1$ and $E_a = 98 \pm 7 \text{ meV}$ for $x = 0.2$, then increases to $E_a = 289 \pm 10 \text{ meV}$ for $x = 0.5$ and $E_a = 217 \pm 11 \text{ meV}$ for $x = 0.7$. The trend is similar for the second process contributing to halide migration - with lower activation energy, labelled Halide (2) in Figure 3.3 - with a maximal value of $E_a = 139 \pm 14 \text{ meV}$ for $x = 0.5$. García-Rodríguez *et al.*¹¹⁶ show an increase in the activation energy with higher bromide concentration, in their case using bromide concentrations below 10%. Here, we find that halide migration has a lower activation energy in mixed devices for bromide contents of 10, 20, 50 and 70%.

Figure 3.3b shows the halide diffusion coefficients in the dark. The diffusion coefficient of both contributions is constant for different bromide concentrations. The diffusion coefficient of Halide (1) is on the order of 10^{-9} to $10^{-10} \text{ cm}^2 \text{ s}^{-1}$, similar - within the error bar - to the iodide and bromide diffusion coefficients in MAPbI₃ and MAPbBr₃. Halide (2) on the other hand is slower, on the order of $10^{-11} \text{ cm}^2 \text{ s}^{-1}$. Halide migration is thus equally fast in all the mixed devices.

Figure 3.3c shows the density of mobile halide ions. The Halide (2) peak has a relatively constant and similar concentration to the bromide and iodide mobile ion densities found in the pure-phase perovskites. The

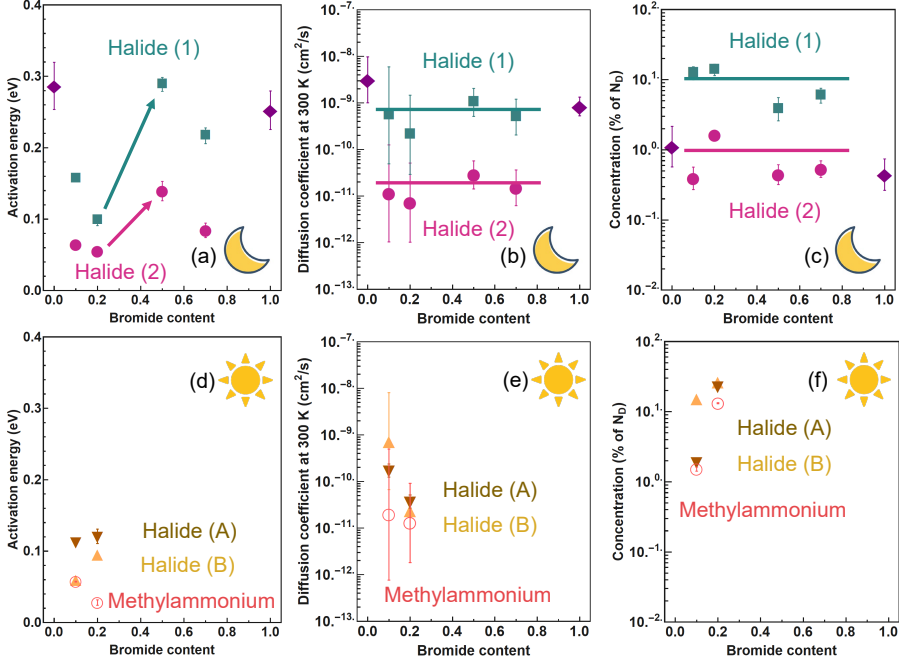


FIGURE 3.3. Comparison of the characteristics of ion migration as a function of the bromide to iodide ratio. Halide ion migration characteristics in dark, with (a) ion migration activation energies, (b) halide ion diffusion coefficients at 300 K, and (c) concentration of mobile halide ions, represented as a fraction of the doping density. The two migration processes Halide (1) and Halide (2) are shown in blue and pink, respectively. The arrows in (a) represent the point of phase transition, the lines in (b) and (c) are a guide to the eye representing the weighted averages for diffusion coefficient and mobile ion concentration. The halide and methylammonium ion migration characteristics in light are respectively shown in dark and light orange - Halide (A) and Halide (B) - and in red, with (d) ion migration activation energies, (e) halide and methylammonium ion diffusion coefficients at 300 K, and (f) concentration of mobile ions. Error bars represent the standard deviation of the fit parameters from several fits giving lowest chi-square values (see Section 3.4.3). The values for $x = 0$ and $x = 1$ are reproduced from references [56, 76].

peak for Halide (1) on the other hand shows a clear increase in the concentration of migrating halide ions compared to the pure-phase cases, with up to 10% of the doping density for the devices with 10% and 20% bromide concentrations. There is thus more halide migration in the mixed devices.

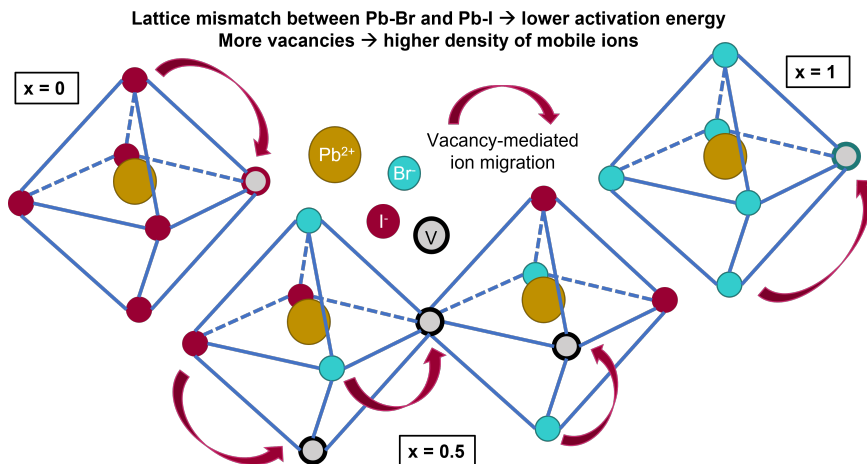


FIGURE 3.4. Schematic picture of the ion migration process in the pure-halide perovskites compared to the mixed-halide perovskites. The lattice mismatch between the bromide and iodide perovskite lattices in the mixed-halide case leads to a decreased activation energy for the migration step. The number of vacancies is also higher for the mixed-halide case, thereby increasing the density of mobile halide ions in the mixed-halide perovskites.

ILLUSTRATIVE SCHEME One possible scheme to rationalise these observations is to consider the two processes separately. Halide (1) shows a high density of ions which presumably arises from an increased density of vacancies when moving from pure-halide to mixed-halide compositions. The difference in solubility of iodide and bromide species has indeed been suggested to result in heterogeneous nucleation during thin-film deposition¹²⁵ and has led to the observation of lower crystallinity in the mixed films¹²⁶, which could in turn lead to an increase in the density of halide vacancies. The Halide (1) process would thus become more prominent for mixed-halides due to the higher number of vacancies. This is in line with the finding that the fraction of halide vacancies enables and controls the rate of phase segregation^{40,110}. Overall, the Halide (1) process shares many features with the halide migration in pure-halide perovskites. It has a similar diffusion coefficient and a slightly reduced activation energy, especially for the mixing ratios $x < 0.2$. This reduction in activation energy could be associated with the strain in the crystal from the different bond length between bromide and iodide¹²⁷, in which case the activation energy should be lowest close to the phase transition. A reduced activation energy might naively lead to an increase diffusion coefficient. However, in the mixed halide perovskites the entropy is likely to decrease

when the ion is moving, since it is most likely coming from a well-mixed unit cell. The effect would be accentuated if the ions are moving towards a transport layer, as the mobile halide will accumulate there and likely end up in a unit cell enriched in one of the halides. The maximal entropy difference for a mobile halide ion to migrate is the entropy difference $\Delta S = k \ln \frac{8!}{4! \times 4!} = 3.6 \times 10^4 \text{ eV K}^{-1}$, where the argument of the logarithm represents the ratio between the number of possible configurations for the neighbours of an ion in a mixed-halide phase of $x = 0.5$ (i.e. $\frac{8!}{4! \times 4!}$) and the number of configurations for neighbouring ions in a single-halide phase (i.e. 1). While we expect this effect to be large in the well-mixed perovskites ($x < 0.2$), the higher bromide ratios already show some de-mixing even in the dark and when a bias is applied^{128,129}, which means that the entropy change during migration towards the interfaces is smaller. Taken together, the reduced activation energy and entropy gain appear to balance each other, resulting in a rather constant diffusion coefficient at room temperature. A representation of this scheme is depicted in Figure 3.4.

Halide (2) represents a very slow ion with a low activation energy. The diffusion coefficient is about 2 orders of magnitude lower than that of Halide (1). Presumably, even if present, this process cannot be detected easily in pure-halide mixtures as also the concentration is about 2 orders of magnitude lower than Halide (1). We speculate that a similar process could be responsible for the very slow dynamics (minutes to days) often seen in perovskite devices¹³⁰. The observation of the difference in the activation energy for migration before and after the $x = 0.2$ mark - with much lower migration barriers for the perovskites with low-bromide content - is also noteworthy. The $x \geq 0.2$ threshold marks the onset of light-induced phase segregation in mixed-halide perovskites and is thought to arise due to the phase transition (from tetragonal to cubic) close to this composition. Here this threshold is clearly visible in the ion migration properties of the devices, reinforcing the relationship between perovskite composition, phase segregation and ion migration instability.

ION MIGRATION UNDER ILLUMINATION When comparing halide migration in dark and in light, we find that the activation energy is decreased in light, see for instance for the perovskite with 10% bromide, the small decrease from $65 \pm 5 \text{ meV}$ to $60 \pm 3 \text{ meV}$ for the first peak, and the larger decrease from $157 \pm 3 \text{ meV}$ to $113 \pm 4 \text{ meV}$ for the second peak. This is consistent with our previous work on these systems¹¹⁵. We note that the similar activation energies between Halide (1) and Halide (A) seem to

suggest the same process, but that TID cannot distinguish mechanisms, complicating the assignments of the Halide (1) and Halide (2) peaks in light. We thus choose the nomenclature Halide (A) and Halide (B) for the halide migration peaks in light. When comparing the diffusion coefficients in dark and in light, no clear trend seems to emerge as there is both an increase in one of the features, and a decrease in the other. The most noticeable difference lies in the concentration of mobile halide ions, with a clear increase in the total halide concentration as a function of doping density, from 12.8% to 17.3% for $x = 0.1$, and from 15.4% to 36.9% for $x = 0.2$. Under light, there is thus an increased halide ion migration, partly due to a lower activation energy, and mostly due to the much larger fraction of mobile halide ions. We note that at such high densities the quantification of ion migration by TID might not be accurate anymore because the analysis method assumes that the change in the charge density from mobile ions is small compared to the background doping density.

As mentioned above, in the presence of light, a new cation migration process appears for the devices with $x = 0.1$ and $x = 0.2$, on top of the halide migration process. This process has a very low activation energy (< 0.060 eV), has a low diffusion coefficient on the order of 10^{-11} cm² s⁻¹, and is prominent, representing 1.5% and 13.2% of the doping density, respectively for the devices with 10% and 20% bromide concentrations. So far in dark, we have only observed MA⁺ migration in the case of the pure MAPbI₃ perovskite, and in this work as a minor contribution to the MAPbBr_{0.3}I_{2.7} perovskite. In other words, the higher the bromide concentration, the more methylammonium migration is suppressed, as the bond between lead and halide gets stronger. Under light conditions, it thus seems like the barrier preventing cation migration is released, in agreement with galvanostatic measurements from Zhao *et al.*¹³¹ showing decreased activation energies with increasing light intensity. This effect might happen either through an increase in the number of MA⁺ vacancies in light -similar to the increase of halide vacancies observed in light¹³²- and/or through a loosening of the Pb-X bond, perhaps upon polaron formation^{133,134}. We also note that one of the theories behind light-induced phase segregation involves polaron stabilization of the iodide domains. One possibility is that halide migration might promote this effect, while cation migration might prevent it: there, the reduction (or suppression) of cation migration in light when $x > 0.2$ would help rationalize the $x = 0.2$ threshold observed in light-induced phase segregation. This calls for future investigation.

All in all, light thus has two effects on the ion migration process for the mixed-halide perovskites: first, it increases the number of mobile halide ions; second, it introduces an extra cation migration pathway. These results are in line with the previous work from Kim *et al.*¹¹⁷, showing increased ionic conductivity in light compared to dark for similar perovskite compositions. In conductivity measurements, however, the contributions from diffusion coefficient and mobile ion density cannot be disentangled: here, we can thus specifically attribute the increased ion migration in light to an increase in the mobile ion density.

3.3 CONCLUSION

In conclusion, we find that mixing iodide and bromide in $\text{MAPb}(\text{Br}_x\text{I}_{1-x})_3$ solar cells facilitates halide ion migration by decreasing the activation energy and by increasing the number of mobile halide ions. We also notice the appearance of a second pathway in the halide ion migration process, not observed in the pure-phase perovskites. In light, the density of mobile halide ions increases even more, and additional migration from the methylammonium cation becomes prominent. To reduce ion migration in mixed-halide perovskites, it is thus essential to increase the activation energy of the process and/or to decrease the density of mobile halide ions. These can be achieved for instance by reducing the unit cell size by replacing MA^+ with Cs^+ (E_a increase)¹¹⁵, or by tailoring the Pb:X stoichiometry to reduce the number of halide vacancies (N_{ion} decrease)¹²². Our quantitative assessment of the ion migration processes in mixed-halide perovskites thus provides new insights into the relative contributions of activation energy, ion diffusion and mobile ion density, tracing the path towards rational design of mitigation strategies, necessary for long-term stability of bandgap-tunable perovskite solar cells.

3.4 APPENDIX

3.4.1 SOLAR CELL DEVICE FABRICATION

The substrates are laser-patterned Fluorinated Tin Oxide (FTO)-coated glass substrates. We clean them with 3 successive rounds of sonication of 15 minutes each, in deionized water, acetone, and isopropanol; and further plasma clean them for 20 minutes at 100 W.

The NiO_x Hole Transport Layer (HTL) is prepared by dissolving the precursor (nickel(II) acetylacetonate, Sigma Aldrich) in ethanol at a concentration of 0.3 M. The solution is then filtered with a PTFE membrane of diameter 0.45 μm, and then spin coated on the cleaned FTO glass at 4000 rpm for 15 seconds. The as-prepared film is dried at 150 °C for 1 minute and then annealed with a slow heating rate of 3 °C/min until a temperature of 350 °C is reached. The samples are then left at 350 °C for 1 h, and further plasma cleaned for 20 minutes at 100 W before the perovskite spin coating step.

The perovskite synthesis has been previously described in reference [114] and goes as follows. To prepare the perovskite solutions, we first mix DMF and DMSO in a 4 : 1 (DMF:DMSO) volume ratio. We then dissolve PbI₂ (TCI, 99.99 %, trace metals basis), CH₃NH₃I (TCI, > 99 %), PbBr₂ (Sigma-Aldrich, trace metals basis), and CH₃NH₃Br (TCI, > 98 %) precursors in this solvent mixture, with molar ratio of 1.1 M. These stock solutions are then mixed (PbI₂ with CH₃NH₃I, and PbBr₂ with CH₃NH₃Br) to obtain MAPbI₃ and MAPbBr₃ solutions, using a 1 : 1 molar stoichiometric ratio. The MAPb(Br_xI_{1-x})₃ precursor solutions are then prepared by mixing x parts MAPbBr₃ stock solution with $(1 - x)$ parts MAPbI₃ stock solution, resulting in 1.1 M MAPb(Br_xI_{1-x})₃ solutions. The perovskite films are prepared by spin coating the precursor solutions onto the NiO_x-coated FTO substrates, with a spin speed of 9000 rpm for 30 s. The chlorobenzene (Sigma-Aldrich, anhydrous, ≥ 99 %) anti-solvent is dropped 15 s after the start of spin coating. The film is then annealed at 100 °C for 1 h.

We note that the devices with pure MAPbI₃ and pure MAPbBr₃ were prepared in a similar fashion, with only a few differences: the MAPbI₃ solution has a concentration of 1.35 M in pure DMF, and is spin coated for 25 seconds at 5000 rpm, with addition of the chlorobenzene anti-solvent after 5 seconds; the MAPbBr₃ solution is spin coated at 6000 rpm for 30 seconds.

The C₆₀ and BathoCuProine (BCP) Electron Transport Layers

(ETL), as well as the gold electrode are thermally evaporated: 30 nm of C_{60} (0.2 \AA s^{-1} rate), 8 nm of BCP (0.2 \AA s^{-1} rate) and 120 nm of gold (0.1 \AA s^{-1} for the first 10 nm, then 1.0 \AA s^{-1} for the remaining 110 nm). The pressure remained below 8×10^{-6} mbar during all thermal evaporation steps. The preparation and spin coating of the perovskite solutions are done in a nitrogen-filled glovebox, while the spin coating of NiO_x is done in a downflow cabinet.

An example SEM image of the as-prepared $MAPbBr_{1.5}I_{1.5}$ perovskite film is shown below (Figure 3.5), with apparent grains of size 300 nm to $1 \mu\text{m}$. SEM imaging was done using a FEI Verios 460 instrument. The perovskite film thicknesses are measured by profilometry, using a KLA Tencor stylus profiler P7 instrument.

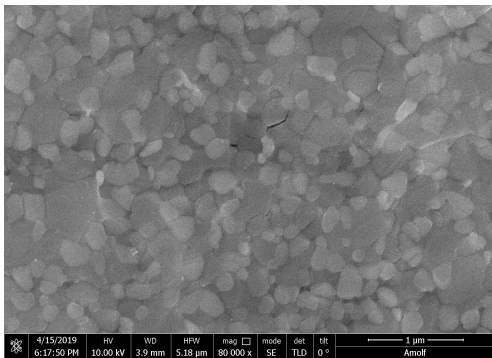


FIGURE 3.5. SEM image of the $MAPbBr_{1.5}I_{1.5}$ perovskite film, showing a flat and homogeneous layer with features between 300 nm and $1 \mu\text{m}$.

We have previously published the PL spectra, absorption spectra and XRD diffractograms of the $MAPb(Br_xI_{1-x})_3$ films prepared by this synthesis recipe¹¹⁴. These measurements confirm that the films have a comparable and controlled quality for the whole range of x-ratios used. From the absorption spectra and XRD diffractograms we observe that both the bandgap and the unit cell size scale with the x-ratio, and that on a macroscopic level, the halides are homogeneously mixed. Finally, the peaks around 15 and 30 degrees observed in XRD for $0.25 < x < 1$ have similar FWHM, reflecting the constant trend in grain size for these films.

In the full devices, we note that we choose the same device structure as our previously-published pure halide devices^{56,76}. In this context, NiO_x and C_{60} / BCP are chosen specifically with the aim of avoiding ion migration from the transport layers themselves – a process commonly reported for traditional HTL and ETL such as Spiro-OMeTAD¹³⁵ and

TiO₂¹³⁶. We can thus safely assume that the effects observed in this study stem from the perovskite layers themselves.

To observe the effect of illumination on the ion migration properties of the mixed-halide devices, we use the following illumination conditions: a 405 nm CW laser is focused on the considered pixel, using a 1 mW beam and a spot size of $6.3 \times 10^{-4} \text{ cm}^2$, amounting to a power density of 1.59 W cm^{-2} .

3.4.2 ELECTRICAL MEASUREMENTS

The TID technique has been extensively described elsewhere^{51,118}. To resolve the Equation for the ion diffusion coefficient (see Equation 3.1), we need both the perovskite permittivity ϵ and the doping density N_D of the film. We get these by performing Capacitance versus Voltage (CV) measurements, as shown in Figure 3.6. These show $\epsilon = 38.6$ and $N_D = 1.98 \times 10^{16} \text{ cm}^{-3}$ for the MAPbBr_{1.5}I_{1.5} film, above the threshold for experimentally accessible charge densities for the perovskite film thicknesses considered here, as defined by Kirchartz *et al.*¹³⁷. For $x = 0.7$, we use $\epsilon = 17.2$ and $N_D = 2.53 \times 10^{16} \text{ cm}^{-3}$ as determined by CV measurement. In the cases of $x = 0.1$ and $x = 0.2$, CV measurements were not conclusive in the determination of N_D , and we use instead the average found by combining the doping densities of the devices with $x = 0$, $x = 0.5$, $x = 0.7$, and $x = 1$, which is $4.39 \times 10^{16} \text{ cm}^{-3}$. To account for possible discrepancies in the determination of the diffusion coefficient - which is based on N_D - we consider a large error bar for N_D in these two cases, with a lower bound of 10^{16} cm^{-3} and an upper bound of 10^{17} cm^{-3} . This is reflected in the large error bars for the diffusion coefficient values as shown in Figure 3.3b,e.

To further characterize the cells, we perform Thermal Admittance Spectroscopy (TAS) on the MAPb(Br_xI_{1-x})₃ solar cells. The results shown in Figure 3.7 present a constant capacitance plateau in the intermediate frequency range, which spans from 10^2 Hz to $5 \times 10^4 \text{ Hz}$ for the devices with $x = 0.1$ and $x = 0.2$, and from $5 \times 10^3 \text{ Hz}$ to $5 \times 10^4 \text{ Hz}$ for the devices with $x = 0.5$ and $x = 0.7$. This region of constant capacitance is the region where we measure the geometric capacitance of the device, where capacitance is determined by the depletion capacitance. This is the reason why we choose a frequency of 10^4 Hz for all the TID measurements, within that region of interest. In light, we notice that the low-frequency regime, representative of ion movement back and forth close to the interfaces, increases drastically, with 4 orders of magnitude

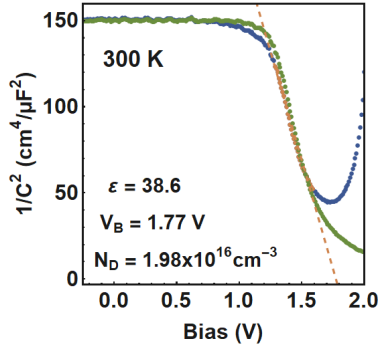


FIGURE 3.6. Typical capacitance versus voltage curve, measured at 300 K with a V_{AC} of 20 mV applied with a frequency of 10 kHz, here for the $\text{MAPbBr}_{1.5}\text{I}_{1.5}$ device. The forward and reverse scans are shown in green and blue, respectively.

difference. These high values are in line with previous works^{54,97}. The increase in capacitance values in the low-frequency regime when illuminating the devices has also been observed previously in TAS measurements of perovskite solar cells under light¹³⁸.

The phase angle part of the Bode plot is shown in Figure 3.8. At 10 kHz, the phase shift is close to -90° for all of the $\text{MAPb}(\text{Br}_x\text{I}_{1-x})_3$ devices, indicating that the devices are mostly capacitive (i.e. not resistive) at that frequency.

We further use the TAS measurement to determine the series resistance and parallel resistance of each of the devices, see Table I below. The methodology is the following: we fit the semi-circle of the Nyquist plot to an RC equivalent circuit model containing an RC circuit (with resistance and capacitance values R_p and C_p) in series with a resistor (with resistance R_s). The fit is performed in the region close to the TID measurement frequency of 10^4 Hz - here using a frequency range from 5×10^3 Hz to 5×10^4 Hz. This allows us to check that the series resistance is low enough for proper TID characterisation and it is the reason for the limited frequency range shown here. The resulting fits are shown in Figure 3.9. We observe that the very first datapoints seem to show a systematic error for most of the x -halide ratios (with the exception of $x = 0.5$), but we note that these datapoints are the points of highest frequency, where it is possible that the feature comes from another smaller semi-circle, representing an interfacial RC circuit in series to the main RC circuit modelled here¹³⁹.

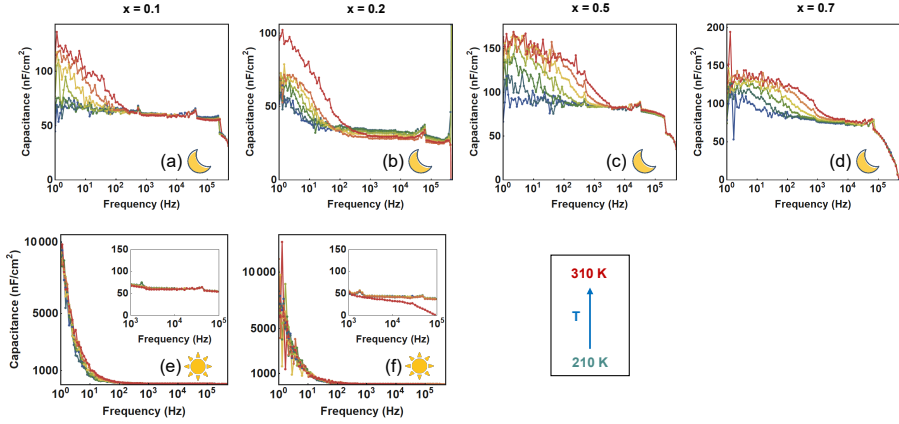


FIGURE 3.7. Impedance spectra of the $\text{MAPb}(\text{Br}_x\text{I}_{1-x})_3$ solar cells, measured from 1 Hz to 5×10^4 Hz with an AC voltage of 50 mV, in dark conditions, for (a) $x = 0.1$, (b) $x = 0.2$, (c) $x = 0.5$ and (d) $x = 0.7$; and in light conditions, for (e) $x = 0.1$, (f) $x = 0.2$. Insets in (e) and (f) allow for better visualization of the capacitance plateau at intermediate frequencies. The spectra shown here are taken at temperatures of 210 K, 230 K, 250 K, 270 K, 290 K and 310 K. Light conditions correspond to a 405 nm CW laser shining directly on the considered pixel, with a power density of 1.59 W cm^{-2} .

Light IV characterisation of the $\text{MAPb}(\text{Br}_x\text{I}_{1-x})_3$ solar cell devices is shown below in Figure 3.10. The devices show relatively low V_{OC} values of $(1.0 \pm 0.1) \text{ V}$. The FF and J_{SC} values are lower than literature values, due to the choice of transport layers. The device with $x = 0.7$ shows signs of phase separation, degrading the cell performance during the measurement timeframe itself. For TID characterisation of the devices with $x = 0.5$ and $x = 0.7$, we use fresh devices which have not been exposed to light, to avoid the light-induced phase separation process established for $x > 0.2$.

Some devices show shunting. The phase measurement in TAS shows that the measurement is mostly capacitive at the frequencies with which we measure TID (see Figure 3.8), ensuring that this shunting of the solar cells is not an issue for TID characterisation in this work.

We further note that for TID measurements, devices with non-optimal charge extraction could affect two parameters in the ion migration process, namely the mobile ion density, and the ion diffusion coefficient. However, the variation in these values is not expected to exceed one order of magnitude, and mobile ion densities and ion diffusion coefficients

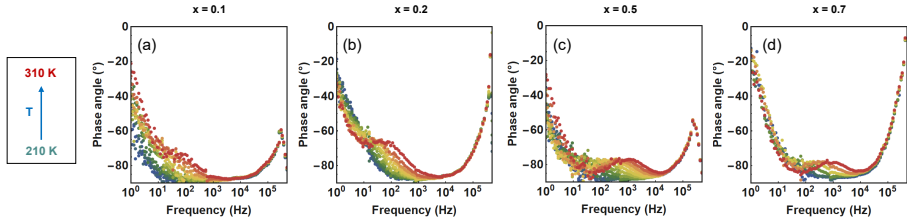


FIGURE 3.8. Phase shift in the Bode plot presentation of the impedance spectra of the $\text{MAPb}(\text{Br}_x\text{I}_{1-x})_3$ solar cells, measured from 1 Hz to 500 kHz with an AC voltage of 50 mV, in dark conditions, for (a) $x = 0.1$, (b) $x = 0.2$, (c) $x = 0.5$ and (d) $x = 0.7$.

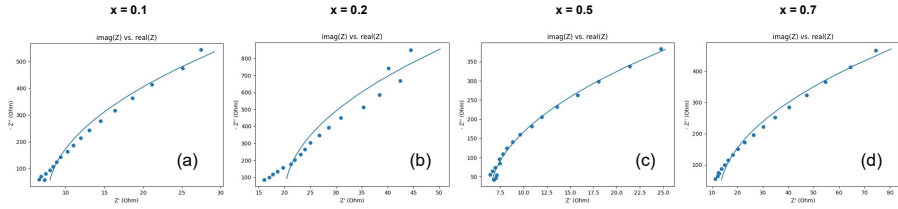


FIGURE 3.9. Fitting of the Nyquist semi-circle in the frequency range from 5 kHz to 50 kHz, at 300 K, for the $\text{MAPb}(\text{Br}_x\text{I}_{1-x})_3$ solar cells with (a) $x = 0.1$, (b) $x = 0.2$, (c) $x = 0.5$ and (d) $x = 0.7$.

are already presented with a high error bar in this manuscript. We thus conclude that the trends obtained with the present set of $\text{MAPb}(\text{Br}_x\text{I}_{1-x})_3$ devices would remain equivalent to that obtained with of a series of devices with optimized light IV characteristics.

We measure TID with different filling voltages (1 V, 1.25 V, 1.5 V). An example of the TID datasets with varying pulse voltages for the device with $x = 0.1$ is shown in Figure 3.11 below. There, we notice that the 1 V filling voltage is not sufficient for the TID measurement, as the built-in bias is on the upper end of that scale. We decide to base our analysis on the TID measurements taken with a voltage of 1.5 V, as it reliably offers the best signal when considering the range of device compositions measured for this study. Upon application of this 1.5 V bias, we assume that the depletion layer in the perovskite is fully collapsed. Note that we might see even larger signals for higher voltages, but the high injected current risks damage to the device. We account for this with the large error bar on the ion densities measured.

Composition	Series resistance ($\Omega \text{ cm}^2$)	Parallel resistance ($\Omega \text{ cm}^2$)	Capacitance (nF)
$x = 0.1$	7.72 ± 0.75	13400 ± 1300	58 ± 0.1
$x = 0.2$	20.06 ± 1.24	24400 ± 2700	36 ± 0.1
$x = 0.5$	6.41 ± 0.48	7760 ± 540	82 ± 0.2
$x = 0.7$	12.95 ± 0.84	3400 ± 100	65 ± 0.2

TABLE I. Values for sheet resistance, parallel resistance and capacitance of the $\text{MAPb}(\text{Br}_x\text{I}_{1-x})_3$ solar cells, as determined by modelling the high-frequency arc of the Nyquist plot.

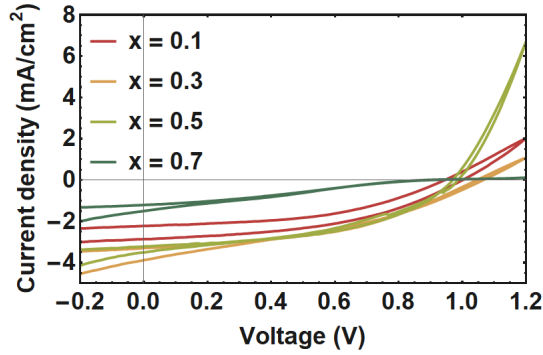


FIGURE 3.10. Light IV characterization of the $\text{MAPb}(\text{Br}_x\text{I}_{1-x})_3$ solar cell devices, measured with a scan speed of $10 \text{ mV} \cdot \text{s}^{-1}$, for $x = 0.1, 0.2, 0.5,$ and 0.7 .

To ensure that the TID measurements are non-destructive, once the TID measurement is finished, we repeat the impedance measurement, and verify that is unchanged with respect to the initial impedance measurement. To ensure measurement reproducibility, we either measure TID on multiple devices with the same composition or repeat the measurement multiple times on the same device.

Ion migration and hence phase segregation can happen under both the application of electrical or light bias. The voltage pulse in TID is a short perturbation after which we observe the drift of ions back to the steady-state position under zero bias. We assume that the properties of the ions (activation energy, density etc.) are independent of the applied bias for the mild electric fields applied here.

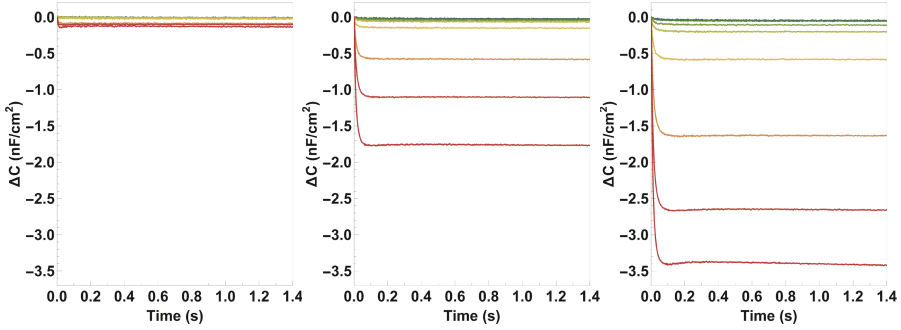


FIGURE 3.11. Relative difference in capacitance transients $\Delta C = C(t) - C_0$ of the MAPbBr_{0.3}I_{2.7} solar cell device, measured with an AC voltage of 20 mV, after applying a 2 s voltage pulse of (a) 1 V, (b) 1.25 V, and (c) 1.5 V, under dark conditions. The transients shown here are taken at temperatures of 210 K, 225 K, 240 K, 255 K, 270 K, 285 K, 300 K, 315 K and 330 K.

3.4.3 FITTING PROCEDURE

We use a global fit algorithm with the fit function shown in Equation 3.1. This fit function can be adapted to contain any number of exponential terms needed to resolve the full dataset of capacitance transients, where each of these exponential terms represents one specific ion migration process n , with its own ΔC_n , $p_{fit(n)}$ and $E_{a(n)}$.

The fitting procedure goes as follows: $C_\infty(T)$ is extracted from the measurements directly from the steady-state capacitance before we allow the algorithm to find the best value for $\Delta C(T)$ at each temperature and the best global values for p_{fit} and E_a . We thus directly obtain the value of the activation energy E_a . The fitted parameter p_{fit} is then used to determine the diffusion coefficient, using Equation 3.2:

$$D_0 = \frac{k_B \epsilon \epsilon_0}{q^2 N_D p_{fit}} \quad (3.2)$$

We further use Equation 3.3 below to obtain the temperature-dependent ion diffusion coefficient, $D(T)$.

$$D(T) = D_0 \exp\left(\frac{-E_a}{k_B T}\right) \quad (3.3)$$

In Figure 3.3b and e we present the diffusion coefficients calculated at room temperature, $D(300 \text{ K})$, for the MAPb(Br_xI_{1-x})₃ solar cells in dark and in light, respectively.

The fitted $\Delta C(T)$ parameter is used to determine the ion concentration N_{ion} , using Equation 3.4 below.

$$N_{ion}(T) = 2 N_D \frac{\Delta C(T)}{C_{\infty}(T)} \quad (3.4)$$

In Figure 3.3c,f, we present N_{ion} as a function of N_D and show the maximal value for the density of mobile ions, $N_{ion}(max)$.

On top of the set of assumptions detailed in Chapter 1 of this thesis, we note that we assume that the background doping does not change under illumination.

Values for the parameters in Figure 3.3 are obtained from multiple repetition of the fit procedure on the same TID transient, averaging the fit parameters giving the lowest chi-square values and taking their standard deviation as an estimate for the error.

We additionally note that in this Chapter, we attribute the ion migration to vacancy-mediated migration, as it has been suggested to be the most likely candidate process at play^{33,40}, and it is energetically favoured compared to interstitial-mediated ion migration³². Finally, we note that TID does not resolve the specific ion migration mechanism at play but is a powerful technique for quantifying the key ion migration characteristics mentioned above - E_a , D_{ion} , N_{ion} .

4 THE IMPACT OF GRAIN SIZE

ACTIVATION ENERGY AND MIGRATION PATHWAYS IN MAPbBr₃ SOLAR CELLS

Ion migration in perovskite layers can significantly reduce the long-term stability of the devices. While perovskite composition engineering has proven an interesting tool to mitigate ion migration, many optoelectronic devices require a specific bandgap and thus require a specific perovskite composition. Here, we look at the effect of grain size to mitigate ion migration. We find that in MAPbBr₃ solar cells prepared with grain sizes varying from 2 to 11 μm , the activation energy for bromide ion migration increases from 0.17 to 0.28 eV. Moreover, we observe the appearance of a second bromide ion migration pathway for the devices with largest grain size, which we attribute to ion migration mediated by the bulk of the perovskite, as opposed to ion migration mediated by the grain boundaries. Together, these results suggest the beneficial nature of grain engineering for reduction of ion migration in perovskite solar cells.

This chapter is based on the following publication¹²⁴:
Lucie McGovern, Isabel Koschany, Gianluca Grimaldi, Loreta A. Muscarella and Bruno Ehrler, "Grain Size Influences Activation Energy and Migration Pathways in MAPbBr₃ Perovskite Solar Cells", *Journal of Physical Chemistry Letters*, vol. 12, pp. 2423–2428, 2021.

4.1 INTRODUCTION

Over the recent decade, the advancement of metal halide perovskite solar cells has shown remarkable results, with power conversion efficiencies (PCEs) reaching as high as 25.5 % for single junctions and 29.2 % for perovskite/silicon tandems¹⁰. In terms of efficiency, this class of material has thus proven effective in solar cell devices. This high performance is, however, somewhat mitigated by the stability issue this technology currently exhibits, where a decrease of the PCE of devices over time is commonly observed. This stability loss can be linked to two types of degradation processes, caused by either intrinsic factors or extrinsic factors. Extrinsic factors include moisture, oxygen exposure, and heat, which can all rapidly degrade the PCE of devices. Though very detrimental to cell performance, these degradation-inducing factors can mostly be prevented, noticeably through passivation or encapsulation schemes of the perovskite layer^{140–143}. Of more problematic nature are the intrinsic factors of degradation. Indeed, contrary to most solar cell technologies, perovskite crystals are not formed by covalent bonds only, but instead exhibit dual covalent and ionic nature^{12,144}, bearing in mind that ionic bonds are weaker. A number of defects can thus readily occur in the perovskite lattice, including ion vacancies and ion interstitials³³. Within the solar cell stack, these charged ions can drift toward the electrode of reverse polarity, in a process called ion migration. Under operation, this migration can further change the charge and elemental distribution throughout the perovskite layer and is known to affect the long-term stability of devices^{108,145,146}.

To achieve long-term stability in metal halide perovskite solar cells, it is thus necessary to understand the intrinsic degradation process that is ion migration, to find suitable ways of mitigating and eventually suppressing this feature altogether.

In devices, the ions migrate from their initial defect position in the lattice toward the perovskite interface with the transport layer and accumulate at that interface⁸⁹. However, there is still ongoing debate on how this migration proceeds in the film, namely, whether the process is mediated by the grain boundaries or rather by the bulk of the polycrystalline perovskite films. Some studies report an increased ion migration at grain boundaries, while others report the opposite effect: Studies reporting an enhancement of ion migration at grain boundaries include a range of atomic force microscopy techniques (c-AFM, KPFM, and BE-KPFM) showing the contact potential difference or the hysteresis per-

centage mapped locally^{48,147,148}; imaging techniques (SEM) visualizing the deterioration of the grain boundaries¹⁴⁸; elemental techniques (EDX) measuring the dynamic of the lead-to-halide ratio¹⁴⁸; and conductivity measurements comparing films of various grain size to extract an activation energy for the migration process⁴⁹. Studies reporting a reduction of ion migration at grain boundaries include PL techniques (PL microscopy and PLQY) tracking the ionic defect distribution rate¹⁴⁹ and intensity-modulated photocurrent spectroscopy measurements (IMPS) comparing the ionic current responses in thin and thick cells¹⁵⁰.

With this study, we thus aim to answer the following question: is increasing the grain size an effective way to mitigate ion migration? We choose MAPbBr₃, a well-characterized perovskite in terms of ion migration^{56,77,151}. The major advantage of using this perovskite material is the possibility to synthesize films of varying grain size, without altering key physical or chemical properties of the film. To characterize and quantify ion migration, we use transient ion drift (TID), a capacitance-based technique which allows for determination of the nature of the mobile ions and quantification of their migration activation energy, diffusion coefficient, and number density^{51,56,76}. The combination of this measurement technique together with a perovskite recipe that allows for grain size variation without any modification of the perovskite composition allows us to determine the influence of grain boundaries on ion migration in perovskite solar cells.

4.2 RESULTS AND DISCUSSION

4.2.1 VARYING THE GRAIN SIZE IN MAPbBr₃ SOLAR CELL DEVICES

To measure the influence of grain size on ion migration, we prepare solar cell devices with an active layer of polycrystalline MAPbBr₃ perovskite, of which we modulate the grain size. The recipe for MAPbBr₃ perovskite is adapted from reference [152]. Its advantage is the possibility of varying the perovskite grain size without modifying any key chemical parameters: only the spin-coating time is varied, while all other parameters, including precursor content, solvent, antisolvent, and annealing conditions, remain unchanged. Optical microscopy (OM) images of the films are shown in Figure 4.1a,b, where we observe that the grain size is correlated to the spinning time of the solution, with short spinning times leading to larger grains. After a spinning duration of 5 s, the grains in the final film

measure an average size of $(11.3 \pm 1.7) \mu\text{m}$ (Figure 4.1a), while 60 s of spinning leads to an average size of $(1.7 \pm 0.2) \mu\text{m}$ (Figure 4.1b). Grain size attribution by microscopy techniques such as OM and SEM might be misleading^{152,153}; we thus confirm our initial OM characterization with electron backscatter diffraction (EBSD). The EBSD images show an overlay of the image quality (brightness, IQ) with the inverse pole figure (color, IPF) along the z -axis (normal to the substrate, Figure 4.1c,d) and x -axis (parallel to the substrate, Figure 4.1e,f). The IPF relative to the x -axis shows a distribution of orientations along the $[101]$ and the $[111]$ directions, indicative of polycrystallinity. The grains and grain boundaries detected by EBSD correspond to those observed by OM, thereby confirming the grain size characterization by OM. We conclude that this recipe, when used at spinning times between 5 and 60 s, allows for about 1 order of magnitude in grain size variation.

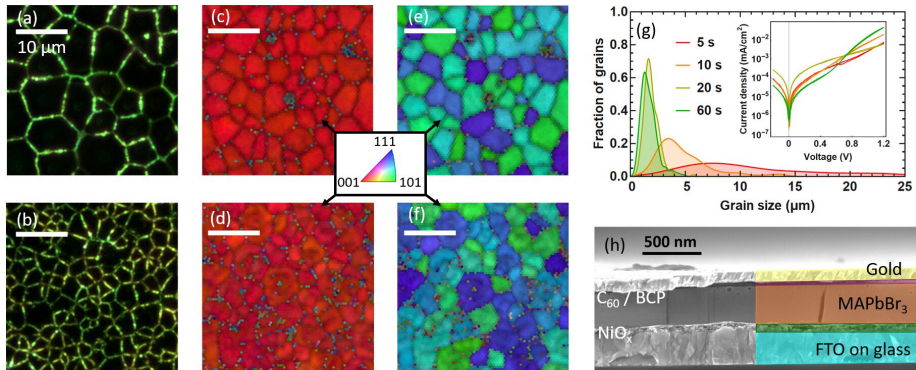


FIGURE 4.1. Top-view OM image of a MAPbBr_3 perovskite film spin coated for (a) 5 s and (b) 60 s. The z orthogonal-direction top-view EBSD of the MAPbBr_3 films spin coated for (c) 5 s and (d) 60 s. The x in-plane-direction top-view EBSD of the MAPbBr_3 films spin coated for (e) 5 s and (f) 60 s. The inverse pole figure legend in the EBSD images shows the crystallization plane as a function of color. (g) Histogram of the average grain size as a function of spin coating time, with inset of the dark IV curves of the devices. (h) Cross-section SEM image showing the device layers: FTO, NiO_x , MAPbBr_3 , C_{60} , BCP, and gold. The device has a planar p-i-n architecture. The white scale bars presented from (a) to (f) all represent a $10 \mu\text{m}$ length.

The polydispersity in grain size is presented in the histogram in Figure 4.1g. The small grain regime is characterized by relatively sharp peaks of standard deviation $\sim 0.2 \mu\text{m}$, whereas the size distribution is more pronounced in the big grain regime, with standard deviations of 0.6 and

1.7 μm respectively for the 5 and 11 μm samples.

Each of these active perovskite layers of MAPbBr_3 is incorporated into a p-i-n solar cell architecture as shown in Figure 4.1h. Representative cross-section SEM pictures show uniform stacking of these successive layers. The thick perovskite film exhibits vertical grain boundaries—the same as those observed in top-view OM images. The bottom electrode is a FTO layer, covered by a hole transport layer of NiO_x on top of which the MAPbBr_3 perovskite is spin coated, finally the electron transport layer consists of C_{60} and BCP, and a gold electrode on top completes the device. The extraction layers are chosen specifically because they exhibit no direct ion migration, even though they may reduce the overall PCE of the devices. Dark IV curves of the devices (see the inset of Figure 4.1g) confirm good diode characteristics, a prerequisite for the TID measurements to study ion migration.

The solar cell performance of the devices is shown in Figure 4.2a, where the IV characteristics from the best cells are presented. There, it is already apparent that the FF and J_{SC} are the values most affected by grain size. For a fairer comparison, the average values taken over multiple pixels from multiple devices are shown in Table I. There, we observe that the V_{OC} does not change as a function of grain size, which is an indication that the amount of non-radiative recombination is similar in all devices. The overall PCE of the devices is constant through the series of varying grain size films: from 1 % to 1.3 %. The devices show reasonable efficiency for the simplistic solar cell architecture considered here, and are in line with other works using similar HTL and ETL⁷⁹. As mentioned in above, we choose the extraction layers NiO_x , C_{60} and BCP mainly because they are not themselves affected by ion migration, contrary to other commonly used extraction layers such as Li-TFSI doped Spiro-O-MeTAD^{45,154}. We note that the low efficiency does not affect the TID measurement as the devices are measured in the dark where the measurement mainly requires a low dark current to avoid electrical charge flowing through the device affecting the depletion layer width. All in all, two parameters are thus affected by grain size, J_{SC} and FF, in an opposing manner, where the increase of one is concomitant to the decrease of the other – thereby maintaining a constant PCE. The relatively low fill factor values are partly due to a low shunt resistance. As mentioned earlier, this can be modulated by further device engineering and is therefore not the focus of the present study. The EQE curves of the devices are shown in Figure 4.2b. These match well with the corresponding IV curves of Figure 4.2a, with slightly lower J_{SC} values. The highest EQE point

	5 s	10 s	20 s	60 s
J_{SC} (mA/cm ²)	4.1 ± 0.2	3.2 ± 0.1	3.6 ± 0.2	4.3 ± 0.3
V_{OC} (V)	0.88 ± 0.03	0.84 ± 0.02	0.87 ± 0.02	0.82 ± 0.02
FF (%)	27.4 ± 2.7	47.0 ± 1.5	39.2 ± 1.7	36.0 ± 2.2
PCE (%)	1.0 ± 0.1	1.3 ± 0.1	1.2 ± 0.1	1.3 ± 0.1

TABLE I. Average IV solar cell characteristics of the devices made with a polycrystalline MAPbBr₃ film prepared with a spin coating process of 5, 10, 20 or 60 seconds.

reaches almost 60%, for the sample spin coated for 60 seconds (i.e. with smallest grain size). The overall shape of the EQE feature follows that of typical MAPbBr₃ absorption, with the characteristic excitonic peak at 525 nm, and the bandgap at 540 nm, further confirming the successful preparation of MAPbBr₃ devices.

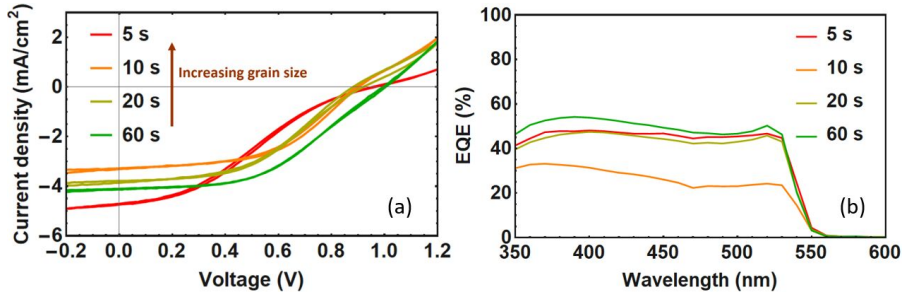


FIGURE 4.2. (a) Light IV curves of the best pixel for each of the solar cell device made with a photoactive layer of polycrystalline MAPbBr₃, spin coated for 5, 10, 20 or 60 seconds. (b) EQE curves of the best pixels for each of these devices.

4.2.2 TRANSIENT ION DRIFT CHARACTERISATION

TID is an electric spectroscopy technique for ion migration measurements used in perovskite solar cells^{56,76}. The measurement is based on two steps: first, the application of a filling voltage which will redistribute the ions within a device and, second, the release of this voltage pulse, which will lead to the ions drifting back to their initial position. We record the capacitance signal during this second step by applying a small

alternating voltage V_{AC} , which thus provides a direct measurement of the ion migration process.

For TID characterization, the first step is the selection of a relevant frequency at which to apply the alternating voltage—for this purpose we measure the impedance spectra of all devices. The two extreme situations are presented in Figure 4.3, where the impedance spectra of the devices with smallest and largest grain size are shown respectively in panels a and b. Both impedance spectra look very much alike and resemble earlier measurements of MAPbBr_3 ⁵⁶. They can be decomposed into a low-frequency regime which is temperature-dependent and dominated by ion accumulation¹⁵⁵ and a high-frequency regime which is characterized by a decrease of the capacitance signal due to the series resistance. In between these two regimes lies an intermediate plateau regime, where the capacitance is determined by the depletion capacitance - this is suitable for TID measurements. We thus select the frequency of 10^4 Hz for the small alternating voltage V_{AC} in the intermediate impedance regime.

Figures 4.3c and 4.3d show the TID capacitance traces after applying a filling voltage of 1 V for 2 s to the devices with smallest and largest grain size, respectively. Interestingly, both TID traces show a negative slope in the whole temperature range considered, independent of the grain size. This is further confirmed in the TID traces taken after applying filling voltages of 0.75 or 1.1 V (see Section 4.4.2). In TID of p-type semiconductors, a negative transient is attributed to anion migration. In the MAPbBr_3 crystal structure, the only anion species is the bromide ion. The main ion migration process at play in the whole device range is thus bromide migration. This was previously observed for MAPbBr_3 in our work comparing MAPbI_3 and MAPbBr_3 ⁵⁶ and is further confirmed here.

4.2.3 ACTIVATION ENERGY INCREASE, CONSTANT MOBILE ION DENSITY AND DIFFUSION COEFFICIENTS

In this study, we use TID to quantify the ion migration activation energy E_a , the density of mobile ions N_{ion} , and the diffusion coefficient D for each grain size. The fitting procedure is described in the Supporting Information, in Section 4.4.2, where the insets in Figure 4.3c,d show the good correspondence of the fits with the data.

In the small grain regime (1-3 μm), the data can be accurately fitted with one exponential contribution, suggesting a single ion migration process. As the average grain size grows ($> 5 \mu\text{m}$), the fit needs an ad-

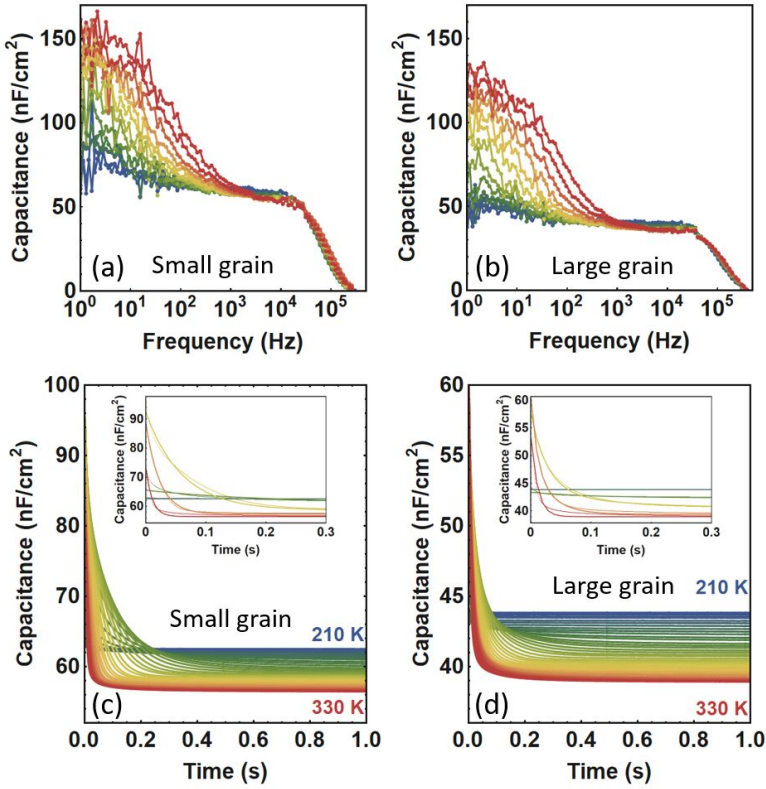


FIGURE 4.3. Impedance spectra of the devices with (a) $1.7\ \mu\text{m}$ and (b) $11.3\ \mu\text{m}$ grain size MAPbBr₃ perovskite films, measured by using an AC voltage of 10 mV. TID traces after applying a voltage pulse of 1 V for 2 s to the devices with (c) $1.7\ \mu\text{m}$ and (d) $11.3\ \mu\text{m}$ grain size perovskite films, between 210 and 330 K in steps of 3 K. The insets in (c) and (d) show the fit to the data for five intermediate temperatures: 210, 240, 270, 300, and 330 K.

ditional exponential contribution to accurately represent the data (see Figure 4.4a). TID cannot directly point to the microscopic migration pathway; however, the presence of two separate peaks (with distinct E_a , N_{ion} , and D) is a strong indication for the combination of two bromide migration processes in the perovskite film, where, for example, in addition to the grain boundary mediated pathway most often described, a bulk pathway would appear for films with larger grains. We expand on this idea below and for now refer to these migration pathways as peak A and peak B (respectively in purple and in orange in Figure 4.4).

The density of mobile ions is on the order of $5 \times 10^{15}\ \text{cm}^{-3}$ to

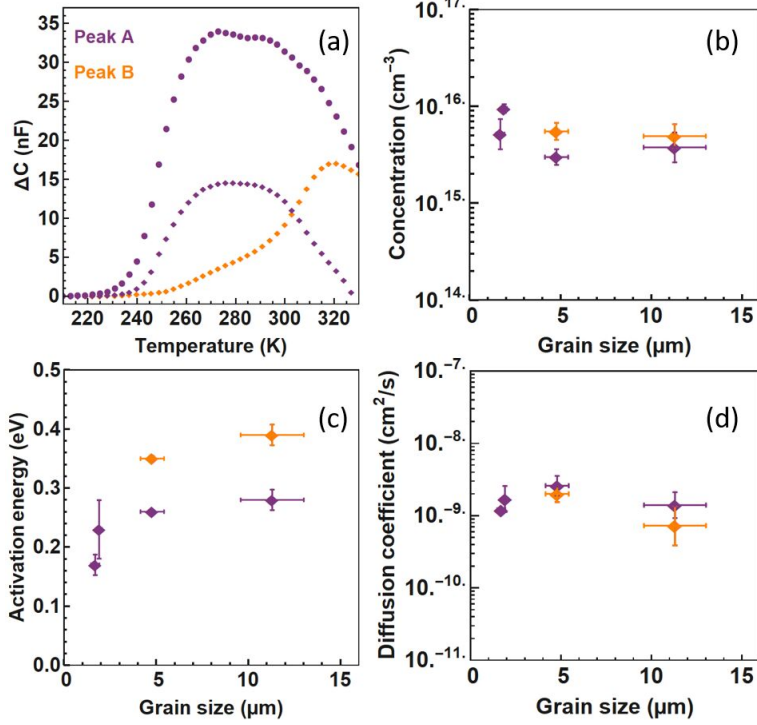


FIGURE 4.4. Effect of grain size on ion migration parameters: (a) Typical ΔC peak(s) found after fitting the TID traces for samples with 1.7 μm grain size (circle) and with 11 μm grain size (diamond). Peaks A and B are shown in purple and orange, respectively. (b) Concentration of mobile ions, (c) activation energy, and (d) diffusion coefficient, extracted by using Equations in Section 4.4.2.

$1 \times 10^{16} \text{ cm}^{-3}$, as shown in Figure 4.4b. We note that this low density of mobile ions is in agreement with the assumption of ions incompletely screening the built-in voltage in perovskites⁸⁸. The total density of mobile species from peaks A and B is rather constant with grain size: 5.2×10^{15} , 9.5×10^{15} , 8.5×10^{15} , and $8.7 \times 10^{15} \text{ cm}^{-3}$ for the samples with 1.7, 1.9, 4.8, and 11.3 μm grain size, respectively. This is consistent with a model where the ion defect formation energy is independent of the grain size. This trend suggests that ion vacancies form in the bulk of the perovskite or at the interface with the transport layers.

We now look at the evolution of E_a as a function of grain size, as shown in Figure 4.4c. The activation energy describes the energy it

takes for an ion to move to the neighboring unit cell. E_a of peak A first strongly increases with grain size, before reaching a saturation regime for grains larger than $5\ \mu\text{m}$. For peak B, which is only present for the larger grains, we notice a higher activation energy than peak A and a slight increase with grain size from (0.35 ± 0.01) to (0.39 ± 0.02) eV for films of average grain size 4.8 to $11.3\ \mu\text{m}$. The general trend is thus an increase in the activation energy with grain size, indicative of a stronger barrier to the migration process for larger grains. This increase is first rapid and then reaches a saturation regime for grains between 5 and $11\ \mu\text{m}$. We note that the defect formation energy (DFE) model developed by Meggiolaro *et al.*³⁶ shows a similar evolution of the activation energy with grain size but that a difference of DFE would lead to a change in the density of mobile ions in grain interiors compared to grain boundaries, an explanation which is in contradiction with our observation.

The diffusion coefficient as a function of grain size is presented in Figure 4.4d. The values are on the order of $10^{-9}\ \text{cm}^2\text{s}^{-1}$, similar to previous observations for halide migration⁵⁶. These remain relatively constant with grain size, the lowest value being observed for peak B of the sample with largest grains, with $(7.3 \pm 4.6) \times 10^{-10}\ \text{cm}^2\ \text{S}^{-1}$ and the highest value being observed for peak A of the sample with $4.8\ \mu\text{m}$ grains, with $(2.6 \pm 0.8) \times 10^{-10}\ \text{cm}^2\ \text{S}^{-1}$. Within the error this shows a relatively constant diffusion coefficient as compared to the clear increase in activation energy with grain size. Additional considerations regarding the diffusion coefficient and activation energy trends are added in Section 4.4.2.

4.2.4 GEOMETRICAL MODELLING

We now combine all the previous observations into a possible model. We find the same total number of mobile ions (from peaks A and B combined) independent of the grain size, which means that these mobile ions do not arise from the grain boundary. On top of that the activation energy of peak A increases with grain size. Here it cannot be explained by a reduced number of mobile ions in grain interiors compared to grain boundaries: this observation instead suggests that the mobile bromide ions experience a migration pathway with higher activation energy in the bulk of the grain relative to grain boundaries. We speculate that ions migrate first from their original location in the grain interior to the grain boundary and then through a grain boundary channel toward the interface. The larger the grain size, the fewer grain boundaries are present,

and the further away from a grain boundary an average ion will be positioned. The increase in activation energy of peak A with grain size is thus a representation of the longer average traveling distance to the grain boundary. The migration through the grain boundary channel is thus faster than the migration within the grain, in agreement with various experimental studies showing faster ion migration at the grain boundaries^{48,49,147,148}. For larger grains we find a new ion migration pathway labeled peak B. With larger grains, it is possible that some of the ions migrating within the grain become so far away from any grain boundary that an additional migration pattern arises, where the ions migrate directly from the grain interior to the interface. The implication there is that the migration from grain interior to interface is slower than the migration from grain interior to grain boundary but still takes place when the interface becomes closer than a grain boundary region. This model is also consistent with a relatively constant activation energy and diffusion coefficient for peak B. The illustrative scheme of this model is presented in Figure 4.5a,b. We thus assign peak A as grain-boundary-mediated bromide migration and peak B as grain-interior-mediated bromide migration.

The observed trend can be approximately captured by a geometrical model for the motion of ions, in which, for simplicity, we consider the motion of ions along the fastest path to the electrode (see Section 4.4.3). Figure 4.5c shows the effective activation energy as a function of grain size, obtained by computing the fraction of the path occurring inside the grain and optimizing the value of the activation energies for bulk and grain boundaries diffusion. We obtain activation energies of 0.18 and 0.50 eV for ion diffusion along the grain boundaries and in the bulk. Despite the approximate nature of the model, leading to a large shift in the onset of the activation energy change as a function of grain size, it captures the experimentally observed increase in activation energy for larger grains.

We note that PL microscopy, PLQY, and IMPS studies^{149,150} suggest that ions migrate from the inside of a grain to a grain boundary and then become trapped at the grain boundary. These works all have in common that they study ion migration along the in-plane direction by diffusion. Here, the ions may be initially trapped at the grain boundary, but they are then allowed to drift through the grain boundary channel in the normal direction, leading them to the interface of reverse polarity.

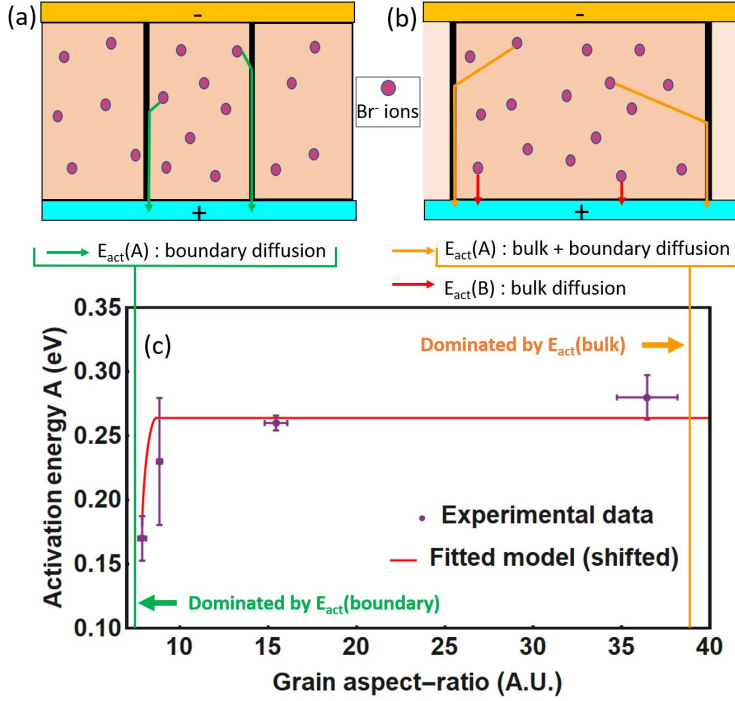


FIGURE 4.5. Model of ion migration in grains with different lateral size. Schematic of the proposed ion migration, where (a) in small grain sizes most ions first migrate to the grain boundary before they migrate to the interface via the boundary and (b) for larger grain sizes a second pathway appears where the ions migrate to the interface directly. (c) Fit to the experimental data of a geometrical model for the activation energy of ion diffusion (Section 4.4.4).

4.2.5 TRAP STATES

The grain size of a perovskite film can also affect the electronic trap states. By applying a short voltage pulse of 20 ms instead of 2 s to measure only the contribution of trap states to the capacitance signal, we see changes in the trap state population and energy. The resulting trap depths, trap densities and trap attempt-to-escape frequencies of the MAPbBr₃ cells with smallest and largest grain size are presented in Table II.

We find one dominant electronic trap, which is shallower for the largest grain size sample ($E_T = 192$ meV) compared to the smallest grain size ($E_T = 300$ meV). This on its own could suggest an increase in the recombination rate for cells with smallest grain size. The density of traps

	5 s (largest grains)	60 s (smallest grains)
E_{trap} (eV)	0.192 ± 0.020	0.300 ± 0.002
N_{trap} (cm^{-3})	$(1.55 \pm 0.64) \times 10^{15}$	$(7.25 \pm 0.18) \times 10^{15}$
$A(300 \text{ K})$ (s^{-1})	$(4.58 \pm 0.11) \times 10^5$	$(7.86 \pm 0.74) \times 10^5$

TABLE II. Average trap depth, density of traps and attempt frequency of the devices made with a polycrystalline MAPbBr₃ film prepared with a spin coating process of 5 or 60 seconds (respectively with largest and smallest grain size).

is also highest for the cells with smallest grains, i.e. the cells with most grain boundaries. The factor of increase is a little over 4, close to the 3.8 difference in density of grain boundaries when going from cells with 1.7 μm grains to cells with 11.3 μm grains - this strongly suggests that the traps are located at the grain boundaries of the perovskite film. We thus find that the density of trap states scales with the number of grain boundaries present, suggesting that the grain boundaries play a major role in trap state formation. This initial finding warrants further investigation.

4.3 CONCLUSION

We studied bromide ion migration in MAPbBr₃ perovskite solar cells where we find that the grain size mainly affects the activation energy, while the density of mobile ions and their diffusion coefficient remain relatively constant with grain size. This is a first indication that crystallinity is indeed an effective tool to mitigate ion migration. The quantification of the density of mobile ions and diffusion coefficient are further useful in understanding how the migration pathway is affected by grain size. Ion migration is reduced in cells with larger grains not due to a lower density of mobile ions, but rather due to a higher energy of the transition state for the hopping process in the grain interior compared to that transition state at the grain boundary. Together, our results suggest that for smaller grains there is only one migration process mediated by the grain boundaries and that for larger grains a process mediated by the grain bulk becomes significant. Crystallinity is thus an effective tool to reduce ion migration, proving itself as an interesting strategy for long-term stability of devices.

4.4 APPENDIX

4.4.1 DEVICE FABRICATION AND CHARACTERISATION

The solar cell fabrication closely follows the recipes established in reference [56], with the notable exception of the MAPbBr₃ perovskite layer preparation, which we detail below.

The precursor for the MAPbBr₃ layer is fabricated from two solutions dissolved together in dimethyl sulfoxide (DMSO). First, a solution of 5.5 M methylamine hydro bromide (MABr, TCI) is made by dissolving the powder in DMSO (Sigma-Aldrich). To ensure a complete dissolution, the precursor is stirred and heated on a hot plate to 50-60 °C. The second precursor is a 1.8 M lead(II) acetate trihydrate (PbOAc) solution (Sigma-Aldrich). To prepare this solution, the PbOAc powder is dissolved in DMSO and stirred and heated to 50-60 °C overnight. Both precursor solutions are stirred and heated up to 65 °C until a clear dense solution is formed. This final MAPbBr₃ precursor solution has a molarity of 3.05 M. For the spin coating step, 200 μ L are used per sample, with a spin coating speed of 7500 rpm. To vary the grain size in the perovskite film, we vary the spin coating times: 5 s, 10 s, 20 s and 60 s. The samples are annealed for 1 h on the hot plate at 70 °C. During this annealing step, the samples quickly show a yellow-orange color, characteristic for MAPbBr₃. All of the above steps are carried inside a glovebox in a nitrogen atmosphere, with an O₂ level below 1 ppm. For proper investigation both of the perovskite layer and of the full device, cells are either prepared until the perovskite layer (optical microscopy and EBSD imaging) or as the whole device (all electrical measurements and SEM cross-section imaging).

Optical microscopy images are taken using an Imager.A2m Zeiss microscope with an AxioCam ICc 5 camera in the dark field mode, with magnification objectives of 20 \times , 50 \times or 100 \times . Many images of the various samples are collected and the evaluation of each grain size is done through software evaluation using the program ImageJ. Specifically, to characterize the polydispersity in grain size, we take OM pictures at multiple spots and of multiple films spin coated for the same duration. For each of these images we measure the average grain size. Performed over multiple images, we obtain statistics on the grain size distribution for about 60 to 80 grains per spin coating condition. We note that the word “grain size” used in this chapter systematically refers to grain diameter.

The SEM images are taken with a FEI Verios 460 scanning electron microscope in the secondary electron mode. The sample is cleaved in the

center to obtain the cross-section image. The acceleration voltage used is 10 kV and the working distance is 4 mm. EBSD images of MAPbBr₃ on NiO_x are collected by using a direct electron detector based on the Timepix sensor from Amsterdam Scientific Instruments (ASI). The best parameters for the scans are found to be 10 keV for the voltage, 100 pA for the current, 50 ms for the exposure time, and between 10 and 12 mm for the working distances. The step size is chosen depending on the cluster size shown by the specific sample. EBSD data are collected using EDAX OIM software, and a Python script is used for image processing. The resulting Kikuchi patterns are indexed as cubic symmetry, using 1-3° as the degree of tolerance. Characterizing the MAPbBr₃ layer of the different spinning durations, we notice, on top of the grain size evolution, an evolution in the thickness of the perovskite layer. Samples prepared after 5 or 10 seconds spinning duration have a thickness of (310 ± 10) nm, while the samples prepared after 20 or 60 seconds spinning duration have a thickness of (215 ± 10) nm. This thickness difference is incorporated into the different Equations presented in Section 4.4.2 below.

4.4.2 CAPACITANCE MEASUREMENTS

GENERAL CONSIDERATIONS For TID measurements the sample is loaded into a Janis VPF-100 liquid nitrogen cryostat inside a nitrogen-filled glovebox. Impedance spectroscopy, capacitance-voltage, transient ion-drift and deep level transient spectroscopy measurements are performed at a pressure below 2×10^{-6} mbar, in the dark, using a commercially available DLTS system from Semetrol. To ensure thermal equilibrium, the temperature of the sample is held constant for at least 30 minutes before impedance spectroscopy and capacitance-voltage measurements. Capacitance transient measurements were performed from 210 K to 330 K in steps of 3 K with a temperature accuracy of 0.2 K. The sample is held at 330 K for 30 minutes before starting the transient ion-drift and deep level transient spectroscopy measurements.

MOTT-SCHOTTKY ANALYSIS TID is a technique which makes use of a voltage bias to redistribute ions within a device. The voltage applied should thus be close to the built-in voltage of the cell. We determine this value by Mott-Schottky analysis¹⁵⁵ as shown in Figure 4.6. We obtain values of 1.09 V, 0.98 V, 1.02 V and 1.24 V for typical devices with grain size 1.7 μm, 1.9 μm, 4.8 μm and 11.3 μm, respectively. In the subsequent TID measurements, we thus apply voltage biases of 1 V (see Figure 4.3) and 1.1 V (see Figure 4.7). We further measure the devices with a lower

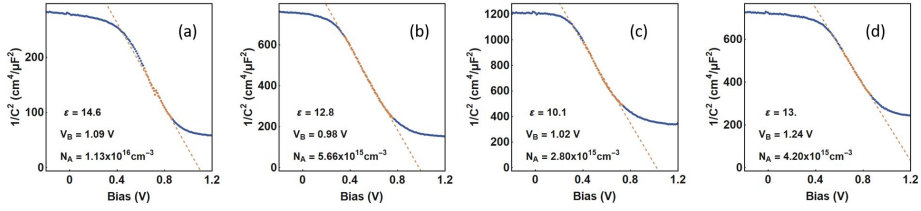


FIGURE 4.6. Mott-Schottky plots of the devices with MAPbBr₃ perovskite films of (a) 1.7 μm grain size; (b) 1.9 μm grain size; (c) 4.8 μm grain size; (d) 11.3 μm grain size.

applied voltage of 0.75 V in order to test the measurement response and to check if ion migration is already visible for smaller built-in fields. We note that our Mott-Schottky measurement is taken in reverse mode, and that the doping density values are found to be above the minimal threshold for correct Mott-Schottky evaluation⁹⁸.

STEADY-STATE CAPACITANCE The steady-state capacitance (determined either by Thermal Admittance Spectroscopy (TAS) or by TID, taking the values at longer times) is found to be stable with temperature (see Figure 4.7 below). We attribute this effect to the choice of contact layers, NiO_x and C₆₀. Indeed, if we chose other contact layers, the geometric capacitance would become temperature dependent, presumably because of the formation of a dipole layer at that interface¹⁵⁶.

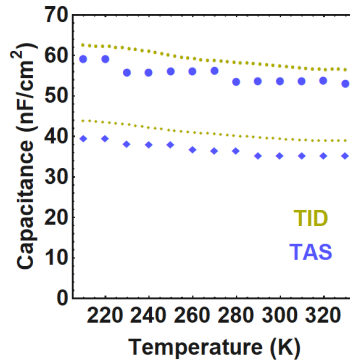


FIGURE 4.7. Steady-state capacitance values obtained by thermal admittance spectroscopy measurements at 10 kHz - in green - and from TID measurements, taking the capacitance value at longer times - in blue - for the cells with small and large grain size (represented by circle and diamond respectively).

TID MEASUREMENTS WITH VARYING FILLING VOLTAGES In Figure 4.8 a-h we show the TID traces taken at different filling voltages of 0.75 V and 1.1 V, for the samples from the smallest (Figure 4.7 a and e) to the largest grain size (Figure 4.7 d and h). The first observation is the presence of a similar trend in all cases, that is that the capacitance decreases with time. This pattern is conserved for the samples with small and large grain size, and for all filling voltages. The ion migration process at play must therefore remain bromide migration.

One parameter is, however, affected by the voltage pulse: the height of the transient, with higher voltages leading to a more pronounced transient. This indicates a difference in the density of mobile ions measured after applying the different filling voltages: more bromide mobile ions have been displaced when applying a voltage pulse of 1 V or 1.1 V, rather than a lower voltage pulse of 0.75 V. Some but not all of the mobile bromide ions in our devices have thus already been displaced by a voltage pulse of 0.75 V. This trend is consistent with a built-in voltage of about 1 V, meaning that the device is still partially depleted at 0.75 V.

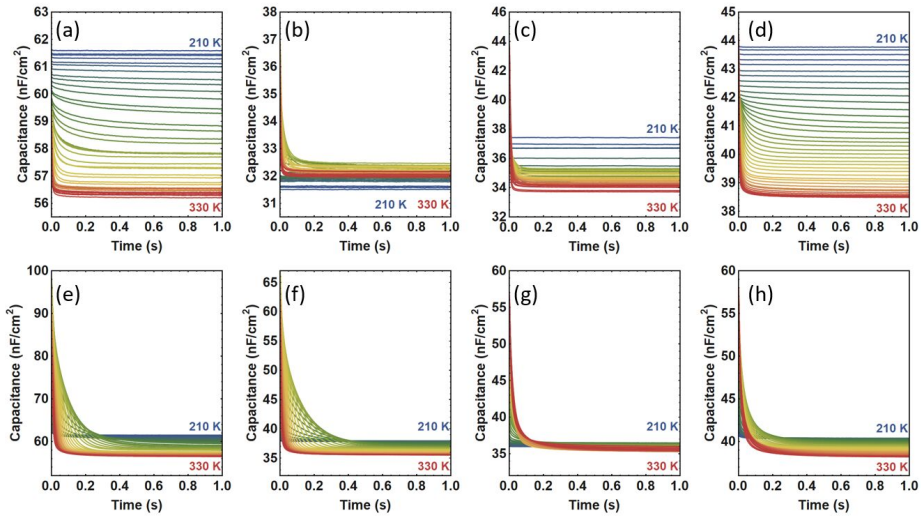


FIGURE 4.8. TID traces measured after applying filling voltage of 0.75 V for 2 seconds to the devices with MAPbBr₃ perovskite films of (a) 1.7 μm grain size; (b) 1.9 μm grain size; (c) 4.8 μm grain size; (d) 11.3 μm grain size; TID traces measured after applying a filling voltage of 1.1 V for 2 seconds to the devices with MAPbBr₃ perovskite films of (e) 1.7 μm grain size; (f) 1.9 μm grain size; (g) 4.8 μm grain size; (h) 11.3 μm grain size.

FITTING PROCEDURE AND EXTRACTED TRENDS To quantify bromide migration, we use a global fit algorithm. This global fit algorithm is fully described in Sections 3.2.3 and 3.4.3 of Chapter 3. The assumptions of the model are detailed in Chapter 1.

To apply the conversions from p_{fit} and $\Delta C(T)$ to $D(T)$ and $N_{ion}(T)$, we need values for the perovskite permittivity ϵ and for the doping density N_D of the devices. These are determined through Mott-Schottky analysis, as shown in Figure 4.6. For typical devices made with small (large) grain size, the perovskite permittivity is of 14.6 (13), while the doping density reaches $1.13 \times 10^{16} \text{ cm}^{-3}$ ($4.2 \times 10^{15} \text{ cm}^{-3}$).

While fitting the capacitance transients, we find that a biexponential fit works well to describe the data, which supports the hypothesis of two specific ionic contributions, rather than a broad distribution of a single peak⁹⁰. Within each of these migration pathways, however, we cannot completely exclude some distribution in the activation energy and/or diffusion coefficient.

Looking at the results in Figure 4.4, we note that we would expect a reduced diffusion coefficient when the activation energy increases if nothing else changes, contrary to our observation. If we expand the full Equation for the diffusion coefficient D_{ion} , we find:

$$D_{ion} = \frac{v_a d^2}{6} \exp\left(\frac{\Delta S}{k_B}\right) \exp\left(\frac{-\Delta H}{k_B T}\right)$$

with v_a the attempt frequency for the ionic jump, d the ionic jump distance, ΔS and ΔH the changes in Gibbs free entropy and enthalpy of activation for a single ion migration step⁵¹.

The combination of an increased activation energy with a constant diffusion coefficient suggests a compensating term when the average grain size is increased: this could be either an increase in the attempt frequency v_a , an increase in the ionic jump distance d , or an increase in the entropy term ΔS . Regarding the first hypothesis, the presence of uncoordinated atoms in the grain boundary region suggests weaker bonding of the perovskite lattice at these grain boundaries, which is generally related to lower attempt-to-escape frequencies. This would lead indeed to an increase of v_a with grain size. If we consider the ionic jump distance d , and follow our previous statement that the defect formation energy is independent of grain size, then d should remain constant with grain size. On the other hand, at grain boundaries, the higher degrees of freedom suggest that ΔS should increase with the amount of grain boundaries, i.e. the trend would consist of a decrease of ΔS with grain size. To-

gether, these suggest that the compensating term is an increase of the attempt to escape frequency v_a .

We note that, as discussed in Section 4.2.1, the extraction layers are chosen specifically because they exhibit no direct ion migration, even though they may reduce the overall PCE of the devices. Ion migration through the extraction layers into the contact layers may still happen on long timescales¹⁵⁷.

DLTS MEASUREMENTS The vacancies necessary for ion migration to occur are part of the wider range of traps and charged point defects that hybrid halide perovskites exhibit³². We can study this trap behavior using a deep level transient spectroscopy (DLTS) measurement. DLTS is similar to TID, only the duration of the voltage pulse is shorter, such that traps have enough time to be filled, but ions do not have sufficient time to diffuse⁵¹. This technique has been extensively used in the past to measure trap state energy and density¹⁵⁸.

Here we apply a filling pulse of 1 V for a duration of 20 ms to the cells with smallest and largest grain size. The resulting transients are fitted with a global fit procedure, analogous to the one presented for TID.

The fitting function has the same form as Equation 3.1,

$$C(t, T) = C_{\infty}(T) + \Delta C(T) \exp\left(\frac{-t}{p_{fit} T \exp\left(\frac{E_T}{k_B T}\right)}\right)$$

but now with E_T the trap depth (replacing the activation energy E_a). The only difference lies in the conversion of the factor p_{fit} to the attempt frequency A_0 relevant for traps, where

$$A_0 = \frac{1}{(p_{fit} \times T^3)}$$

with A_0 the temperature-independent attempt frequency. Often $A(T) = A_0 T^2$, the temperature-dependent attempt frequency, is used.

The observation of traps (and not ions) in the DLTS measurements is further confirmed by the fact that the observed trend in DLTS (energy decrease for cells with smallest grain size) is opposite to the one observed in TID for the mobile ions. From this analysis, it also follows that the density of mobile ions is not directly related to the density of traps in the perovskite layer.

Both trap density and trap depth shown in Section 3.2.5 suggest an increased recombination of electrons and holes for the cells with smallest

grain size. On the other hand, the attempt frequency at room temperature $A(300\text{ K})$ is higher for the devices with smallest grain size, resulting in the following picture: the dense number of deep traps in cells with small grain size can counteract the higher attempt to escape frequency, thereby maintaining a constant level of non-radiative recombination in cells with small and large grain size. This is one possibility to explain the constant V_{OC} of the devices with respect to grain size. Another possibility is that the constant V_{OC} is a consequence of an interfacial energetic barrier between the perovskite and one of the transport layers, rather than being determined by the recombination rate - the constant V_{OC} with regard to grain size would thus be linked to the materials' energetic offset and the resulting interfacial recombination.

4.4.3 MODEL OF ION MIGRATION PATHWAYS

The scheme of migration pathways presented in Figure 4.5 can be further used to estimate key parameters in the bromide migration process at play. Indeed, from the activation energies of peak A in Figure 4.4, we can recover the two underlying activation energies needed for the migration from bulk to grain boundaries, and from grain boundaries to the electrode.

To do so, we use a geometric model as shown in Figure 4.8. Any given bromide ion will travel a distance $L1$ inside the bulk, then $L2$ through the grain boundary, here represented as the edge of the rectangle. If the ion starts in position (x, y) , where x is the distance between the ion and the electrode in the vertical plane, and y is the distance between ion and grain boundary in the horizontal plane, then the fraction f of bulk travelling distance to total travelling distance, $f = \frac{L1}{L1 + L2}$, is equal to the following expression:

$$f[v1, v2, L, H] = \frac{\int_0^{x_{max}} dx \int_{y_{min}}^H dy \frac{1}{1 - \frac{v1}{v2} + \frac{y}{x} \sqrt{1 - \left(\frac{v1}{v2}\right)^2}}}{\int_0^{x_{max}} dx \int_{y_{min}}^H dy}$$

with distances as defined in Figure 4.9, where x_{max} is the minimal value between $x_{max} = \frac{L}{2}$ and $x_{max} = \frac{H(v2 - v1)}{\sqrt{v2^2 - v1^2}}$, and

$y_{min} = x \frac{\sqrt{v2^2 - v1^2}}{v2 - v1}$. The expression for f thus takes into account all possible starting values for (x, y) .

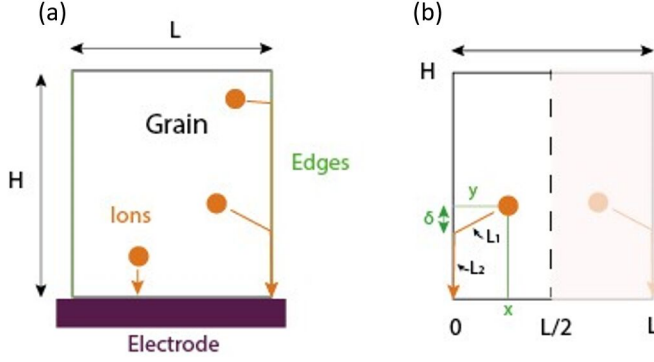


FIGURE 4.9. (a) Geometric scheme showing bromide ions within a perovskite grain for a grain of height H and length L , on top of an electrode. The inside of the rectangle represents the bulk of the perovskite lattice, while the edges of the rectangle represent grain boundaries. (b) Mean free path from the grain interior to the electrode of opposite polarity of an ion located at position (x, y) , with $L = L_1 + L_2$, L_1 being the distance from grain interior to grain boundary, and L_2 from grain boundary to electrode.

The effective activation energy of peak A, $E_{a(eff)}(A)$ can be written

$$E_{a(eff)}(A) = f E_a(1) + (1 - f) E_a(2)$$

where $E_a(1)$ and $E_a(2)$ are the bromide migration activation energies from bulk to grain boundary and from grain boundary to electrode, respectively, where the conversion relation from v_1 to $E_a(1)$, and from v_2 to $E_a(2)$ are $v_1 = \exp[-E_a(1)]$ and $v_2 = \exp[-E_a(2)]$. We note that this simplification assumes that the diffusion coefficient for both pathways is identical and only the activation energy is different, as also indicated by our measurement (Figure 4.4d).

We can now estimate $E_a(1)$ and $E_a(2)$, by solving the previous Equation for various sets of $(E_a(1), E_a(2))$ and try to find the best fit to the activation energies of peak A. The results are shown in Figure 4.10. We note that the x-axis for activation energies of peak A (as shown in Figure 4.4c) is transformed from grain size to a new metric of grain size over thickness of the perovskite layer, allowing to plot all experimental values

on the same axis as the fitted values. The simple model we used predicts a change in the activation energy for aspect ratios between 0 and 2, while our experimental data shows an onset starting around 7.8. The failure to account for the delayed onset of the activation energy change is likely due to the simplicity of our model, which does not account for the distribution of grain sizes in each sample, a possibly rough grain boundary, and for the contribution of a slower diffusion paths to the capacitance decay. Nevertheless, if we shift the x-axis of the model by 7.8, we can reproduce the trend of the activation energy increase as a function of grain aspect-ratio. The plot in Figure 4.5c was obtained with fitted values of the activation energies of 0.50 eV for bulk diffusion and 0.18 eV for grain-boundary diffusion. While not attempting a precise description of the experimental data our model shows the effect that a varying grain size has on the geometry of the ion's path, rationalizing the experimental trend.

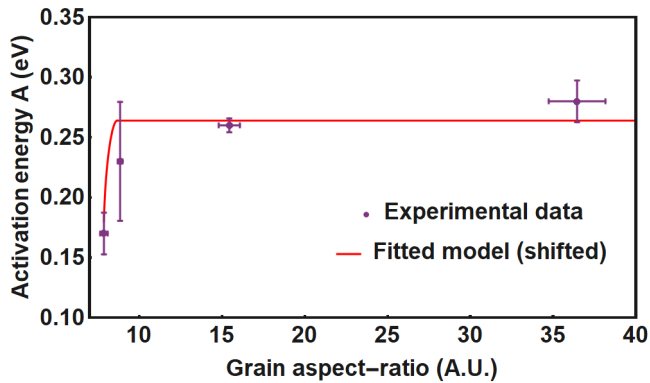


FIGURE 4.10. Experimental activation energies of peak A in purple, rescaled as a function of length over thickness and shifted to lower x-values; fitted geometrical model in red, using values of 0.50 eV for bulk diffusion and 0.18 eV for grain-boundary diffusion. We further note that TID cannot unveil the microscopic pathways of ion diffusion in the perovskite layer, but remains an interesting tool that can be further complemented by theoretical modelling using DFT and MD simulations.

5 2D OR NOT 2D

REDUCED ION MIGRATION BY ADDITION OF A 2D LAYER, COMPARING PEA, FEA AND MIXED PEA/FEA

2D/3D perovskite solar cells, where a thin 2D perovskite layer is deposited onto a thick 3D perovskite layer, have recently emerged as a promising avenue to combine both the high efficiency of the 3D perovskites and the increased stability of the 2D perovskites. In fully 2D perovskite devices, ion migration appears to be reduced or suppressed compared to the fully 3D systems. However, it remains unclear if ion migration in a 2D/3D perovskite solar cell is affected by the presence of the thin 2D layer at the interface between the 3D perovskite and the hole transport layer. Here, we study the influence of the addition of this thin 2D layer on ion migration in the full 2D/3D solar cell devices. We further evaluate the effect of the 2D spacer layer composition by varying the 2D spacer molecules between FEA, PEA or a mix of FEA and PEA, and find that in all devices incorporating a 2D layer, ion migration is hindered. Upon addition of the FEA 2D layer, the density of one of the mobile halide ions decreases from 41 % to 15 % of the doping density; while addition of the PEA 2D layer affects the second mobile halide ion, by decreasing its density from 60 % to 25 % of the doping density, and increasing the migration activation energy from 65 meV to 110 meV. Our quantitative analysis of ion migration thus allows us to distinguish different mechanisms of ion migration suppression, dependent on the 2D spacer composition.

This chapter is based on the following publication:
Lucie McGovern, Rens van Roosmalen, Anwar Alanazi, Gianluca Grimaldi, Moritz C. Schmidt, Jovana V. Milić and Bruno Ehrler, "Effect of a 2D layer on ion migration in perovskite solar cells, comparing PEA, FEA and mixed PEA/FEA systems", in preparation.

5.1 INTRODUCTION

Perovskite solar cells have recently emerged as one of the most promising material platforms for optoelectronic devices. Combining high Power Conversion Efficiencies (PCEs)^{159–161}, cheap synthesis and fabrication methods^{162–164}, and bandgap tunability by simple modification of the perovskite composition¹¹, they appear as an outstanding candidate in the field of photovoltaic research¹⁰, where efforts for better and cheaper solar cells are continuously ongoing. However, perovskite solar cells are still affected by a major drawback, which is their instability. Modules tend to degrade with time and have been shown to be sensitive to a range of environmental factors^{19,165,166}, impeding their large-scale commercialisation. Ion migration, the process whereby an ion from the ABX_3 perovskite structure detaches and becomes mobile within the perovskite layer, is a particular challenge in lead halide perovskites, as it is an intrinsic source of instability in these devices⁶⁰. Finding a reliable, simple, and robust mitigation strategy against ion migration in perovskite solar cells is thus a desirable goal, which would allow these devices to contribute to the ever-growing global need for energy¹⁶⁷.

In this context, 2D perovskite devices have recently emerged as an opportunity for increased stability in the field of perovskite solar cells^{168–171}. In 2D perovskite layers, the lead halide inorganic sheets are separated by organic spacer molecules (called 2D spacer molecules), which are large organic cations that replace some of the small A-site cations present in the 3D perovskites¹⁶⁹. The general formula for the structure is $B_2A_{n-1}Pb_nI_{3n+1}$, where B is the replacement cation and n is the number of perovskite inorganic sheets, tunable by adjusting the mixing ratio of 3D cations to 2D spacer molecules.

Adding the 2D spacer layer to 3D perovskite solar cells has been shown to offer increased protection against humidity and thermal stress^{172–176}. However, these devices suffer from a reduced PCE in comparison with their 3D counterparts. After optimisation in the device preparation, state-of-the-art 2D perovskite devices now reach competitive PCEs above 14%¹⁷⁷, but remain below the record 25.7% found for 3D perovskites¹⁵⁹. More recently, new devices combining a bulk 3D perovskite layer with a thin 2D layer have appeared, to benefit both from the increased stability offered by the 2D layer, and from the higher efficiency offered by the

3D layer. These 2D/3D heterostructures already reach efficiencies over 20 % (efficiencies of 21 % and 23 % were recently demonstrated^{178,179}) and, most remarkably, have been shown to maintain their PCE for over a year^{180–182}. While the impact of the 2D perovskite layer on external instability sources is thus established, how these 2D perovskite layers affect the ion migration dynamics in the 2D/3D heterostructures remains an open question.

Initial works on this topic of ion migration in 2D perovskites include conductivity^{183,184}, TOF-SIMS⁴³ and absorption spectroscopy measurements¹⁸⁵, all indicating a reduction of ion migration in the low-dimensional perovskite layers. Lin *et al.* and Xiao *et al.* showed that ion migration was completely suppressed in fully 2D perovskites - both along the out-of-plane and in-plane directions - when using n-butylammonium (BA) (with $n = 3$ or $n = 4$) as the 2D spacer molecule^{183,184}. Huang *et al.* looked at TOF-SIMS signals of 3D perovskites and compared these with those of 2D perovskites with large n -values. They found that iodide was the dominant species migrating in the 3D devices, and that this migration was suppressed in the case of the 2D perovskites⁴³. Cho *et al.* compared the speed of halide remixing as a function of n , and found that with lower n values, the halide remixing took longer, indicating an energy barrier against ion migration for the lower-dimensionality perovskites¹⁸⁵. While there seems to be an emerging consensus that 2D perovskites can either mitigate or altogether suppress the ion migration in fully 2D perovskite devices, some questions remain unanswered. These include the quantification of the effect of the 2D layer, whether a thin 2D perovskite layer has any influence on the ion migration dynamics within a stack that contains a much thicker 3D layer, and the potential impact of the 2D organic cation spacer itself.

To study these questions, we use efficient 2D/3D solar cell devices prepared with a range of 2D spacer molecules, and measure small variations induced by these thin 2D perovskite layers on top of the 3D perovskite.

5.2 RESULTS AND DISCUSSION

5.2.1 2D/3D DEVICE FABRICATION, WITH FEA, PEA AND MIXED FEA/PEA AS 2D SPACER MOLECULES

We fabricate a range of 2D/3D perovskite stacks using either pentafluorophenethylammonium (FEA), phenethylammonium (PEA), or a mix of FEA/PEA as the 2D spacer molecule in the 2D perovskite layer. We

further complement our range of devices with a reference device containing only the 3D perovskite and no additional 2D layer. The 3D layer is a mixed-halide $\text{MAPb}(\text{I}_{0.95}\text{Br}_{0.05})_3$ perovskite. All devices have a p-i-n architecture with compact TiO_2 (C- TiO_2) and mesoporous TiO_2 (M- TiO_2) as Electron Transport Layers (ETLs) and Spiro-OMeTAD as the Hole Transport Layer (HTL). The devices are completed with Fluorine doped Tin Oxide (FTO) and gold electrodes for current extraction. An illustration is shown in Figure 5.1.

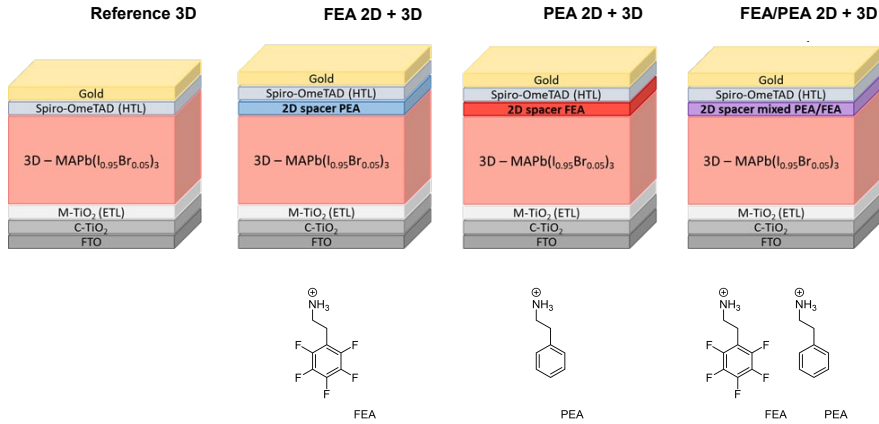


FIGURE 5.1. Solar cell device stacks, where the 3D layer is a mixed-halide $\text{MAPb}(\text{I}_{0.95}\text{Br}_{0.05})_3$ perovskite, the ETL consists of a combination of C- TiO_2 and M- TiO_2 , the HTL is Spiro-OMeTAD, and the bottom and top electrodes are respectively FTO and gold. Except for the pure 3D sample, a thin 2D perovskite layer is added on top of the 3D perovskite layer, where the 2D spacer molecule is varied to obtain a range of 2D/3D stacks. The 2D spacer molecules used are FEA, PEA or a mix of FEA/PEA. The organic spacers FEA and PEA are shown below their respective stacks.

The 2D spacer molecules FEA and PEA both consist of an aromatic ring and an ammonium group, the latter allowing for coordination to the perovskite octahedra. FEA and PEA differ in the electron density distribution across the aromatic rings: fluorine atoms remove electron density from the aromatic ring in the FEA system, leading to a low electron density in the centre of the aromatic ring, whereas the electron density is highest in the centre of the aromatic ring in the PEA system. This change in the electronic distribution will modify the stacking of the 2D molecules within the 2D layer: as shown in Figure 5.2, the PEA molecules can either adopt a $\pi - \pi$ interaction with a T-shaped (t), parallel displaced

(d) or parallel (p) orientation (with interaction strengths $\pi_T \sim \pi_d < \pi_p$), while the FEA molecules will favor parallel $\pi - \pi$ interactions, π_p . In turn, this affects the strength and nature of the supramolecular interaction between the 2D and 3D perovskites¹⁸⁶. Our investigation thus extends the characterisation of ion migration to 2D perovskite systems with fluorine containing spacers, in which the change in electronic density leads to a difference in the supramolecular interaction, which could affect the energy barrier for ionic motion. This variation will allow us to study whether the ion migration properties of the 2D/3D perovskite devices are impacted by the composition of the 2D spacer layer itself.

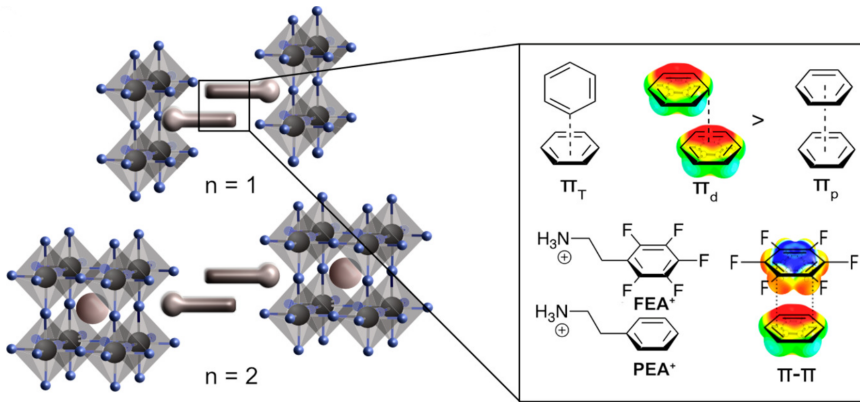


FIGURE 5.2. Illustration scheme of the possible supramolecular interactions formed within the 2D perovskite layers of either PEA or FEA. The strength of the $\pi - \pi$ interaction is dependent on the aromatic ring orientation, whether T-shaped, parallel displaced or parallel. Reproduced from reference 186.

5.2.2 THERMAL ADMITTANCE SPECTROSCOPY AND TRANSIENT ION DRIFT CHARACTERISATION

We measure the Thermal Admittance Spectra (TAS) of the 2D/3D perovskite devices, as shown in Figure 5.3a-d. We find that in the low-frequency regime below 10^2 Hz, the capacitance shows very high values, from 250 to 1750 nF cm^{-2} , depending on the 2D spacer molecule and on the temperature. This low-frequency feature increases with temperature, indicating a thermally activated process. This feature is in line with previous works using devices with a p-i-n architecture and TiO_2 as the ETL⁹⁷. It stems from an activated process in this transport layer or at the TiO_2 /perovskite interface. The mobile ion response in per-

ovskite cells is usually also present in this frequency range¹⁸⁷, but this feature is expected to have lower intensity than the one observed here, especially considering that the TAS measurements are taken under dark conditions⁵². We thus assign this low-frequency peak to an effect of the TiO₂ layer, possibly convoluted with a mobile ion response. Since we are not interested in the effect of the TiO₂/perovskite interface on the capacitance, we measure at a higher frequency where this feature is absent. At higher frequencies above 10² Hz, the capacitance spectra decrease to a plateau-like shape with values in the range of 50 to 150 nF cm⁻². In this frequency regime, the plateau-like spectral shape is temperature independent (see insets in Figure 5.3a-d), and the only influence of temperature is in the small shift to higher capacitance values at higher temperatures. The capacitance in this frequency regime corresponds to geometric capacitance⁵², where the device is approximated as a parallel-plate capacitor. There, we assume that the small shift with temperature is linked to the previously-reported variation of the perovskite permittivity with temperature¹⁰¹.

We are interested in the effect of the 2D layer on ion migration. As the mobile ion response in TAS is shadowed by the effect of the TiO₂ layer, we turn to Transient Ion Drift (TID) for mobile ion characterisation in these devices. There, we choose an AC frequency of 10⁴ Hz to measure the capacitance, in the intermediate frequency regime as defined above, where the capacitance corresponds to geometric capacitance. The resulting TID capacitance datasets, taken after applying a filling voltage of 1.2 V, are shown in Figure 5.3e-h. More TID capacitance datasets, taken after applying voltage pulses of 0.8 V and 1 V, are presented in Section 5.4.2. Qualitatively, the first observation is the similarity in the TID transients of the various 2D/3D perovskite devices. An initial rise in capacitance is observed in the first 10 to 20 milliseconds – this rise is mostly present at higher temperatures, above 310 K – and is followed by a decay in the following timeframe, before the capacitance transients reach their steady-state values after 100 to 200 milliseconds. This first qualitative observation is an indication for similar ion migration processes happening in the range of 2D/3D perovskite devices studied here, prepared with a 2D layer made by using FEA, PEA or a mix of FEA and PEA as the 2D spacer molecule and in the 3D devices. In the 2D/3D devices, the 2D perovskite layer is thin compared to the bulk 3D layer, so this similarity might be expected as most of the ion migration happens through the bulk. On the other hand, the TID transients, if similar, also clearly show some differences, with an evolution of the temperature at

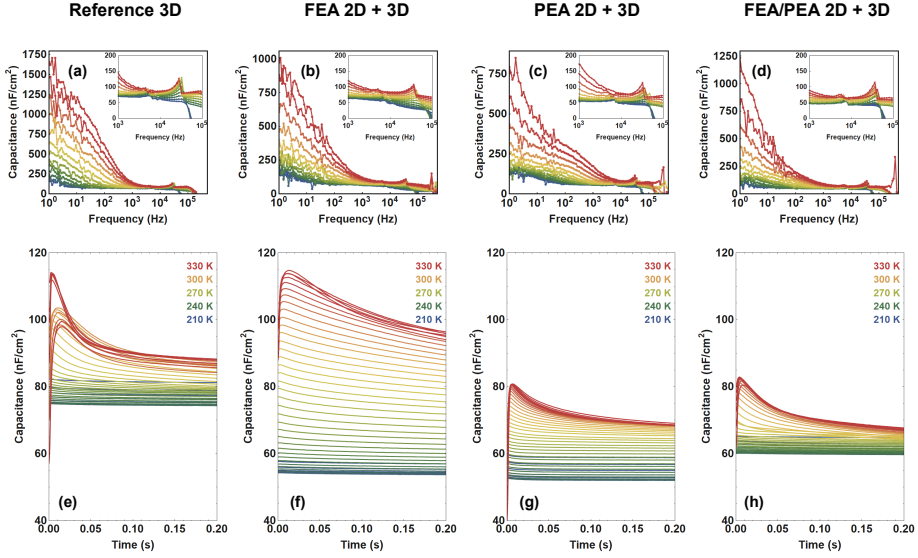


FIGURE 5.3. Admittance spectra of the 2D/3D perovskite solar cell devices, with (a) no 2D layer, (b) the 2D layer with FEA, (c) the 2D layer with PEA and (d) the 2D layer with a mix of FEA and PEA. The admittance spectra were taken at 300 K in the dark, using an AC voltage of 10 mV. TID capacitance transients of the 2D/3D perovskite solar cell devices, with (e) no 2D layer, (f) the 2D layer with FEA, (g) the 2D layer with PEA and (h) the 2D layer with a mix of FEA and PEA. The capacitance transients are taken after applying a voltage pulse of 1.2 V for 2 s and are measured at 10 kHz with an AC voltage of 10 mV. The capacitance traces are taken from 210 K to 330 K, and shown here in temperature steps of 30 K.

which the ion migration process is first observed, but also an evolution in the specific time dynamics for each of the 2D/3D perovskite systems. To further study the mobile ion dynamics in the 2D/3D systems and obtain a quantitative picture, we analyse the transients and fit them to an analytical model. The fitting procedure is detailed in the next paragraph.

5.2.3 QUANTIFICATION OF THE ION MIGRATION CHARACTERISTICS

The TID transients are fitted to Equation 5.1, where $C(t, T)$ is the capacitance at time t and temperature T , $C_{\infty}(T)$ is the steady-state capacitance at temperature T , $\Delta C_n(T)$ is the amplitude of the process n in the transient of temperature T , $p_{fit(n)}$ is a fitting parameter associated

to process n and used to calculate the diffusion coefficient in later stages, and $E_{a(n)}$ is the activation energy of ion migration in process n .

$$C(t, T) = C_{\infty}(T) + \sum_n \Delta C_n(T) \exp\left(\frac{-t}{p_{fit(n)} T \exp\left(\frac{E_{a(n)}}{k_B T}\right)}\right) \quad (5.1)$$

We fit the full set of transients (measured at different temperatures) from one TID dataset in a single global fit. This allows us to determine the global values for both $p_{fit(n)}$ and $E_{a(n)}$ for each of the n processes taking place, and to determine the list of $\Delta C_n(T)$ values at each temperature. To increase the fitting speed, we use a differential evolution algorithm: candidate solutions are proposed and iteratively improved based on a genetic process. In other words, “parent” solutions are combined to find the next generation of improved solutions, labelled “daughter” solutions. Such algorithms are efficient at finding global minima of the cost function in large and complex parameter spaces¹⁸⁸. Further details are provided in Section 5.4.3.

The fitting procedure requires 3 exponential contributions to accurately describe the datasets, where one of the contributions describes a capacitance rise, and the two other contributions correspond to the decay dynamics.

We first consider the rise feature. This contribution is present mostly at higher temperatures and it is dependent on the applied voltage pulse (see Figures 5.5 and 5.6 in Section 5.4). At lower filling voltages, this rise starts with very low initial capacitance values at early times, below 40 nF cm^{-2} in the extreme cases. Negative capacitance and capacitance close to zero have been observed in impedance measurements with TiO_2 /perovskite devices in the low-frequency regime¹⁸⁹ and are often attributed to a surface-ionic interaction. We believe that a similar mechanism upon the (seconds-long) voltage pulse leads to the initial low capacitance. When we take this feature into account for the fitting algorithm, it requires very large $\Delta C_n(T)$ values for the rise process. The TID model, however, assumes a small concentration of ions (compared to the background charge density), and hence the fitted values are above the assumption made in our model (see Section 1.6). For these reasons we exclude the rise feature from the analysis. Drift-diffusion modelling of the system could prove beneficial in the attribution of this rise event

to either an interfacial effect, or an electronic process in the perovskite layer.

The two decay features are present at all temperatures and in a reliable manner for each of the filling voltages applied (see Figure 5.3 in Section 5.2.2, and Figures 5.5 and 5.6 in Section 5.4.2), we thus attribute them to ion migration processes in the 2D/3D perovskite heterostructure devices. If we assume that the perovskite is p-type^{122,190,191}, then a decay in TID capacitance corresponds to migration from an anion species. In the case of lead halide perovskites, this capacitance decay is thus attributed to migration from the halide species. This result matches well with literature, as the halide ion is often found to be the most mobile ion species in perovskite solar cells^{43,56,108}.

5.2.4 HALIDE MIGRATION IN THE 2D/3D PEROVSKITES

We now look at the quantified picture of halide migration in the fabricated solar cell devices and study the influence of the thin 2D layer on the ion dynamics in the full 2D/3D perovskite system, comparing the reference device prepared with only the 3D perovskite, and the 2D/3D perovskites made using either FEA, PEA or a mix of these two as the 2D spacer molecule. We find that in all systems incorporating a 2D layer, the halide migration process is hindered compared to the pure 3D case. The nature of this reduction in ion migration is, however, dependent on the composition of the 2D perovskite. The values plotted in Figure 5.4 are also reproduced in Table I for clarity.

The device including FEA for the 2D thin layer acts as a barrier for halide ion migration by reducing the mobile ion density of one of the mobile species, which we call Halide (1), shown in orange in Figure 5.4b. Specifically, the mobile ion density decreases from 41 % to 15 % of the doping density.

The device including PEA for the 2D thin layer also acts as a barrier for halide ion migration, but the mechanism is different. There, on top of the reduction in mobile ion density - from $\sim 60\%$ to 25% of the doping density, there is also a significant increase in the activation energy for the migration step of Halide (2), from $\sim 65\text{ meV}$ without PEA to 110 meV after addition of PEA as the 2D spacer molecule. Interestingly, both activation energy and density of Halide (2) are affected by PEA, compared to the system with FEA which affects the Halide (1) process only.

We also study the effect of mixing both FEA and PEA as spacer

molecules in the thin 2D layer. This mixture leads to supramolecular interaction which should strengthen the interaction within the 2D spacer layer^{173,192–194}. There, similar to the case with PEA only, we observe both an increase in the activation energy of Halide (2), and a decrease in the density of mobile Halide (2) ion. The values are comparable when using either only PEA or the mix of PEA and FEA: the activation energy remains 110 meV, and the mobile ion density arrives at $(25 \pm 5) \%$ and $(28 \pm 13) \%$ of the doping density. In other words, the ion migration effect observed when using the mixed FEA/PEA system is dominated by the ion migration response of PEA.

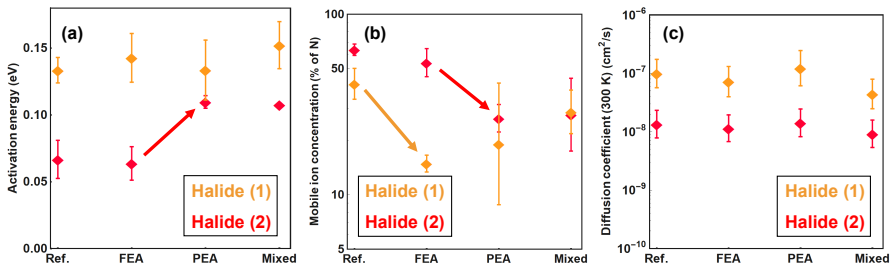


FIGURE 5.4. Ion migration characteristics of the 2D/3D perovskite solar cell devices prepared either with no 2D layer, or FEA, PEA or a mix of FEA and PEA as 2D spacer molecule in the 2D perovskite layer; with (a) the activation energies for the migration step, (b) the density of mobile ions, and (c) the diffusion coefficient of these mobile ions. The 2 different mobile halide species are shown in orange and in red.

The feature that remains constant between the fully 3D perovskite system and all of the 2D/3D perovskite systems studied here is the ion diffusion coefficients of mobile ion species Halide (1) and Halide (2). To test whether these values can indeed be considered constant, we use an unpaired student's t-test, and find that there is no statistically significant trend as a function of the 2D spacer layer. The diffusion coefficient of Halide (1) is on the order of $10^{-7} \text{ cm}^2\text{s}^{-1}$, and that of Halide (2) on the order of $10^{-8} \text{ cm}^2\text{s}^{-1}$. Both diffusion coefficients are in line with previous works on the halide diffusion coefficient in perovskite solar cells^{56,76,124}.

The migration activation energies in the fully 3D reference system are very close to those previously found for the mixed-halide perovskite of similar composition, $\text{MAPbBr}_{0.3}\text{I}_{2.7}$ (see Chapter 3, Section 3.2.3)¹⁰⁴. This 3D perovskite with 10% bromide addition showed two mobile halide species with activation energies of 0.060 eV and 0.150 eV¹⁰⁴, comparable

	Pure 3D	FEA 2D + 3D	PEA 2D + 3D	FEA/PEA 2D + 3D
E_a Halide (1) (eV)	$0.134 \pm$ 0.010	$0.143 \pm$ 0.018	$0.134 \pm$ 0.022	$0.152 \pm$ 0.018
E_a Halide (2) (eV)	$0.067 \pm$ 0.014	$0.064 \pm$ 0.013	$0.110 \pm$ 0.005	$0.108 \pm$ 0.001
Density Halide (1) (% of N_D)	41 ± 8	15 ± 1.6	19 ± 15	29 ± 8
Density Halide (2) (% of N_D)	64 ± 5	54 ± 10	25 ± 5	28 ± 13
D Halide (1) ($\text{cm}^2 \text{s}^{-1}$)	(1.0 ± 0.6) $\times 10^{-7}$	(7.0 ± 4.0) $\times 10^{-8}$	(1.2 ± 0.9) $\times 10^{-7}$	(4.4 ± 2.6) $\times 10^{-8}$
D Halide (2) ($\text{cm}^2 \text{s}^{-1}$)	(1.3 ± 0.7) $\times 10^{-8}$	(1.1 ± 0.6) $\times 10^{-8}$	(1.4 ± 0.8) $\times 10^{-8}$	(9.0 ± 5.0) $\times 10^{-9}$

TABLE I. Extracted parameters for the activation energies, the mobile ion densities, and the diffusion coefficients of the mobile ion species (1) and (2) as measured by TID spectroscopy in the 2D/3D perovskite solar cell devices.

to the 0.067 eV and 0.134 eV found here, suggesting similar migration pathways in both of these mixed-halide 3D perovskites. When comparing the mobile ion densities of Halide (1) and Halide (2) in the fully 3D reference system, we find that they are both on the same order of magnitude, with (41 ± 8) % of the doping density for Halide (1), and (65 ± 5) % for Halide (2). The bromide concentration in the 3D perovskite represents only 5 % of the iodide concentration: if the two different mobile ions Halide (1) and Halide (2) were iodide and bromide, we would expect a clear difference in the density of mobile ions. The similarity in mobile ion density thus suggests that both contributions stem from the prominent halide in the $\text{MAPb}(\text{I}_{0.95}\text{Br}_{0.05})_3$ perovskite, i.e. the iodide species. This is in line with previous work showing iodide to be a more mobile ion than bromide^{68,73,116}. We thus attribute the two migration processes Halide

(1) and Halide (2) to iodide migration. Determining the specific nature of the two different migration processes would facilitate the development of strategies to manage ion migration, and thus calls for future investigation. We also note the large uncertainty in the determination of the halide density. This is partially due to a large sample-to-sample variation, and partially because at such high density (compared to the doping density) the ions are not forming a mere perturbation to the electric field distribution inside the device. Hence, the simple theory we use for the analysis is not entirely accurate, limiting the accuracy with which we can determine the ion density. Ongoing work on simulating the full electric field distribution in the device could shed light on these uncertainties.

Together, our results thus show a prominent effect of the thin 2D layer addition on top of the thicker 3D perovskite in terms of ion migration reduction. To observe such a large effect might be surprising, considering the difference in thickness between these two layers. One explanation might come from the role of the transport layers in the perovskite device stacks. In our general model of lead halide perovskite devices, we assume that these transport layers are fully ion-blocking, meaning that the mobile ions only drift through the perovskite layer and to the interface between perovskite and transport layer. If, however, there is some transfer of the mobile ions into the transport layers, in other words if this hypothesis is invalid in the fully 3D case, then the impact of a completely ion-blocking layer, however thick, at the interface with this 3D perovskite would be consequential. We thus consider the 2D perovskite layer to have better ion-blocking properties than the usual electron and hole transport layers.

5.3 CONCLUSION

We study the influence of the addition of a thin 2D perovskite layer on top of a bulk 3D perovskite layer, in terms of ion migration in the full 2D/3D solar cell device, and further evaluate the effect of the 2D perovskite composition by varying the 2D spacer molecules with FEA, PEA or a mix of FEA and PEA. We find that in all systems incorporating a 2D perovskite layer, the 2D/3D solar cell device shows a reduction in halide migration. The mechanism however differs, with either a reduction in the mobile density of Halide (1) for the pure-FEA case, or a combination of a reduction in the mobile density and an increase in the activation energy of Halide (2) for the pure-PEA case and the mixed FEA and PEA

case. These results highlight the crucial role played by 2D perovskites in hindering ion diffusion through the stack of efficient solar cell devices, while suggesting the presence of different mechanisms of blocking ion migration for different 2D spacers. Detailed understanding of the impact of the 2D spacer on ion migration processes might finally pave the way towards perovskite photovoltaics with long term stability.

5.4 APPENDIX

5.4.1 DEVICE FABRICATION

The devices are fabricated according to previously published procedures^{173,186,193}. The thickness of the 3D perovskite layer was shown to vary between 400 and 500 nm.

5.4.2 ELECTRICAL MEASUREMENTS

All electrical measurements are taken in the dark, using a commercially available setup from Semetrol and a JANIS VPF-100 cryostat. To avoid oxygen or moisture contamination, the pressure is kept below 7×10^{-6} mbar during the measurements and the loading of the samples into the cryostat takes place in a nitrogen-filled glovebox.

TAS spectra are recorded from 1 Hz to 500 kHz in 100 steps, using a 10 mV perturbation voltage. The measurement is repeated every 10 K, from 210 K up to 340 K. We measure TID after applying a voltage pulse for 2 seconds and record the capacitance transients between 210 and 330 K, with temperature steps of 3 K. The different filling voltages applied are 0.8, 1.0 and 1.2 V, and the AC perturbation voltage used to measure capacitance is 10 mV applied with a frequency of 10 kHz. For each temperature transient, 2033 data points are collected (i.e. ~ 1 s after $t = 0$), and the capacitance transients are averaged over 20 repetitions before moving to the next transient. All TAS and TID measurements are repeated on 2 different cells, coming from separate batches prepared by using the same recipe (i.e. two pure 3D cells and six 2D/3D systems, with 2 \times FEA, 2 \times PEA and 2 \times mixed FEA/PEA).

The TID technique, as well as the analytical model and hypotheses used, are described in Chapter 1 of this thesis.

In Figures 5.5 and 5.6, we show the TID datasets after applying filling voltages of 0.8 V and 1 V, for the 4 different types of solar cell devices prepared - the pure 3D device, and the set of 2D/3D heterostructure devices with FEA, PEA and the mixture of FEA and PEA as 2D spacer molecules. In Figure 5.5, which represents the case after applying a voltage of 0.8 V, we notice that the transients are visible, but have a much lower magnitude than in the cases with filling voltages of 1 V or 1.2 V (shown in Figure 5.6 and Figure 5.3, respectively). We conclude that 0.8 V is not sufficient to fully collapse the depletion in the devices. In Figure 5.6 however, which represents the case after applying a voltage of 1 V, we notice that the dynamics in the capacitance transients are very

similar to those observed after applying a voltage of 1.2 V, with an initial rise in the first 10 to 20 ms before a decay in the following 100 ms, and finally a saturation after ~ 150 ms. This indicates that the 1 V filling voltage is sufficient for the devices to be almost or fully depleted, and that the ion migration dynamics taking place are equivalent to those observed after application of the 1.2 V filling bias. To obtain a reliable quantification of the ion migration dynamics in the 2D/3D perovskite systems, we thus decide to use the TID datasets measured at 1 V and 1.2 V.

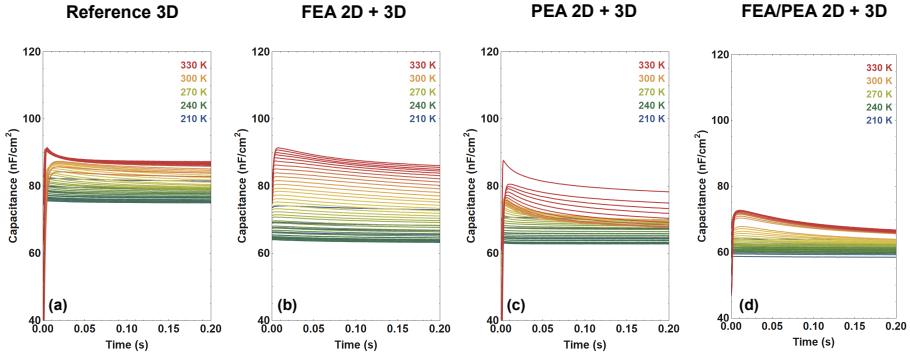


FIGURE 5.5. TID capacitance transients of the 2D/3D perovskite solar cell devices taken after applying a voltage pulse of 0.8 V for 2 s, for the devices with (a) no 2D layer, (b) the 2D layer with FEA, (c) the 2D layer with PEA and (d) the 2D layer with a mix of FEA and PEA. The capacitance transients are measured at 10 kHz with an AC voltage of 10 mV. The capacitance traces are taken from 210 K to 330 K, with temperature steps of 3 K.

The feature which evolves the most between the 0.8 and 1 V TID datasets compared to the 1.2 V TID dataset is the magnitude of the initial rise event, where the peak shows larger magnitude in the 2 cases with lower voltage pulses. This observation further strengthens our analysis of this rise event being caused by either an interface effect or an electronic process rather than an ion migration process.

5.4.3 FITTING PROCEDURE

To obtain the values shown in Figure 5.4 and in Table I, we fit the TID datasets to Equation 5.1 (shown in Section 5.2.3). For each composition, the extracted value is taken from averaging over two filling voltages (the TID datasets obtained after applying the 1 V and 1.2 V filling voltages)

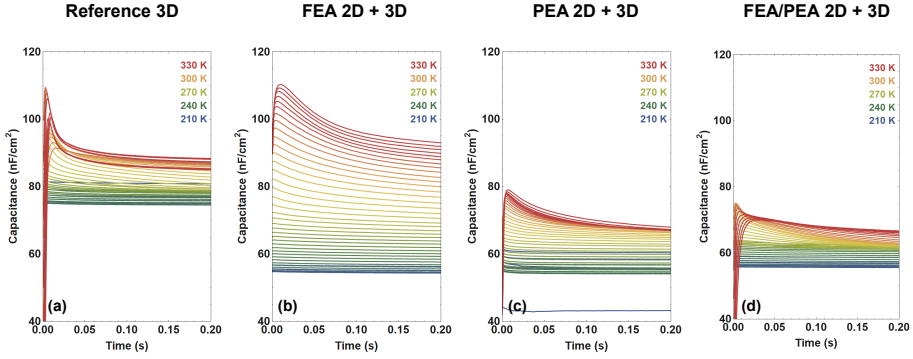


FIGURE 5.6. TID capacitance transients of the 2D/3D perovskite solar cell devices taken after applying a voltage pulse of 1 V for 2 s, for the devices with (a) no 2D layer, (b) the 2D layer with FEA, (c) the 2D layer with PEA and (d) the 2D layer with a mix of FEA and PEA. The capacitance transients are measured at 10 kHz with an AC voltage of 10 mV. The capacitance traces are taken from 210 K to 330 K, with temperature steps of 3 K.

and two device copies for each of the device compositions ($2 \times$ pure 3D, $2 \times$ FEA, $2 \times$ PEA and $2 \times$ mixed FEA/PEA). The resulting averages are thus taken over a set of 4 measurements and the error bars represent the standard deviation of the mean over these measurements. The reasoning for averaging over two filling voltages is explained in Section 5.4.2 above.

The fitting procedure is based on a differential evolution algorithm, here using `scipy`'s differential evolution function¹⁹⁵. In such differential evolution algorithms, the genetic selection of “daughter” solutions is stochastic in nature. To counteract this effect, the fitting process is repeated at least 10 times for each dataset, which allows us to acquire sufficient statistics on the obtained parameters. The solutions are then filtered based on their cost function¹⁹⁶, which is a measure of how well the fitted function matches the datasets. These are obtained by taking the sum of the residuals squared for each temperature trace and summing them together in a dataset-wide cost value. Finally, the fitted parameters of the remaining solutions are averaged – the resulting values are reported in Table I.

To avoid the cost function being dominated by the traces with the highest decay amplitudes (i.e. the traces at highest temperatures), we normalize all temperature traces prior to the fitting procedure.

The differential evolution algorithm has tunable parameters to optimise a quick route to a reliable global fit. To increase the likelihood

$\Delta C_n(T)$ (pF)	-30 to 2
$p_{fit(n)}$ (s K^{-1})	10^{-8} to 10^{-4}
$E_{a(n)}$ (eV)	0.01 to 0.3
$C_\infty(T)$ (pF)	10^{-6} to 0.5
Tolerance factor	0.002 to 0.1
Mutation factor	0.4 to 0.6
Cost treshold	6 to 33

TABLE II. Set of parameters and the range of values used for the fitting procedure.

of finding the global minimum, either more iterations, a higher mutation factor or a lower tolerance factor can be set, all at the expense of computational power. To avoid any prior bias on the results, a broad parameter range was applied throughout the entire fitting process. The typical parameter ranges used are shown in Table II.

The maximum value of the activation energy for ion migration chosen here is on the low end compared to some of the previously reported values^{86,131,148}. This range was chosen due to the observation that using higher activation energies in the initial parameter set did not result in better convergence of the extracted value. Indeed, allowing the activation energies to increase up to 1.2 V resulted in similar final values, far below 0.3 V, while the larger parameter space required significantly more computational power.

BIBLIOGRAPHY

1. “IPCC 2021: Summary for policymakers”, in *Climate Change 2021: The Physical Science Basis. Contribution of Working Group I to the Sixth Assessment Report of the Intergovernmental Panel on Climate Change*, V. Masson Delmotte, P. Zhai, A. Pirani, S. L. Connors, C. Péan, S. Berger, N. Caud, Y. Chen, L. Goldfarb, M. I. Gomis, M. Huang, K. Leitzell, E. Lonnoy, J. B. R. Matthews, T. K. Maycock, T. Waterfield, O. Yelekçi, R. Yu, and B. Zhou, Ed. Cambridge University Press, 2021.
2. H. Ritchie and M. Roser, “CO₂ and greenhouse gas emissions”, *Our World in Data*, 2020, <https://ourworldindata.org/co2-and-other-greenhouse-gas-emissions>. Last visited 01-12-2021.
3. IRENA, “Energy Transition”, <https://www.irena.org>. Last visited 29-11-2021.
4. Statista, “Global cumulative installed solar PV capacity 2020”, <https://www.statista.com/statistics/280220>. Last visited 01-12-2021.
5. Bccresearch, “A History of Perovskite Solar Cells”, <https://blog.bccresearch.com>. Last visited 25-11-2021.
6. A. Krause, W. M. Weber, D. Pohl, B. Rellinghaus, A. Kersch, and T. Mikolajick, “Investigation of band gap and permittivity of the perovskite CaTiO₃ in ultrathin layers”, *Journal of Physics D: Applied Physics*, vol. 48, no. 41, p. 415304, 2015.
7. A. Kojima, K. Teshima, Y. Shirai, and T. Miyasaka, “Organometal halide perovskites as visible-light sensitizers for photovoltaic cells”, *Journal of the American Chemical Society*, vol. 131, no. 17, pp. 6050–6051, 2009.
8. G. E. Eperon, S. D. Stranks, C. Menelaou, M. B. Johnston, L. M. Herz, and H. J. Snaith, “Formamidinium lead trihalide: a broadly tunable perovskite for efficient planar heterojunction solar cells”, *Energy & Environmental Science*, vol. 7, no. 3, pp. 982–988, 2014.

9. J. Liang, C. Wang, Y. Wang, Z. Xu, Z. Lu, Y. Ma, H. Zhu, Y. Hu, C. Xiao, X. Yi, G. Zhu, H. Lv, L. Ma, T. Chen, Z. Tie, Z. Jin, and J. Liu, “All-Inorganic Perovskite Solar Cells”, *Journal of the American Chemical Society*, vol. 138, no. 49, pp. 15 829–15 832, 2016.
10. NREL, “Cell Efficiency Chart”, <https://www.nrel.gov/pv/cell-efficiency>. Last visited 01-12-2021.
11. B. R. Sutherland and E. H. Sargent, “Perovskite photonic sources”, *Nature Photonics*, vol. 10, no. 5, pp. 295–302, 2016.
12. W. J. Yin, T. Shi, and Y. Yan, “Unusual defect physics in $\text{CH}_3\text{NH}_3\text{PbI}_3$ perovskite solar cell absorber”, *Applied Physics Letters*, vol. 104, no. 6, p. 063903, 2014.
13. S. D. Stranks, G. E. Eperon, G. Grancini, C. Menelaou, M. J. Alcocer, T. Leijtens, L. M. Herz, A. Petrozza, and H. J. Snaith, “Electron-hole diffusion lengths exceeding 1 micrometer in an organometal trihalide perovskite absorber”, *Science*, vol. 342, no. 6156, pp. 341–344, 2013.
14. T. Leijtens, S. D. Stranks, G. E. Eperon, R. Lindblad, E. M. Johansson, I. J. McPherson, H. Rensmo, J. M. Ball, M. M. Lee, and H. J. Snaith, “Electronic properties of meso-superstructured and planar organometal halide perovskite films: Charge trapping, photodoping, and carrier mobility”, *ACS Nano*, vol. 8, no. 7, pp. 7147–7155, 2014.
15. I. L. Ivanov, A. S. Steparuk, M. S. Bolyachkina, D. S. Tsvetkov, A. P. Safronov, and A. Y. Zuev, “Thermodynamics of formation of hybrid perovskite-type methylammonium lead halides”, *The Journal of Chemical Thermodynamics*, vol. 116, pp. 253–258, 2018.
16. A. Ciccioli and A. Latini, “Thermodynamics and the Intrinsic Stability of Lead Halide Perovskites $\text{CH}_3\text{NH}_3\text{PbX}_3$ ”, *The Journal of Physical Chemistry Letters*, vol. 9, no. 13, pp. 3756–3765, 2018.
17. E. J. Juarez-Perez, Z. Hawash, S. R. Raga, L. K. Ono, and Y. Qi, “Thermal degradation of $\text{CH}_3\text{NH}_3\text{PbI}_3$ perovskite into NH_3 and CH_3I gases observed by coupled thermogravimetry–mass spectrometry analysis”, *Energy & Environmental Science*, vol. 9, no. 11, pp. 3406–3410, 2016.

18. A. Dualeh, P. Gao, S. I. Seok, M. K. Nazeeruddin, and M. Grätzel, “Thermal behavior of methylammonium lead-trihalide perovskite photovoltaic light harvesters”, *Chemistry of Materials*, vol. 26, no. 21, pp. 6160–6164, 2014.
19. J. Yang, B. D. Siempelkamp, D. Liu, and T. L. Kelly, “Investigation of $\text{CH}_3\text{NH}_3\text{PbI}_3$ degradation rates and mechanisms in controlled humidity environments using in situ techniques”, *ACS Nano*, vol. 9, no. 2, pp. 1955–1963, 2015.
20. M. Shirayama, M. Kato, T. Miyadera, T. Sugita, T. Fujiseki, S. Hara, H. Kadowaki, D. Murata, M. Chikamatsu, and H. Fujiwara, “Degradation mechanism of $\text{CH}_3\text{NH}_3\text{PbI}_3$ perovskite materials upon exposure to humid air”, *Journal of Applied Physics*, vol. 119, no. 11, p. 115501, 2016.
21. N. Aristidou, I. Sanchez-Molina, T. Chotchuangchutchaval, M. Brown, L. Martinez, T. Rath, and S. A. Haque, “The Role of Oxygen in the Degradation of Methylammonium Lead Trihalide Perovskite Photoactive Layers”, *Angewandte Chemie International Edition*, vol. 54, no. 28, pp. 8208–8212, 2015.
22. D. Bryant, N. Aristidou, S. Pont, I. Sanchez-Molina, T. Chotchuangchutchaval, S. Wheeler, J. R. Durrant, and S. A. Haque, “Light and oxygen induced degradation limits the operational stability of methylammonium lead triiodide perovskite solar cells”, *Energy & Environmental Science*, vol. 9, no. 5, pp. 1655–1660, 2016.
23. S. W. Lee, S. Kim, S. Bae, K. Cho, T. Chung, L. E. Mundt, S. Lee, S. Park, H. Park, M. C. Schubert, S. W. Glunz, Y. Ko, Y. Jun, Y. Kang, H. S. Lee, and D. Kim, “UV Degradation and Recovery of Perovskite Solar Cells”, *Scientific Reports*, vol. 6, no. 38150, 2016.
24. A. Farooq, I. M. Hossain, S. Moghadamzadeh, J. A. Schwenzler, T. Abzieher, B. S. Richards, E. Klampaftis, and U. W. Paetzold, “Spectral Dependence of Degradation under Ultraviolet Light in Perovskite Solar Cells”, *ACS Applied Materials & Interfaces*, vol. 10, no. 26, pp. 21 985–21 990, 2018.
25. F. Corsini and G. Griffini, “Recent progress in encapsulation strategies to enhance the stability of organometal halide perovskite

- solar cells”, *Journal of Physics: Energy*, vol. 2, no. 3, p. 031002, 2020.
26. J. Wang, G. Jin, Q. Zhen, C. He, and Y. Duan, “Bulk Passivation and Interfacial Passivation for Perovskite Solar Cells: Which One is More Effective?” *Advanced Materials Interfaces*, vol. 8, no. 9, 2021.
27. C. A. Aranda, L. Calìo, and M. Salado, “Toward Commercialization of Stable Devices: An Overview on Encapsulation of Hybrid Organic-Inorganic Perovskite Solar Cells”, *Crystals*, vol. 11, no. 5, p. 519, 2021.
28. A. Jaffe, Y. Lin, and H. I. Karunadasa, “Halide Perovskites under Pressure: Accessing New Properties through Lattice Compression”, *ACS Energy Letters*, vol. 2, no. 7, pp. 1549–1555, 2017.
29. W. C. Lai, K. W. Lin, T. F. Guo, P. Chen, and Y. Y. Liao, “Perovskite-based solar cells with inorganic inverted hybrid planar heterojunction structure”, *AIP Advances*, vol. 8, no. 1, p. 15109, 2018.
30. D. Meggiolaro and F. De Angelis, “First-Principles Modeling of Defects in Lead Halide Perovskites: Best Practices and Open Issues”, *ACS Energy Letters*, vol. 3, no. 9, pp. 2206–2222, 2018.
31. D. Meggiolaro, S. G. Motti, E. Mosconi, A. J. Barker, J. Ball, C. Andrea Riccardo Perini, F. Deschler, A. Petrozza, and F. De Angelis, “Iodine chemistry determines the defect tolerance of lead-halide perovskites”, *Energy & Environmental Science*, vol. 11, no. 3, pp. 702–713, 2018.
32. A. Walsh, D. O. Scanlon, S. Chen, X. G. Gong, and S.-H. Wei, “Self-Regulation Mechanism for Charged Point Defects in Hybrid Halide Perovskites”, *Angewandte Chemie*, vol. 127, no. 6, pp. 1811–1814, 2015.
33. C. Eames, J. M. Frost, P. R. Barnes, B. C. O’Regan, A. Walsh, and M. S. Islam, “Ionic transport in hybrid lead iodide perovskite solar cells”, *Nature Communications*, vol. 6, no. 7497, 2015.
34. J. M. Azpiroz, E. Mosconi, J. Bisquert, and F. De Angelis, “Defect migration in methylammonium lead iodide and its role in perovskite solar cell operation”, *Energy & Environmental Science*, vol. 8, no. 7, pp. 2118–2127, 2015.

35. T. Zhang, C. Hu, and S. Yang, "Ion Migration: A "Double-Edged Sword" for Halide-Perovskite-Based Electronic Devices", *Small Methods*, vol. 4, no. 5, p. 1900552, 2020.
36. D. Meggiolaro, E. Mosconi, and F. De Angelis, "Formation of Surface Defects Dominates Ion Migration in Lead-Halide Perovskites", *ACS Energy Letters*, vol. 4, no. 3, pp. 779–785, 2019.
37. J. Haruyama, K. Sodeyama, L. Han, and Y. Tateyama, "First-principles study of ion diffusion in perovskite solar cell sensitizers", *Journal of the American Chemical Society*, vol. 137, no. 32, pp. 10 048–10 051, 2015.
38. A. Mattoni, A. Filippetti, and C. Caddeo, "Modeling hybrid perovskites by molecular dynamics", *Journal of Physics: Condensed Matter*, vol. 29, no. 4, p. 043001, 2016.
39. S. R. Balestra, J. M. Vicent-Luna, S. Calero, S. Tao, and J. A. Anta, "Efficient modelling of ion structure and dynamics in inorganic metal halide perovskites", *Journal of Materials Chemistry A*, vol. 8, no. 23, pp. 11 824–11 836, 2020.
40. A. Ruth, M. C. Brennan, S. Draguta, Y. V. Morozov, M. Zhukovskyi, B. Janko, P. Zapol, and M. Kuno, "Vacancy-Mediated Anion Photosegregation Kinetics in Mixed Halide Hybrid Perovskites: Coupled Kinetic Monte Carlo and Optical Measurements", *ACS Energy Letters*, vol. 3, no. 10, pp. 2321–2328, 2018.
41. J. W. Lee, S. G. Kim, J. M. Yang, Y. Yang, and N. G. Park, "Verification and mitigation of ion migration in perovskite solar cells", *APL Materials*, vol. 7, no. 4, p. 041111, 2019.
42. Y. Luo, P. Khoram, S. Brittman, Z. Zhu, B. Lai, S. P. Ong, E. C. Garnett, and D. P. Fenning, "Direct Observation of Halide Migration and its Effect on the Photoluminescence of Methylammonium Lead Bromide Perovskite Single Crystals", *Advanced Materials*, vol. 29, no. 43, p. 1703451, 2017.
43. Z. Huang, A. H. Proppe, H. Tan, M. I. Saidaminov, F. Tan, A. Mei, C.-S. Tan, M. Wei, Y. Hou, H. Han, S. O. Kelley, and E. H. Sargent, "Suppressed Ion Migration in Reduced-Dimensional Perovskites Improves Operating Stability", *ACS Energy Letters*, vol. 4, no. 7, pp. 1521–1527, 2019.

44. J. S. Yun, J. Seidel, J. Kim, A. Mahboubi Soufiani, S. Huang, J. Lau, N. Joong Jeon, S. Il Seok, M. A. Green, A. Ho-Baillie, J. S. Yun, J. Kim, A. M. Soufi ani, S. Huang, J. Lau, M. A. Green, A. Ho-Baillie, J. Seidel, N. J. Jeon, and S. I. Seok, "Critical Role of Grain Boundaries for Ion Migration in Formamidinium and Methylammonium Lead Halide Perovskite Solar Cells", *Advanced Energy Materials*, vol. 6, no. 13, p. 1600330, 2016.
45. T. Zhang, X. Meng, Y. Bai, S. Xiao, C. Hu, Y. Yang, H. Chen, and S. Yang, "Profiling the organic cation-dependent degradation of organolead halide perovskite solar cells", *Journal of Materials Chemistry A*, vol. 5, no. 3, pp. 1103–1111, 2017.
46. J. P. Correa-Baena, Y. Luo, T. M. Brenner, J. Snaider, S. Sun, X. Li, M. A. Jensen, N. T. P. Hartono, L. Nienhaus, S. Wiegold, J. R. Poindexter, S. Wang, Y. S. Meng, T. Wang, B. Lai, M. V. Holt, Z. Cai, M. G. Bawendi, L. Huang, T. Buonassisi, and D. P. Fenning, "Homogenized halides and alkali cation segregation in alloyed organic-inorganic perovskites", *Science*, vol. 363, no. 6427, pp. 627–631, 2019.
47. S. P. Harvey, Z. Li, J. A. Christians, K. Zhu, J. M. Luther, and J. J. Berry, "Probing Perovskite Inhomogeneity beyond the Surface: TOF-SIMS Analysis of Halide Perovskite Photovoltaic Devices", *ACS Applied Materials & Interfaces*, vol. 10, no. 34, pp. 28 541–28 552, 2018.
48. B. Yang, C. C. Brown, J. Huang, L. Collins, X. Sang, R. R. Unocic, S. Jesse, S. V. Kalinin, A. Belianinov, J. Jakowski, D. B. Geohegan, B. G. Sumpter, K. Xiao, and O. S. Ovchinnikova, "Enhancing Ion Migration in Grain Boundaries of Hybrid Organic-Inorganic Perovskites by Chlorine", *Advanced Functional Materials*, vol. 27, no. 26, p. 1700749, 2017.
49. J. Xing, Q. Wang, Q. Dong, Y. Yuan, Y. Fang, and J. Huang, "Ultrafast ion migration in hybrid perovskite polycrystalline thin films under light and suppression in single crystals", *Physical Chemistry Chemical Physics*, vol. 18, no. 44, pp. 30 484–30 490, 2016.
50. M. Bag, L. A. Renna, R. Y. Adhikari, S. Karak, F. Liu, P. M. Lahti, T. P. Russell, M. T. Tuominen, and D. Venkataraman,

- “Kinetics of Ion Transport in Perovskite Active Layers and Its Implications for Active Layer Stability”, *Journal of the American Chemical Society*, vol. 137, no. 40, pp. 13 130–13 137, 2015.
51. M. H. Futscher, M. K. Gangishetty, D. N. Congreve, and B. Ehrler, “Quantifying mobile ions and electronic defects in perovskite-based devices with temperature-dependent capacitance measurements: Frequency vs time domain”, *Journal of Chemical Physics*, vol. 152, no. 4, p. 44202, 2020.
 52. E. von Hauff, “Impedance Spectroscopy for Emerging Photovoltaics”, *The Journal of Physical Chemistry C*, vol. 123, no. 18, pp. 11 329–11 346, 2019.
 53. S. T. Birkhold, J. T. Pecht, H. Liu, R. Giridharagopal, G. E. Eperon, L. Schmidt-Mende, X. Li, and D. S. Ginger, “Interplay of Mobile Ions and Injected Carriers Creates Recombination Centers in Metal Halide Perovskites under Bias”, *ACS Energy Letters*, vol. 3, no. 6, pp. 1279–1286, 2018.
 54. A. Guerrero, G. Garcia-Belmonte, I. Mora-Sero, J. Bisquert, Y. Soo Kang, T. Jesper Jacobsson, J.-P. Correa-Baena, and A. Hagfeldt, “Properties of Contact and Bulk Impedances in Hybrid Lead Halide Perovskite Solar Cells Including Inductive Loop Elements”, *The Journal of Physical Chemistry C*, vol. 120, no. 15, pp. 8023–8032, 2016.
 55. H. Wang, A. Guerrero, A. Bou, A. M. Al-Mayouf, and J. Bisquert, “Kinetic and material properties of interfaces governing slow response and long timescale phenomena in perovskite solar cells”, *Energy & Environmental Science*, vol. 12, no. 7, pp. 2054–2079, 2019.
 56. L. McGovern, M. H. Futscher, L. A. Muscarella, and B. Ehrler, “Understanding the Stability of MAPbI₃ versus MAPbI₃: Suppression of Methylammonium Migration and Reduction of Halide Migration”, *Journal of Physical Chemistry Letters*, vol. 11, no. 17, pp. 7127–7132, 2020.
 57. J. A. Christians, P. A. M. Herrera, and P. V. Kamat, “Transformation of the Excited State and Photovoltaic Efficiency of CH₃NH₃PbI₃ Perovskite upon Controlled Exposure to Humidified

- Air”, *Journal of the American Chemical Society*, vol. 137, no. 4, pp. 1530–1538, 2015.
58. Y.-H. Kye, C.-J. Yu, U.-G. Jong, Y. Chen, and A. Walsh, “Critical Role of Water in Defect Aggregation and Chemical Degradation of Perovskite Solar Cells”, *The Journal of Physical Chemistry Letters*, vol. 9, no. 9, pp. 2196–2201, 2018.
59. A. Marronnier, H. Lee, H. Lee, M. Kim, C. Eypert, J. P. Gaston, G. Roma, D. Tondelier, B. Geffroy, and Y. Bonnassieux, “Electrical and optical degradation study of methylammonium-based perovskite materials under ambient conditions”, *Solar Energy Materials & Solar Cells*, vol. 178, pp. 179–185, 2018.
60. H. Yuan, E. Debroye, K. Janssen, H. Naiki, C. Steuwe, G. Lu, M. Moris, E. Orgiu, H. Uji-i, F. D. Schryver, P. Samorì, J. Hofkens, and M. Roeffaers, “Degradation of Methylammonium Lead Iodide Perovskite Structures through Light and Electron Beam Driven Ion Migration”, *Journal of Physical Chemistry Letters*, vol. 7, no. 3, pp. 561–566, 2016.
61. Y. Xiang, F. Zhang, J. He, J. Lian, P. Zeng, J. Song, and J. Qu, “Light-current-induced acceleration of degradation of methylammonium lead iodide perovskite solar cells”, *Journal of Power Sources*, vol. 384, pp. 303–311, 2018.
62. N. H. Nickel, F. Lang, V. V. Brus, O. Shargaieva, and J. Rappich, “Unraveling the Light-Induced Degradation Mechanisms of $\text{CH}_3\text{NH}_3\text{PbI}_3$ Perovskite Films”, *Advanced Electronic Materials*, vol. 3, no. 12, p. 1700158, 2017.
63. B. Brunetti, C. Cavallo, A. Ciccioi, G. Gigli, and A. Latini, “On the Thermal and Thermodynamic (In)Stability of Methylammonium Lead Halide Perovskites”, *Scientific Reports*, vol. 6, no. 31896, 2016.
64. A. Alberti, I. Deretzis, G. Mannino, E. Smecca, S. Sanzaro, Y. Numata, T. Miyasaka, and A. L. Magna, “Revealing a Discontinuity in the Degradation Behavior of $\text{CH}_3\text{NH}_3\text{PbI}_3$ during Thermal Operation”, *Journal of Physical Chemistry C*, vol. 121, no. 25, pp. 13 577–13 585, 2017.

-
65. V. Nandal and P. R. Nair, "Predictive Modeling of Ion Migration Induced Degradation in Perovskite Solar Cells", *ACS Nano*, vol. 11, no. 11, pp. 11 505–11 512, 2017.
66. S. Pont, D. Bryant, C.-T. Lin, N. Aristidou, S. Wheeler, X. Ma, R. Godin, S. A. Haque, and J. R. Durrant, "Tuning $\text{CH}_3\text{NH}_3\text{Pb}(\text{I}_{1-x}\text{Br}_x)_3$ perovskite oxygen stability in thin films and solar cells", *Journal of Materials Chemistry A*, vol. 5, no. 20, pp. 9553–9560, 2017.
67. E. J. Juarez-Perez, L. K. Ono, M. Maeda, Y. Jiang, Z. Hawash, and Y. Qi, "Photodecomposition and thermal decomposition in methylammonium halide lead perovskites and inferred design principles to increase photovoltaic device stability", *Journal of Materials Chemistry A*, vol. 6, no. 20, pp. 9604–9612, 2018.
68. A. Aziz, N. Aristidou, X. Bu, R. J. E. Westbrook, S. A. Haque, and M. S. Islam, "Understanding the Enhanced Stability of Bromide Substitution in Lead Iodide Perovskites", *Chemistry of Materials*, vol. 32, no. 1, pp. 400–409, 2019.
69. S. J. Yoon, M. Kuno, and P. V. Kamat, "Shift Happens. How Halide Ion Defects Influence Photoinduced Segregation in Mixed Halide Perovskites", *ACS Energy Letters*, vol. 2, no. 7, pp. 1507–1514, 2017.
70. S. J. Yoon, K. G. Stamplecoskie, and P. V. Kamat, "How Lead Halide Complex Chemistry Dictates the Composition of Mixed Halide Perovskites", *Journal of Physical Chemistry Letters*, vol. 7, no. 7, pp. 1368–1373, 2016.
71. M. Szafranski and A. Katrusiak, "Mechanism of Pressure-Induced Phase Transitions, Amorphization, and Absorption-Edge Shift in Photovoltaic Methylammonium Lead Iodide", *Journal of Physical Chemistry Letters*, vol. 7, no. 17, pp. 3458–3466, 2016.
72. A. Jaffe, Y. Lin, C. M. Beavers, J. Voss, W. L. Mao, and H. I. Karunadasa, "High-Pressure Single-Crystal Structures of 3D Lead-Halide Hybrid Perovskites and Pressure Effects on their Electronic and Optical Properties", *ACS Central Science*, vol. 2, no. 4, pp. 201–209, 2016.

73. C. Lin, S. Li, W. Zhang, C. Shao, and Z. Yang, “Effect of Bromine Substitution on the Ion Migration and Optical Absorption in MAPbI₃ Perovskite Solar Cells: The First-Principles Study”, *ACS Applied Energy Materials*, vol. 1, no. 3, pp. 1374–1380, 2018.
74. J. H. Noh, S. H. Im, J. H. Heo, T. N. Mandal, and S. I. Seok, “Chemical Management for Colorful, Efficient, and Stable Inorganic–Organic Hybrid Nanostructured Solar Cells”, *Nano Letters*, vol. 13, no. 4, pp. 1764–1769, 2013.
75. L. Atourki, E. Vega, B. Marí, M. Mollar, H. Ait Ahsaine, K. Bouabid, and A. Ihlal, “Role of the chemical substitution on the structural and luminescence properties of the mixed halide perovskite thin MAPbI_{3-x}Br_x (0 ≤ x ≤ 1) films”, *Applied Surface Science*, vol. 371, pp. 112–117, 2016.
76. M. Futscher, J. Lee, L. McGovern, L. Muscarella, T. Wang, M. Haider, A. Fakharuddin, L. Schmidt-Mende, and B. Ehrler, “Quantification of ion migration in CH₃NH₃PbI₃ perovskite solar cells by transient capacitance measurements”, *Materials Horizons*, vol. 6, no. 7, 2019.
77. A. Oranskaia, J. Yin, O. M. Bakr, J.-L. Brédas, O. F. Mohammed, and S. Arabia, “Halogen Migration in Hybrid Perovskites: The Organic Cation Matters”, *Journal of Physical Chemistry Letters*, vol. 9, p. 59, 2018.
78. S. Feldmann, S. Macpherson, S. P. Senanayak, M. Abdi-Jalebi, J. P. H. Rivett, G. Nan, G. D. Tainter, T. A. S. Doherty, K. Frohna, E. Ringe, R. H. Friend, H. Sirringhaus, M. Saliba, D. Beljonne, S. D. Stranks, and F. Deschler, “Photodoping through local charge carrier accumulation in alloyed hybrid perovskites for highly efficient luminescence”, *Nature Photonics*, vol. 14, no. 2, pp. 123–128, 2019.
79. X. Hu, X.-F. Jiang, X. Xing, L. Nian, X. Liu, R. Huang, K. Wang, H.-L. Yip, and G. Zhou, “Wide-Bandgap Perovskite Solar Cells With Large Open-Circuit Voltage of 1653 mV Through Interfacial Engineering”, *Solar RRL*, vol. 2, no. 8, p. 1800083, 2018.
80. A. Musiienko, P. Moravec, R. Grill, P. Praus, I. Vasylenko, J. Pekarek, J. Tisdale, K. Ridzonova, E. Belas, L. Landová, B. Hu,

- E. Lukosi, and M. Ahmadi, “Deep levels, charge transport and mixed conductivity in organometallic halide perovskites”, *Energy & Environmental Science*, vol. 12, no. 4, pp. 1413–1425, 2019.
81. M. Ahmadi, E. S. Muckley, I. N. Ivanov, M. Lorenz, X. Li, O. Ovchinnikova, E. D. Lukosi, J. T. Tisdale, E. Blount, I. I. Kravchenko, S. V. Kalinin, B. Hu, and L. Collins, “Environmental Gating and Galvanic Effects in Single Crystals of Organic–Inorganic Halide Perovskites”, *ACS Applied Materials & Interfaces*, vol. 11, no. 16, pp. 14 722–14 733, 2019.
82. F. El-Mellouhi, A. Marzouk, E. T. Bentría, S. N. Rashkeev, S. Kais, and F. H. Alharbi, “Hydrogen Bonding and Stability of Hybrid Organic–Inorganic Perovskites”, *ChemSusChem*, vol. 9, no. 18, pp. 2648–2655, 2016.
83. T. Glaser, C. Müller, M. Sendner, C. Krekeler, O. E. Semonin, T. D. Hull, O. Yaffe, J. S. Owen, W. Kowalsky, A. Pucci, and R. Lovrinčić, “Infrared Spectroscopic Study of Vibrational Modes in Methylammonium Lead Halide Perovskites”, *Journal of Physical Chemistry Letters*, vol. 6, no. 15, pp. 2913–2918, 2015.
84. A. M. A. Leguy, A. R. Goñi, J. M. Frost, J. Skelton, F. Brivio, X. Rodríguez-Martínez, O. J. Weber, A. Pallipurath, M. I. Alonso, M. Campoy-Quiles, M. T. Weller, J. Nelson, A. Walsh, and P. R. F. Barnes, “Dynamic disorder, phonon lifetimes, and the assignment of modes to the vibrational spectra of methylammonium lead halide perovskites”, *Physical Chemistry Chemical Physics*, vol. 18, no. 39, pp. 27 051–27 066, 2016.
85. K. L. Svane, A. C. Forse, C. P. Grey, G. Kieslich, A. K. Cheetham, A. Walsh, and K. T. Butler, “How Strong Is the Hydrogen Bond in Hybrid Perovskites?” *Journal of Physical Chemistry Letters*, vol. 8, no. 24, pp. 6154–6159, 2017.
86. S. Meloni, T. Moehl, W. Tress, M. Franckeviius, M. Saliba, Y. H. Lee, P. Gao, M. K. Nazeeruddin, S. M. Zakeeruddin, U. Rothlisberger, and M. Graetzel, “Ionic polarization-induced current-voltage hysteresis in $\text{CH}_3\text{NH}_3\text{PbX}_3$ perovskite solar cells”, *Nature Communications*, vol. 7, no. 10334, 2016.
87. M. Ledinský, P. Löper, B. Niesen, J. Holovský, S.-J. Moon, J.-H. Yum, S. D. Wolf, A. Fejfar, and C. Ballif, “Raman Spectroscopy

- of Organic-Inorganic Halide Perovskites”, *Journal of Physical Chemistry Letters*, vol. 6, no. 3, pp. 401–406, 2015.
88. L. Bertoluzzi, C. C. Boyd, N. Rolston, J. Xu, R. Prasanna, B. C. O’Regan, and M. D. McGehee, “Mobile Ion Concentration Measurement and Open-Access Band Diagram Simulation Platform for Halide Perovskite Solar Cells”, *Joule*, vol. 4, no. 1, pp. 109–127, 2020.
89. S. A. Weber, I. M. Hermes, S. H. Turren-Cruz, C. Gort, V. W. Bergmann, L. Gilson, A. Hagfeldt, M. Graetzel, W. Tress, and R. Berger, “How the formation of interfacial charge causes hysteresis in perovskite solar cells”, *Energy & Environmental Science*, vol. 11, no. 9, pp. 2404–2413, 2018.
90. S. Reichert, J. Flemming, Q. An, Y. Vaynzof, J.-F. Pietschmann, and C. Deibel, “Ionic-Defect Distribution Revealed by Improved Evaluation of Deep-Level Transient Spectroscopy on Perovskite Solar Cells”, *Physical Review Applied*, vol. 10, p. 34018, 2020.
91. J. Caram, M. García-Batlle, O. Almora, R. D. Arce, A. Guerrero, and G. Garcia-Belmonte, “Direct observation of surface polarization at hybrid perovskite/Au interfaces by dark transient experiments”, *Applied Physics Letters*, vol. 116, no. 18, p. 183503, 2020.
92. D. Barboni and R. A. D. Souza, “The thermodynamics and kinetics of iodine vacancies in the hybrid perovskite methylammonium lead iodide”, *Energy & Environmental Science*, vol. 11, no. 11, pp. 3266–3274, 2018.
93. P. Calado, A. M. Telford, D. Bryant, X. Li, J. Nelson, B. C. O’Regan, and P. R. Barnes, “Evidence for ion migration in hybrid perovskite solar cells with minimal hysteresis”, *Nature Communications*, vol. 7, no. 13831, 2016.
94. P. Schulz, E. Edri, S. Kirmayer, G. Hodes, D. Cahen, and A. Kahn, “Interface energetics in organo-metal halide perovskite-based photovoltaic cells”, *Energy & Environmental Science*, vol. 7, no. 4, pp. 1377–1381, 2014.
95. X. Yin, Z. Yao, Q. Luo, X. Dai, Y. Zhou, Y. Zhang, Y. Zhou, S. Luo, J. Li, N. Wang, and H. Lin, “High Efficiency Inverted Planar Perovskite Solar Cells with Solution-Processed NiO_x Hole Contact”,

-
- ACS Applied Materials & Interfaces*, vol. 9, no. 3, pp. 2439–2448, 2017.
96. I. Collins, P. Andrews, and A. Law, “Unoccupied electronic states of single-crystal graphite by angle-resolved ultraviolet inverse photoemission”, *Physical Review B - Condensed Matter and Materials Physics*, vol. 38, no. 18, pp. 13 348–13 354, 1988.
97. I. Zarazua, G. Han, P. P. Boix, S. Mhaisalkar, F. Fabregat-Santiago, I. Mora-Seró, J. Bisquert, and G. Garcia-Belmonte, “Surface Recombination and Collection Efficiency in Perovskite Solar Cells from Impedance Analysis”, *The Journal of Physical Chemistry Letters*, vol. 7, no. 24, pp. 5105–5113, 2016.
98. T. Kirchartz, W. Gong, S. A. Hawks, T. Agostinelli, R. C. MacKenzie, Y. Yang, and J. Nelson, “Sensitivity of the Mott-Schottky Analysis in Organic Solar Cells”, *Journal of Physical Chemistry C*, vol. 116, no. 14, pp. 7672–7680, 2012.
99. J. N. Wilson, J. M. Frost, S. K. Wallace, and A. Walsh, “Dielectric and ferroic properties of metal halide perovskites”, *APL Materials*, vol. 7, no. 1, p. 010901, 2019.
100. S. Govinda, B. P. Kore, M. Bokdam, P. Mahale, A. Kumar, S. Pal, B. Bhattacharyya, J. Lahnsteiner, G. Kresse, C. Franchini, A. Pandey, and D. D. Sarma, “Behavior of Methylammonium Dipoles in MAPbX₃ (X = Br and I)”, *The Journal of Physical Chemistry Letters*, vol. 8, no. 17, p. 4113, 2017.
101. N. Onoda-Yamamuro, T. Matsuo, and H. Suga, “Dielectric study of CH₃NH₃PbX₃ (X = Cl, Br, I)”, *Journal of Physics and Chemistry of Solids*, vol. 53, no. 7, pp. 935–939, 1992.
102. K. Gesi, “Effect of hydrostatic pressure on the structural phase transitions in CH₃NH₃PbX₃ (X = Cl, Br, I)”, *Ferroelectrics*, vol. 203, no. 1-4, pp. 249–268, 1997.
103. M. Masaki, H. Maki, H. Akifumi, and S. Ikuo, “Dielectric Studies on CH₃NH₃PbX₃ (X = Cl and Br) Single Crystals”, *Journal of the Physical Society of Japan*, vol. 66, no. 5, pp. 1508–1511, 1997.
104. L. McGovern, G. Grimaldi, M. H. Futscher, E. M. Hutter, L. A. Muscarella, M. C. Schmidt, and B. Ehrler, “Reduced Barrier for

- Ion Migration in Mixed-Halide Perovskites”, *ACS Applied Energy Materials*, vol. 4, no. 12, pp. 13 431–13 437, 2021.
105. E. T. Hoke, D. J. Slotcavage, E. R. Dohner, A. R. Bowring, H. I. Karunadasa, and M. D. McGehee, “Reversible photo-induced trap formation in mixed-halide hybrid perovskites for photovoltaics”, *Chemical Science*, vol. 6, no. 1, pp. 613–617, 2015.
106. U. B. Cappel, S. Svanström, V. Lanzilotto, F. O. L. Johansson, K. Aitola, B. Philippe, E. Giangrisostomi, R. Ovsyannikov, T. Leitner, A. Föhlich, S. Svensson, N. Mårtensson, G. Boschloo, A. Lindblad, and H. Rensmo, “Partially Reversible Photoinduced Chemical Changes in a Mixed-Ion Perovskite Material for Solar Cells”, *ACS Applied Materials & Interfaces*, vol. 9, no. 40, pp. 34 970–34 978, 2017.
107. A. Gomez, S. Sanchez, M. Campoy-Quiles, and A. Abate, “Topological distribution of reversible and non-reversible degradation in perovskite solar cells”, *Nano Energy*, vol. 45, pp. 94–100, 2018.
108. K. Domanski, B. Roose, T. Matsui, M. Saliba, S. H. Turren-Cruz, J. P. Correa-Baena, C. R. Carmona, G. Richardson, J. M. Foster, F. De Angelis, J. M. Ball, A. Petrozza, N. Mine, M. K. Nazeeruddin, W. Tress, M. Grätzel, U. Steiner, A. Hagfeldt, and A. Abate, “Migration of cations induces reversible performance losses over day/night cycling in perovskite solar cells”, *Energy & Environmental Science*, vol. 10, no. 2, pp. 604–613, 2017.
109. S. Draguta, O. Sharia, S. J. Yoon, M. C. Brennan, Y. V. Morozov, J. M. Manser, P. V. Kamat, W. F. Schneider, and M. Kuno, “Rationalizing the light-induced phase separation of mixed halide organic-inorganic perovskites”, *Nature Communications*, vol. 8, no. 200, 2017.
110. A. J. Barker, A. Sadhanala, F. Deschler, M. Gandini, S. P. Senanayak, P. M. Pearce, E. Mosconi, A. J. Pearson, Y. Wu, A. Ram Srimath Kandada, T. Leijtens, F. De Angelis, S. E. Dutton, A. Petrozza, and R. H. Friend, “Defect-Assisted Photoinduced Halide Segregation in Mixed-Halide Perovskite Thin Films”, *ACS Energy Letters*, vol. 2, no. 6, pp. 1416–1424, 2017.
111. R. A. Belisle, K. A. Bush, L. Bertoluzzi, A. Gold-Parker, M. F. Toney, and M. D. McGehee, “Impact of Surfaces on Photoinduced

- Halide Segregation in Mixed-Halide Perovskites”, *ACS Energy Letters*, vol. 3, no. 11, pp. 2694–2700, 2018.
112. T. Elmelund, B. Seger, M. Kuno, and P. V. Kamat, “How Interplay between Photo and Thermal Activation Dictates Halide Ion Segregation in Mixed Halide Perovskites”, *ACS Energy Letters*, vol. 5, no. 1, pp. 56–63, 2019.
 113. R. A. Scheidt and P. V. Kamat, “Temperature-driven anion migration in gradient halide perovskites”, *Journal of Chemical Physics*, vol. 151, no. 13, p. 134703, 2019.
 114. E. Hutter, L. Muscarella, F. Wittmann, J. Versluis, L. McGovern, H. Bakker, Y.-W. Woo, Y.-K. Jung, A. Walsh, and B. Ehrler, “Thermodynamic Stabilization of Mixed-Halide Perovskites against Phase Segregation”, *Cell Reports Physical Science*, vol. 1, no. 8, 2020.
 115. L. Muscarella, E. Hutter, F. Wittmann, Y. Woo, Y.-K. Jung, L. McGovern, J. Versluis, A. Walsh, H. Bakker, and B. Ehrler, “Lattice Compression Increases the Activation Barrier for Phase Segregation in Mixed-Halide Perovskites”, *ACS Energy Letters*, vol. 5, no. 10, 2020.
 116. R. García-Rodríguez, D. Ferdani, S. Pering, P. J. Baker, and P. J. Cameron, “Influence of bromide content on iodide migration in inverted $\text{MAPb}(\text{I}_{1-x}\text{Br}_x)_3$ perovskite solar cells”, *Journal of Materials Chemistry A*, vol. 7, no. 39, pp. 22 604–22 614, 2019.
 117. G. Y. Kim, A. Senocrate, Y. R. Wang, D. Moia, and J. Maier, “Photo-Effect on Ion Transport in Mixed Cation and Halide Perovskites and Implications for Photo-Demixing**”, *Angewandte Chemie International Edition*, vol. 60, no. 2, pp. 820–826, 2021.
 118. T. Heiser and E. Weber, “Transient ion-drift-induced capacitance signals in semiconductors”, *Physical Review B - Condensed Matter and Materials Physics*, vol. 58, no. 7, pp. 3893–3903, 1998.
 119. T. Leijtens, E. T. Hoke, G. Grancini, D. J. Slotcavage, G. E. Eperon, J. M. Ball, M. De Bastiani, A. R. Bowring, N. Martino, K. Wojciechowski, M. D. McGehee, H. J. Snaith, and A. Petrozza, “Mapping Electric Field-Induced Switchable Poling and Structural Degradation in Hybrid Lead Halide Perovskite Thin Films”, *Advanced Energy Materials*, vol. 5, no. 20, p. 1500962, 2015.

120. P. Vashishtha and J. E. Halpert, "Field-Driven Ion Migration and Color Instability in Red-Emitting Mixed Halide Perovskite Nanocrystal Light-Emitting Diodes", *Chemistry of Materials*, vol. 29, no. 14, pp. 5965–5973, 2017.
121. Q. Wang, Y. Shao, H. Xie, L. Lyu, X. Liu, Y. Gao, and J. Huang, "Qualifying composition dependent p and n self-doping in $\text{CH}_3\text{NH}_3\text{PbI}_3$ ", *Applied Physics Letters*, vol. 105, no. 16, p. 163508, 2014.
122. T. Shi, W. J. Yin, F. Hong, K. Zhu, and Y. Yan, "Unipolar self-doping behavior in perovskite $\text{CH}_3\text{NH}_3\text{PbI}_3$ ", *Applied Physics Letters*, vol. 106, no. 10, p. 103902, 2015.
123. K. Miyano, N. Tripathi, M. Yanagida, and Y. Shirai, "Lead Halide Perovskite Photovoltaic as a Model p-i-n Diode", *Accounts of Chemical Research*, vol. 49, no. 2, pp. 303–310, 2016.
124. L. McGovern, I. Koschany, G. Grimaldi, L. A. Muscarella, and B. Ehrler, "Grain Size Influences Activation Energy and Migration Pathways in MAPbI_3 Perovskite Solar Cells", *Journal of Physical Chemistry Letters*, vol. 12, pp. 2423–2428, 2021.
125. Y. Zhou, I. Poli, D. Meggiolaro, F. De Angelis, and A. Petrozza, "Defect activity in metal halide perovskites with wide and narrow bandgap", *Nature Reviews Materials*, vol. 6, p. 986–1002, 2021.
126. W. Rehman, R. L. Milot, G. E. Eperon, C. Wehrenfennig, J. L. Boland, H. J. Snaith, M. B. Johnston, and L. M. Herz, "Charge-Carrier Dynamics and Mobilities in Formamidinium Lead Mixed-Halide Perovskites", *Advanced Materials*, vol. 27, no. 48, pp. 7938–7944, 2015.
127. Y. Zhao, P. Miao, J. Elia, H. Hu, X. Wang, T. Heumueller, Y. Hou, G. J. Matt, A. Osvet, Y.-T. Chen, M. Tarragó, D. de Ligny, T. Przybilla, P. Denninger, J. Will, J. Zhang, X. Tang, N. Li, C. He, A. Pan, A. J. Meixner, E. Spiecker, D. Zhang, and C. J. Brabec, "Strain-activated light-induced halide segregation in mixed-halide perovskite solids", *Nature Communications*, vol. 11, no. 6328, 2020.
128. A. J. Knight, A. D. Wright, J. B. Patel, D. P. McMeekin, H. J. Snaith, M. B. Johnston, and L. M. Herz, "Electronic Traps and

- Phase Segregation in Lead Mixed-Halide Perovskite”, *ACS Energy Letters*, vol. 4, no. 1, pp. 75–84, 2018.
129. I. L. Braly, R. J. Stoddard, A. Rajagopal, A. R. Uhl, J. K. Katahara, A. K.-Y. Jen, and H. W. Hillhouse, “Current-Induced Phase Segregation in Mixed Halide Hybrid Perovskites and its Impact on Two-Terminal Tandem Solar Cell Design”, *ACS Energy Letters*, vol. 2, no. 8, pp. 1841–1847, 2017.
 130. S. Chen, X. Wen, R. Sheng, S. Huang, X. Deng, M. A. Green, and A. Ho-Baillie, “Mobile Ion Induced Slow Carrier Dynamics in Organic–Inorganic Perovskite $\text{CH}_3\text{NH}_3\text{PbBr}_3$ ”, *ACS Applied Materials & Interfaces*, vol. 8, no. 8, pp. 5351–5357, 2016.
 131. Y. C. Zhao, W. K. Zhou, X. Zhou, K. H. Liu, D. P. Yu, and Q. Zhao, “Quantification of light-enhanced ionic transport in lead iodide perovskite thin films and its solar cell applications”, *Light: Science and Applications*, vol. 6, no. 5, p. e16243, 2017.
 132. A. Senocrate, E. Kotomin, and J. Maier, “On the Way to Optoionics”, *Helvetica Chimica Acta*, vol. 103, no. 7, p. e2000073, 2020.
 133. C. G. Bischak, C. L. Hetherington, H. Wu, S. Aloni, D. Frank Ogle-tree, D. T. Limmer, and N. S. Ginsberg, “Origin of Reversible Photoinduced Phase Separation in Hybrid Perovskites”, *Nano Letters*, vol. 17, no. 2, pp. 1028–1033, 2017.
 134. C. G. Bischak, A. B. Wong, E. Lin, D. T. Limmer, P. Yang, and N. S. Ginsberg, “Tunable Polaron Distortions Control the Extent of Halide Demixing in Lead Halide Perovskites”, *The Journal of Physical Chemistry Letters*, vol. 9, no. 14, pp. 3998–4005, 2018.
 135. Z. Li, C. Xiao, Y. Yang, S. P. Harvey, D. H. Kim, J. A. Christians, M. Yang, P. Schulz, S. U. Nanayakkara, C.-S. Jiang, J. M. Luther, J. J. Berry, M. C. Beard, M. M. Al-Jassim, and K. Zhu, “Extrinsic ion migration in perovskite solar cells”, *Energy & Environmental Science*, vol. 10, no. 5, pp. 1234–1242, 2017.
 136. J. T. DuBose and P. V. Kamat, “ TiO_2 -Assisted Halide Ion Segregation in Mixed Halide Perovskite Films”, *Journal of the American Chemical Society*, vol. 142, no. 11, pp. 5362–5370, 2020.

137. S. Ravishankar, T. Unold, and T. Kirchartz, "Comment on "Resolving spatial and energetic distributions of trap states in metal halide perovskite solar cells"", *Science*, vol. 371, no. 6532, 2021.
138. X. Chen, Y. Shirai, M. Yanagida, and K. Miyano, "Effect of light and voltage on electrochemical impedance spectroscopy of perovskite solar cells: An empirical approach based on modified Randles Circuit", *Journal of Physical Chemistry C*, vol. 123, no. 7, pp. 3968–3978, 2019.
139. S. M. Abdulrahim, Z. Ahmad, J. Bahadra, and N. J. Al-Thani, "Electrochemical Impedance Spectroscopy Analysis of Hole Transporting Material Free Mesoporous and Planar Perovskite Solar Cells", *Nanomaterials*, vol. 10, no. 9, p. 1635, 2020.
140. C. Park, H. Ko, D. H. Sin, K. C. Song, and K. Cho, "Organometal Halide Perovskite Solar Cells with Improved Thermal Stability via Grain Boundary Passivation Using a Molecular Additive", *Advanced Functional Materials*, vol. 27, no. 42, p. 1703546, 2017.
141. J. Idígoras, F. J. Aparicio, L. Contreras-Bernal, S. Ramos-Terrón, M. Alcaire, J. R. Sánchez-Valencia, A. Borrás, Á. Barranco, and J. A. Anta, "Enhancing Moisture and Water Resistance in Perovskite Solar Cells by Encapsulation with Ultrathin Plasma Polymers", *ACS Applied Materials & Interfaces*, vol. 10, no. 14, pp. 11 587–11 594, 2018.
142. R. Cheacharoen, C. C. Boyd, G. F. Burkhard, T. Leijtens, J. A. Raiford, K. A. Bush, S. F. Bent, and M. D. McGehee, "Encapsulating perovskite solar cells to withstand damp heat and thermal cycling", *Sustainable Energy & Fuels*, vol. 2, no. 11, pp. 2398–2406, 2018.
143. S. Ma, Y. Bai, H. Wang, H. Zai, J. Wu, L. Li, S. Xiang, N. Liu, L. Liu, C. Zhu, G. Liu, X. Niu, H. Chen, H. Zhou, Y. Li, and Q. Chen, "1000 h Operational Lifetime Perovskite Solar Cells by Ambient Melting Encapsulation", *Advanced Energy Materials*, vol. 10, no. 9, p. 1902472, 2020.
144. F. Brivio, A. B. Walker, and A. Walsh, "Structural and electronic properties of hybrid perovskites for high-efficiency thin-film photovoltaics from first-principles", *APL Materials*, vol. 1, no. 4, p. 042111, 2013.

145. M. V. Khenkin, K. M. Anoop, E. A. Katz, and I. Visoly-Fisher, "Bias-dependent degradation of various solar cells: Lessons for stability of perovskite photovoltaics", *Energy & Environmental Science*, vol. 12, no. 2, pp. 550–558, 2019.
146. S. Bae, S. Kim, S. W. Lee, K. J. Cho, S. Park, S. Lee, Y. Kang, H. S. Lee, and D. Kim, "Electric-Field-Induced Degradation of Methylammonium Lead Iodide Perovskite Solar Cells", *Journal of Physical Chemistry Letters*, vol. 7, no. 16, pp. 3091–3096, 2016.
147. J. S. Yun, A. Ho-Baillie, S. Huang, S. H. Woo, Y. Heo, J. Seidel, F. Huang, Y. B. Cheng, and M. A. Green, "Benefit of grain boundaries in organic-inorganic halide planar perovskite solar cells", *Journal of Physical Chemistry Letters*, vol. 6, no. 5, pp. 875–880, 2015.
148. Y. Shao, Y. Fang, T. Li, Q. Wang, Q. Dong, Y. Deng, Y. Yuan, H. Wei, M. Wang, A. Gruverman, J. Shield, and J. Huang, "Grain boundary dominated ion migration in polycrystalline organic-inorganic halide perovskite films", *Energy & Environmental Science*, vol. 9, no. 5, pp. 1752–1759, 2016.
149. N. Phung, A. Al-Ashouri, S. Meloni, A. Mattoni, S. Albrecht, E. L. Unger, A. Merdasa, and A. Abate, "The Role of Grain Boundaries on Ionic Defect Migration in Metal Halide Perovskites", *Advanced Energy Materials*, vol. 10, no. 20, p. 1903735, 2020.
150. J. P. Correa-Baena, M. Anaya, G. Lozano, W. Tress, K. Domanski, M. Saliba, T. Matsui, T. J. Jacobsson, M. E. Calvo, A. Abate, M. Grätzel, H. Míguez, and A. Hagfeldt, "Unbroken Perovskite: Interplay of Morphology, Electro-optical Properties, and Ionic Movement", *Advanced Materials*, vol. 28, no. 25, pp. 5031–5037, 2016.
151. A. Mahapatra, N. Parikh, H. Kumari, M. K. Pandey, M. Kumar, D. Prochowicz, A. Kalam, M. M. Tavakoli, and P. Yadav, "Reducing ion migration in methylammonium lead tri-bromide single crystal via lead sulfate passivation", *Journal of Applied Physics*, vol. 127, no. 18, p. 185501, 2020.
152. G. W. P. Adhyaksa, S. Brittman, H. Āboliņš, A. Lof, X. Li, J. D. Keelor, Y. Luo, T. Duevski, R. M. A. Heeren, S. R. Ellis,

- D. P. Fenning, and E. C. Garnett, “Understanding Detrimental and Beneficial Grain Boundary Effects in Halide Perovskites”, *Advanced Materials*, vol. 30, no. 52, p. 1804792, 2018.
153. N. Gao, S. C. Wang, H. S. Ubhi, and M. J. Starink, “A comparison of grain size determination by light microscopy and EBSD analysis”, *Journal of Materials Science*, vol. 40, no. 18, pp. 4971–4974, 2005.
154. Q. Luo, Y. Zhang, C. Liu, J. Li, N. Wang, and H. Lin, “Iodide-reduced graphene oxide with dopant-free spiro-OMeTAD for ambient stable and high-efficiency perovskite solar cells”, *Journal of Materials Chemistry A*, vol. 3, no. 31, pp. 15 996–16 004, 2015.
155. O. Almora, C. Aranda, E. Mas-Marzá, and G. Garcia-Belmonte, “On Mott-Schottky analysis interpretation of capacitance measurements in organometal perovskite solar cells”, *Applied Physics Letters*, vol. 109, no. 17, p. 173903, 2016.
156. G. Garcia-Belmonte and J. Bisquert, “Distinction between Capacitive and Noncapacitive Hysteretic Currents in Operation and Degradation of Perovskite Solar Cells”, *ACS Energy Letters*, vol. 1, no. 4, pp. 683–688, 2016.
157. Y. Kato, L. K. Ono, M. V. Lee, S. Wang, S. R. Raga, and Y. Qi, “Silver Iodide Formation in Methyl Ammonium Lead Iodide Perovskite Solar Cells with Silver Top Electrodes”, *Advanced Materials Interfaces*, vol. 2, no. 13, p. 1500195, 2015.
158. N. M. Johnson, D. J. Bartelink, R. B. Gold, and J. F. Gibbons, “Constant-capacitance DLTS measurement of defect-density profiles in semiconductors”, *Journal of Applied Physics*, vol. 50, no. 7, pp. 4828–4833, 1979.
159. E. Aydin, S. De Wolf, A. S. Subbiah, J. Liu, E. Ugur, R. Azmi, T. G. Allen, M. De Bastiani, M. Babics, F. H. Isikgor, B. Chen, Y. Hou, F. Laquai, E. H. Sargent, and A. U. Rehman, “The multiple ways of making perovskite/silicon tandem solar cells: Which way to go?” *Proceedings of 13th Conference on Hybrid and Organic Photovoltaics (HOPV21)*, 2021.

160. Solarpowerportal, "Oxford PV celebrates 29.5% conversion rate with perovskite cell", <https://www.solarpowerportal.co.uk/news>. Last visited 09-11-2021.
161. M. Jost, A. Al-Ashouri, B. Lipovsek, T. Bertram, R. Schlatmann, C. A. Kaufmann, M. Topic, and S. Albrecht, "Perovskite/CIGS tandem solar cells - Can they catch up with perovskite/c-Si tandems?" *Conference Record of the IEEE Photovoltaic Specialists Conference*, pp. 0763–0766, 2020.
162. N. R. Poespawati, I. Dzikri, J. Sulistianto, T. Abuzairi, M. Hariadi, and R. W. Purnamaningsih, "Perovskite Solar Cells Based on Organic-metal halide Perovskite Materials", *4th International Conference on Nano Electronics Research and Education: Toward Advanced Imaging Science Creation (ICNERE)*, pp. 1–4, 2018.
163. G. Cotella, J. Baker, D. Worsley, F. De Rossi, C. Pleydell-Pearce, M. Carnie, and T. Watson, "One-step deposition by slot-die coating of mixed lead halide perovskite for photovoltaic applications", *Solar Energy Materials & Solar Cells*, vol. 159, pp. 362–369, 2017.
164. S. Ito, S. Tanaka, and H. Nishino, "Lead-halide perovskite solar cells by $\text{CH}_3\text{NH}_3\text{I}$ dripping on $\text{PbI}_2\text{-CH}_3\text{NH}_3\text{I-DMSO}$ precursor layer for planar and porous structures using CuSCN hole-transporting material", *Journal of Physical Chemistry Letters*, vol. 6, no. 5, pp. 881–886, 2015.
165. B. Conings, J. Drijkoningen, N. Gauquelin, A. Babayigit, J. D'Haen, L. D'Olieslaeger, A. Ethirajan, J. Verbeeck, J. Manca, E. Mosconi, F. De Angelis, and H. G. Boyen, "Intrinsic Thermal Instability of Methylammonium Lead Trihalide Perovskite", *Advanced Energy Materials*, vol. 5, no. 15, p. 1500477, 2015.
166. M. Wu, N. Haji Ladi, Z. Yi, H. Li, Y. Shen, and M. Wang, "Stability Issue of Perovskite Solar Cells under Real-World Operating Conditions", *Energy Technology*, vol. 8, no. 4, p. 1900744, 2020.
167. IEA, "Global electricity demand is growing faster than renewables, driving strong increase in generation from fossil fuels", <https://www.iea.org/news>. Last visited 11-11-2021.

168. I. C. Smith, E. T. Hoke, D. Solis-Ibarra, M. D. McGehee, and H. I. Karunadasa, “A Layered Hybrid Perovskite Solar-Cell Absorber with Enhanced Moisture Stability”, *Angewandte Chemie International Edition*, vol. 53, no. 42, pp. 11 232–11 235, 2014.
169. D. Cao, C. Stoumpos, O. Farha, J. Hupp, and G. Kanatzidis, “2D Homologous Perovskites as Light-Absorbing Materials for Solar Cell Applications”, *Journal of the American Chemical Society*, vol. 137, no. 24, pp. 7843–7850, 2015.
170. H. Tsai, W. Nie, J.-C. Blancon, C. C. Stoumpos, R. Asadpour, B. Harutyunyan, A. J. Neukirch, R. Verduzco, J. J. Crochet, S. Tretiak, L. Pedesseau, J. Even, M. A. Alam, G. Gupta, J. Lou, P. M. Ajayan, M. J. Bedzyk, M. G. Kanatzidis, and A. D. Mohite, “High-efficiency two-dimensional Ruddlesden–Popper perovskite solar cells”, *Nature*, vol. 536, pp. 312–316, 2016.
171. L. Na Quan, M. Yuan, R. Comin, O. Voznyy, E. M. Beauregard, S. Hoogland, A. Buin, A. R. Kirmani, K. Zhao, A. Amasian, D. Ha Kim, and E. H. Sargent, “Ligand-Stabilized Reduced-Dimensionality Perovskites”, *Journal of the American Chemical Society*, vol. 138, no. 8, pp. 2649–2655, 2016.
172. Y. Li, J. V. Milić, A. Ummadisingu, J.-Y. Seo, J.-H. Im, H.-S. Kim, Y. Liu, M. Ibrahim Dar, S. M. Zakeeruddin, P. Wang, A. Hagfeldt, and M. Grätzel, “Bifunctional Organic Spacers for Formamidinium-Based Hybrid Dion–Jacobson Two-Dimensional Perovskite Solar Cells”, *Nano Letters*, vol. 19, no. 1, pp. 150–157, 2018.
173. Y. Liu, S. Akin, L. Pan, R. Uchida, N. Arora, J. V. Milić, A. Hinderhofer, F. Schreiber, A. R. Uhl, S. M. Zakeeruddin, A. Hagfeldt, M. Ibrahim Dar, and M. Grätzel, “Ultrahydrophobic 3D/2D fluoroarene bilayer-based water-resistant perovskite solar cells with efficiencies exceeding 22%”, *Science Advances*, vol. 5, no. 6, 2019.
174. W. Li, X. Gu, C. Shan, X. Lai, X. W. Sun, and A. K. K. Kyaw, “Efficient and stable mesoscopic perovskite solar cell in high humidity by localized Dion–Jacobson 2D–3D heterostructures”, *Nano Energy*, vol. 91, p. 106666, 2021.
175. H. Zheng, G. Liu, X. Chen, B. Zhang, A. Alsaedi, T. Hayat, X. Pan, and S. Dai, “High-performance mixed-dimensional perovskite solar

- cells with enhanced stability against humidity, heat and UV light”, *Journal of Materials Chemistry A*, vol. 6, no. 41, pp. 20 233–20 241, 2018.
176. H. Yu, Y. Xie, J. Zhang, J. Duan, X. Chen, Y. Liang, K. Wang, and L. Xu, “Thermal and Humidity Stability of Mixed Spacer Cations 2D Perovskite Solar Cells”, *Advanced Science*, vol. 8, no. 12, p. 2004510, 2021.
177. L. Gao, F. Zhang, X. Chen, C. Xiao, B. W. Larson, S. P. Dunfield, J. J. Berry, and K. Zhu, “Enhanced Charge Transport by Incorporating Formamidinium and Cesium Cations into Two-Dimensional Perovskite Solar Cells”, *Angewandte Chemie International Edition*, vol. 58, no. 34, pp. 11 737–11 741, 2019.
178. R. Garai, R. K. Gupta, M. Hossain, and P. K. Iyer, “Surface recrystallized stable 2D–3D graded perovskite solar cells for efficiency beyond 21%”, *Journal of Materials Chemistry A*, vol. 9, pp. 26 069–26 076, 2021.
179. Y. Cai, J. Wen, Z. Liu, F. Qian, C. Duan, K. He, W. Zhao, S. Zhan, S. Yang, J. Cui, and S. F. Liu, “Graded 2D/3D (CF₃-PEA)₂FA_{0.85}MA_{0.15}Pb₂I₇/FA_{0.85}MA_{0.15}PbI₃ heterojunction for stable perovskite solar cell with an efficiency over 23.0%”, *Journal of Energy Chemistry*, vol. 65, pp. 480–489, 2021.
180. G. Grancini, C. Roldán-Carmona, I. Zimmermann, E. Mosconi, X. Lee, D. Martineau, S. Narbey, F. Oswald, F. De Angelis, M. Grätzel, and M. K. Nazeeruddin, “One-Year stable perovskite solar cells by 2D/3D interface engineering”, *Nature Communications*, vol. 8, no. 15684, 2017.
181. M. Lira-Cantú, “Perovskite solar cells: Stability lies at interfaces”, *Nature Energy*, vol. 2, no. 17115, 2017.
182. S. He, L. Qiu, L. K. Ono, and Y. Qi, “How far are we from attaining 10-year lifetime for metal halide perovskite solar cells?” *Materials Science and Engineering: R: Reports*, vol. 140, p. 100545, 2020.
183. Y. Lin, Y. Bai, Y. Fang, Q. Wang, Y. Deng, and J. Huang, “Suppressed Ion Migration in Low-Dimensional Perovskites”, *ACS Energy Letters*, vol. 2, no. 7, pp. 1571–1572, 2017.

184. X. Xiao, J. Dai, Y. Fang, J. Zhao, X. Zheng, S. Tang, P. Neil Rudd, X. Cheng Zeng, and J. Huang, "Suppressed Ion Migration along the In-Plane Direction in Layered Perovskites", *ACS Energy Letters*, vol. 3, no. 3, pp. 684–688, 2018.
185. J. Cho, J. T. DuBose, A. Ngoc Thien Le, and P. V. Kamat, "Suppressed Halide Ion Migration in 2D Lead Halide Perovskites", *ACS Materials Letters*, vol. 2, no. 6, pp. 565–570, 2020.
186. M. A. Hope, T. Nakamura, P. Ahlawat, A. Mishra, M. Cordova, F. Jahanbakhshi, M. Mladenović, R. Runjhun, L. Merten, A. Hinderhofer, B. I. Carlsen, D. J. Kubicki, R. Gershoni-Poranne, T. Schneeberger, L. C. Carbone, Y. Liu, S. M. Zakeeruddin, J. Lewinski, A. Hagfeldt, F. Schreiber, U. Rothlisberger, M. Grätzel, J. V. Milić, and L. Emsley, "Nanoscale Phase Segregation in Supramolecular π -Templating for Hybrid Perovskite Photovoltaics from NMR Crystallography", *Journal of the American Chemical Society*, vol. 143, no. 3, pp. 1529–1538, 2021.
187. E. J. Juarez-Perez, R. S. Sanchez, L. Badia, G. Garcia-Belmonte, Y. S. Kang, I. Mora-Sero, and J. Bisquert, "Photoinduced Giant Dielectric Constant in Lead Halide Perovskite Solar Cells", *Journal of Physical Chemistry Letters*, vol. 5, no. 13, pp. 2390–2394, 2014.
188. M. Georgioudakis and V. Plevris, "A Comparative Study of Differential Evolution Variants in Constrained Structural Optimization", *Frontiers in Built Environment*, vol. 6, p. 102, 2020.
189. A. O. Alvarez, R. Arcas, C. A. Aranda, L. Bethencourt, E. Mas-Marzá, M. Saliba, and F. Fabregat-Santiago, "Negative Capacitance and Inverted Hysteresis: Matching Features in Perovskite Solar Cells", *Journal of Physical Chemistry Letters*, vol. 11, pp. 8417–8423, 2020.
190. T. Shi, W. J. Yin, and Y. Yan, "Predictions for p-type $\text{CH}_3\text{NH}_3\text{PbI}_3$ perovskites", *Journal of Physical Chemistry C*, vol. 118, no. 44, pp. 25 350–25 354, 2014.
191. Q. Liu, Y. C. Hsiao, M. Ahmadi, T. Wu, L. Liu, S. Haacke, H. Wang, and B. Hu, "N and p-type properties in organo-metal halide perovskites studied by Seebeck effects", *Organic Electronics*, vol. 35, pp. 216–220, 2016.

192. J. V. Milić, D. J. Kubicki, L. Emsley, and M. Grätzel, “Multi-functional Molecular Modulation for Efficient and Stable Hybrid Perovskite Solar Cells”, *Chimia*, vol. 73, no. 4, pp. 317–323, 2019.
193. J. V. Milić, J. Im, D. J. Kubicki, A. Ummadisingu, J. Seo, Y. Li, M. A. Ruiz-Preciado, M. I. Dar, S. M. Zakeeruddin, L. Emsley, and M. Grätzel, “Supramolecular Engineering for Formamidinium-Based Layered 2D Perovskite Solar Cells: Structural Complexity and Dynamics Revealed by Solid-State NMR Spectroscopy”, *Advanced Energy Materials*, vol. 9, no. 20, p. 1900284, 2019.
194. M. Ruiz-Preciado, D. Kubicki, A. Hofstetter, L. McGovern, M. Futscher, A. Ummadisingu, R. Gershoni-Poranne, S. Zakeeruddin, B. Ehrler, L. Emsley, J. Milić, and M. Grätzel, “Supramolecular Modulation of Hybrid Perovskite Solar Cells via Bifunctional Halogen Bonding Revealed by Two-Dimensional ^{19}F Solid-State NMR Spectroscopy”, *Journal of the American Chemical Society*, vol. 142, no. 3, 2020.
195. Scipy, “Scipy optimize differential evolution”, *SciPy v1.7.1 Manual*, <https://docs.scipy.org/doc/scipy/reference/generated>. Last visited 15-11-2021.
196. P. P. Biswas, P. N. Suganthan, and G. A. Amaratunga, “Minimizing harmonic distortion in power system with optimal design of hybrid active power filter using differential evolution”, *Applied Soft Computing Journal*, vol. 61, pp. 486–496, 2017.

SUMMARY

Ion migration takes place in lead halide perovskites when either the A, B, or X element within the ABX_3 perovskite structure become a mobile ionic species and start migrating through the perovskite layer. This transient behavior leads to instability in the lead halide perovskite layers, and, importantly, might not be fully reversible in the solar cells in which these perovskite layers are incorporated. This makes ion migration a barrier to the full development of perovskite materials in the solar sector. In this thesis, we aim to understand the different factors influencing ion migration in lead halide perovskite solar cells, with a view of eventually mitigating or suppressing this feature altogether. We do so by taking a variety of perovskite systems and quantifying their ion migration dynamics. The measurement technique used throughout this thesis is transient ion drift, a capacitance-based measurement which can track ion dynamics within semiconductor devices. The key parameters we extract from this technique are the nature of the mobile ions, their migration activation energies, their diffusion coefficients and their densities within the perovskite films.

With climate change already happening before our eyes, we need to develop the renewable energy sector, and particularly the solar sector. In **Chapter 1** we introduce perovskite solar cells along with their key properties, and note that stability issues still prevent these perovskite solar cells from "shining through" in commercial solar cells. We further introduce the ion migration process, along with the different experimental and modelling techniques to observe this phenomenon. Finally, we introduce the transient ion drift technique, and elaborate on the fitting procedure and underlying assumptions used in this thesis. In the following Chapters, we use transient ion drift to characterise ion migration in a variety of lead halide perovskite solar cells.

MAPbBr₃ has been shown to be more stable than MAPbI₃, and we explore whether this beneficial stability property might (also) come from a change in the ion migration properties. In **Chapter 2** we look at the influence of the perovskite composition on ion migration dynamics within the perovskite layer, comparing the two pure-halide systems of MAPbBr₃ and MAPbI₃. We find that, upon substitution of iodide for bromide, halide migration is reduced, through a reduction of the mobile ion concentration and a slower ion diffusion coefficient for the bromide species compared to the iodide species. Surprisingly, we also observe a change in the cation migration, with a suppression of methylammonium migration in the MAPbBr₃ solar cells. The perovskite composition thus plays a crucial role in ion migration dynamics within the perovskite layers.

Nowadays, state-of-the-art perovskite solar cells combine multiple halide ions: we therefore extend our work to mixed-halide perovskites with varying ratios of bromide to iodide in **Chapter 3**. We find that in mixed-halide perovskites, there are 2 mobile halide processes compared to the single mobile halide species in the pure-halide perovskites. We also find that the migration activation energies in the mixed-halide systems is reduced, and that the density of mobile halide ions increases compared to the pure-halide systems. We further compare the ion migration dynamics of the low-bromide perovskites under dark and illumination conditions. Under illumination conditions, we notice the appearance of methylammonium migration. Quantifying the ion migration processes in mixed-halide perovskites thus further confirms the key role played by the perovskite composition in the ion migration dynamics.

Perovskite solar cells can be made from a variety of synthesis and fabrication methods, which can affect important aspects of the perovskite layers, such as the crystallinity of the films. While this might not affect the efficiency of the solar cells, the ion migration dynamics might be changed. In **Chapter 4** we look at the impact of grain size on the ion migration dynamics in MABr₃ perovskite solar cells. We find that in films with smaller grains, the ions migrate through the grain boundaries, whereas films with larger grains show 2 migration processes, where one is mediated by the grain boundaries, and the second is mediated by the bulk of the perovskite. We also find an increase in the activation energy for bromide migration in the films with larger grains. Crystallinity is thus one of the pathways to consider for ion migration mitigation.

To benefit both from the efficiency of the 3D perovskites and from the stability of the 2D perovskites, new combined 2D/3D solar cells have been developed, where a thin 2D layer is deposited on top of a thicker 3D perovskite. We study the ion migration dynamics of these mixed-dimensionality perovskite systems in **Chapter 5**, comparing various 2D layers, made out of FEA, PEA or a mix of FEA and PEA spacer molecules. We find that ion migration is reduced in all solar cells incorporating a 2D layer, but that the specific process is dependent on the 2D spacer layer composition. FEA reduces ion migration by decreasing the mobile halide density of the first halide migration process, while PEA reduces ion migration both by decreasing the mobile halide density and increasing the activation energy of the second halide migration process. Modifying the interfaces of the 3D perovskites by addition of a lower-dimensionality 2D perovskite layer is thus another pathway for mitigation of ion migration in lead halide perovskite solar cells.

SAMENVATTING

Ionenmigratie vindt plaats in lood halide perovskieten wanneer het A-, B- of X-element in de ABX_3 -perovskietstructuur een mobiel ion wordt en door de perovskietlaag migreert. Dit gedrag leidt tot instabiliteit in de lood halide perovskietlagen en, nog belangrijker, is mogelijk niet volledig omkeerbaar in de zonnecellen waarin deze perovskietlagen zijn verwerkt. Dit maakt ionenmigratie een barrière voor de volledige ontwikkeling van perovskietmaterialen in de zonne-energiesector. In dit proefschrift streven wij ernaar de verschillende factoren die ionenmigratie in lood halide perovskietzonnecellen beïnvloeden te begrijpen, met het oog op het uiteindelijk verminderen of onderdrukken van deze eigenschap. We doen dit door de ionenmigratiedynamiek van een verscheidenheid aan perovskietsystemen te kwantificeren. De meettechniek die in dit proefschrift wordt gebruikt is transiënte ionendrift. Dat is een op elektrische capaciteit gebaseerde meting die de ionendynamiek in halfgeleider devices kan volgen. De belangrijkste parameters die we met deze techniek bepalen zijn de aard van de mobiele ionen, hun migratie-activeringsenergieën, hun diffusiecoëfficiënten en hun dichtheden in de perovskietlagen.

Nu de klimaatverandering al voor onze ogen plaatsvindt, moeten we de hernieuwbare energie sector versterken, en daarbij met name de zonne-energie sector. In **Hoofdstuk 1** introduceren we perovskietzonnecellen samen met hun belangrijkste eigenschappen, en merken we op dat stabiliteitsproblemen nog steeds voorkomen dat deze perovskietzonnecellen hun commerciële toepassing vinden. Verder introduceren we het ionenmigratieproces, samen met de verschillende experimentele en modelleringstechnieken om dit fenomeen te observeren. Ten slotte introduceren we de transiënte ionendrifttechniek, en gaan we dieper in op de fit en onderliggende aannames die in dit proefschrift worden gebruikt. In de volgende hoofdstukken gebruiken we transiënte ionendrift om ionenmigratie in verschillende lood halide perovskietzonnecellen te karakteriseren.

Het is aangetoond dat MAPbBr_3 stabiel is dan MAPbI_3 , en we onderzoeken of deze gunstige stabiliteitseigenschap (deels) het gevolg kan zijn van een verandering in de ionenmigratie-eigenschappen. In **Hoofdstuk 2** kijken we naar de invloed van de samenstelling van de perovskietlaag op de dynamiek van ionenmigratie, waarbij we de twee pure halogenidesystemen van MAPbBr_3 en MAPbI_3 vergelijken. We ontdekken dat, na substitutie van bromide door jodide, halidemigratie wordt verminderd door een verlaging van de mobiele ionenconcentratie en een lagere ionendiffusiecoëfficiënt voor de bromide in vergelijking met de jodide. Verrassend genoeg zien we ook een verandering in de kationenmigratie, met een onderdrukking van methylammoniummigratie in de MAPbBr_3 -zonnecellen. De perovskietsamenstelling speelt dus een cruciale rol in de dynamiek van ionenmigratie in de perovskietlagen.

Tegenwoordig combineren state-of-the-art perovskiet zonnecellen meerdere halide-ionen: daarom breiden we ons werk uit naar gemengde-halide perovskieten met variërende verhoudingen van bromide tot jodide in **Hoofdstuk 3**. We ontdekken dat er in gemengde halide perovskieten twee mobiele halide processen plaatsvinden vergeleken met de enkele mobiele halidesoort in de pure halide perovskieten. We ontdekken ook dat de migratie-activeringsenergieën in de gemengde halidesystemen lager zijn, en dat de dichtheid van mobiele halide-ionen toeneemt in vergelijking met de pure halide systemen. Verder vergelijken we de ionenmigratiedynamiek van de bromide-arme perovskieten onder donkere en verlichte omstandigheden. Onder verlichte omstandigheden zien we het op gang komen van methylammoniummigratie. Het kwantificeren van de ionenmigratieprocessen in gemengde halide perovskieten geeft dus verdere bevestiging van de sleutelrol die de perovskietsamenstelling speelt in de ionenmigratiedynamiek.

Perovskietzonnecellen kunnen worden gemaakt met een verscheidenheid aan synthese- en fabricagemethoden, die belangrijke aspecten van de perovskietlagen kunnen beïnvloeden, zoals de kristalliniteit van de lagen. Hoewel dit mogelijk geen invloed heeft op de efficiëntie van de zonnecellen, kan de dynamiek van de ionenmigratie veranderen. In **Hoofdstuk 4** kijken we naar de impact van kristalkorrelgrootte op de ionenmigratiedynamiek in MAPbBr_3 perovskietzonnecellen. We ontdekken dat de ionen langs de korrelgrenzen migreren in lagen met kleinere korrels, terwijl lagen met grotere korrels twee migratieprocessen

vertonen, waarbij het ene proces verloopt langs de kristalkorrelgrenzen en het tweede proces verloopt door het kristalrooster van perovskiet kristalkorrels. We ontdekken ook een toename van de activeringsenergie voor bromidemigratie in de lagen met grotere kristalkorrels. Kristalliniteit is dus een van de parameters om te in acht te nemen voor het verminderen van ionenmigratie.

Om te profiteren van zowel de efficiëntie van 3D-perovskieten als van de stabiliteit van 2D-perovskieten, zijn nieuwe gecombineerde 2D/3D-zonnecellen ontwikkeld, waarbij een dunne 2D-laag bovenop een dikkere 3D-perovskiet wordt geplaatst. We bestuderen de ionenmigratiedynamiek van deze perovskietsystemen met gemengde dimensies in **Hoofdstuk 5**, waarbij we verschillende 2D-lagen vergelijken, gemaakt van FEA, PEA of een mix van FEA en PEA tussenlaagmoleculen. We ontdekken dat ionenmigratie wordt verminderd in alle zonnecellen met een 2D-laag, maar dat het specifieke proces afhankelijk is van de samenstelling van de specifieke 2D-tussenlaag. FEA vermindert de ionenmigratie door de dichtheid van het mobiele halide in het eerste halidemigratieproces te verlagen, terwijl PEA de ionenmigratie vermindert door zowel de dichtheid van de mobiele halide te verlagen als door de activeringsenergie van de tweede halidemigratieproces te verhogen. Het aanpassen van de grensvlakken van de 3D-perovskieten door toevoeging van een lager dimensionale 2D-perovskietlaag is dus een andere manier om ionenmigratie in lood halide perovskietzonnecellen te verminderen.

LIST OF PUBLICATIONS

The Chapters of this thesis are based on the following publications :

1. Lucie McGovern, Moritz H. Futscher, Loreta A. Muscarella and Bruno Ehrler, "Understanding the Stability of MAPbBr₃ versus MAPbI₃: Suppression of Methylammonium Migration and Reduction of Halide Migration", *Journal of Physical Chemistry Letters*, vol. 11, no. 17, pp. 7127–7132, 2020. (**Chapter 2**)
2. Lucie McGovern, Gianluca Grimaldi, Moritz H. Futscher, Eline M. Hutter, Loreta A. Muscarella, Moritz C. Schmidt and Bruno Ehrler, "Reduced Barrier for Ion Migration in Mixed-Halide Perovskites", *ACS Applied Energy Materials*, vol. 4, no. 12, pp. 13431–13437, 2021. (**Chapter 3**)
3. Lucie McGovern, Isabel Koschany, Gianluca Grimaldi, Loreta A. Muscarella and Bruno Ehrler, "Grain Size Influences Activation Energy and Migration Pathways in MAPbBr₃ Perovskite Solar Cells", *Journal of Physical Chemistry Letters*, vol. 12, pp. 2423–2428, 2021. (**Chapter 4**)
4. Lucie McGovern, Rens van Roosmalen, Anwar Alanazi, Gianluca Grimaldi, Moritz C. Schmidt, Jovana V. Milić and Bruno Ehrler, "Effect of a 2D layer on ion migration in perovskite solar cells, comparing PEA, FEA and mixed PEA/FEA systems", in preparation. (**Chapter 5**)

Other publications by the author:

5. Samuel Palato, H el ene Seiler, Lucie McGovern, Timothy G. Mack, Lakshay Jethi and Patanjali Kambhampati, "Electron Dynamics at the Surface of Semiconductor Nanocrystals", *Journal of Physical Chemistry C*, vol. 121, no. 47, pp. 26519–26527, 2017.
6. Moritz H. Futscher, Ju Min Lee, Lucie McGovern, Loreta A. Muscarella, Tianyi Wang, Muhammad I. Haider, Azhar Fakhruddin, Lukas Schmidt-Mende and Bruno Ehrler, "Quantification of Ion Migration in $\text{CH}_3\text{NH}_3\text{PbI}_3$ Perovskite Solar cells by Transient Capacitance Measurements", *Materials Horizons*, vol. 6, no. 7, pp. 1497–1503, 2019.
7. Marco A. Ruiz-Preciado, Dominik J. Kubicki, Albert Hofstetter, Lucie McGovern, Moritz H. Futscher, Amita Ummadisingu, Renana Gershoni-Poranne, Shaik M. Zakeeruddin, Bruno Ehrler, Lyndon Emsley, Jovana V. Mili c and Micha el Gr atzel, "Supramolecular Modulation of Hybrid Perovskite Solar Cells via Bifunctional Halogen Bonding Revealed by Two-Dimensional ^{19}F Solid-State NMR Spectroscopy", *Journal of the American Chemical Society*, vol. 142, no. 3, pp. 1645–1654, 2020.
8. Eline M. Hutter, Loreta A. Muscarella, Francesca Wittmann, Jan Versluis, Lucie McGovern, Huib J. Bakker, Young-Won Woo, Young-Kwang Jung, Aron Walsh and Bruno Ehrler, "Thermodynamic Stabilization of Mixed-Halide Perovskites Against Phase Segregation", *Cell Reports Physical Science*, vol. 1, no. 8, p. 100120, 2020.
9. Loreta A. Muscarella, Eline M. Hutter, Francesca Wittmann, Young Won Woo, Young-Kwang Jung, Lucie McGovern, Jan Versluis, Aron Walsh, Huib J. Bakker and Bruno Ehrler, "Lattice Compression Increases the Activation Barrier for Phase Segregation in Mixed-Halide Perovskites", *ACS Energy Letters*, vol. 5, no. 10, pp. 3152–3158, 2020.
10. Maarten van der Geest, Lucie McGovern, Stefan van Vliet, Hanya Y. Zwaan, Gianluca Grimaldi, Jeroen de Boer, Roland Bliem, Bruno Ehrler and Peter M. Kraus, "Extreme-Ultraviolet Excited Scintillation of Methylammonium Lead Bromide Perovskites", in preparation.

ACKNOWLEDGEMENTS

I would like to start these acknowledgements by thanking my supervisor Bruno. Dear Bruno, it has now been almost 5 years since you gave me the opportunity to work within your group in this green AMOLF building. I am so thankful for your careful supervision. It has this beautiful balance of letting your students try out their own ideas and develop themselves, while always being present and a resource with lots of helpful input, sharp scientific intuitions and ideas, and keeping in mind the bigger picture. You lead the way by example, you are open about your growth as a group leader and are also open to new initiatives and trying things out, and are also patient, taking the time to explain the scientific points that were unclear to me. I was excited to start in a group with a supervisor who truly believes in making solar cells for a better and greener future, and this truly reflects in the deeper motivation you give to your group and to the meaning you give to our research. You also care personally about your students and make us feel like we are in a team together, and are one of the most present, reliable and dedicated supervisors I have ever seen. I am truly grateful for having been a part of the Hybrid Solar Cells (I will certainly miss it a lot) but of course after 5 years the time has come for some new people to fill in the space and continue the adventure. I hope I can bring your many teachings together with me in my next stages.

My scientific growth has benefited from the true quality of the group leaders at AMOLF. I would like to thank my co-supervisor Erik, for the many scientific chats we have shared, the encouragements all along the way, and the top-notch questions which always inspired me to deepen my own understanding of my research. I am very impressed by the talks you give (you have a gift for keeping an audience captive). I'm also impressed of the way you gracefully managed to keep on calmly asking questions and answering them while your son was on your shoulders and clearly trying to distract you. I also want to thank Albert, the founder of the LMPV program which I have benefited so much from. Dear Albert, you are such an inspiration to all surrounding you. Not only for the science you do, but also because you are a true-born leader, who takes care that

their team enjoys themselves such that they want to give their very best. The LMPV program you have set up truly has your fingerprint - you always encourage us to collaborate together and get involved in each others' projects, and you are always keeping an eye on how to set up a more inclusive environment, where a diverse team of scientists can all thrive. This results in a stimulating and positive atmosphere that has contributed so much to my appreciation of my master's and PhD. You are also present in the harder times, and I will never forget that you came by to check on me after my fire incident - it truly made Amsterdam feel like a safer place. Your help and guidance as I was applying for the next stages in my career made me feel confident and supported, and I will keep looking up to you for a very long time! There is another great LMPV group leader who I look up to. Esther, I want to thank you for the many scientific questions you have asked me, the nice discussions about being a group leader and also for the opportunity to present my results at the Klein Colloquia you were organizing. I will also not forget your talk at the "Women in Science" day, which was such a great success. During my stay as a PhD, a new group leader also started in the LMPV program. Wiebke, your science sounds very exciting and your passionate way of explaining it is super motivating. I wish you lots of success.

A special mention also goes here to my first Chemistry teacher from university, Jérémie Caillat. Your courses were the best, and your encouragements all along the way allowed me to become the scientist I am now. I am thankful for our friendship and your ongoing support.

During this PhD, I feel lucky to have been working with such an amazing crew as the Hybrid Solar Cells group. Moritz F., you were the very first to welcome me in the lab. How lucky I have been to have been trained by you! Not only did you train me while I was a master's student, but further on when I came back in the group as a PhD, you trained me on the TID setup you had just built - *the* setup I ended up using my whole PhD. Your training however went way above just the technical and scientific aspects of a project, you also showed how to come up with interesting scientific questions, how to apply for a conference and which conference was a smart choice for my research, and while on a conference, how to start a fruitful collaboration. You also taught me the true value of collaboration, and to never see other groups working on the same topic as competitors. You always put the bar high, but you also gave me the tools to get there. For all of these teachings, as well as your generosity

and patience, I will remain very grateful. Loreta, my dear mevrouw. We started our PhDs with only one week difference, and have shared every office together since! It felt so good to be able to share all our ups and downs, and our daily/monthly/yearly stress through the epic moments of this 4-year adventure... You are very ambitious, down-to-earth, tenacious in your efforts, and your humor is so witty! I'm glad we could share the trip to the US together, and all the many behind-the-scenes moments of the PhD. Thinking about the american trip... Christian, thank you so much for accepting, together with Jenny, to drive us all the time during our US trip! I always had super nice chats with you, and along the way I discovered a lot about hip ways to make good coffee and went back through all the good rock classics in the lab. You were also often the first person to hear me practicing my new Dutch sentences after the courses at UvA- thanks for allowing me to speak my super slow dutch to you! Jumin, thank you for bringing South Korea to the group! I loved chatting with you about how you envisioned both South Korea and Europe, and your humor was also so great :) Many thanks also go to you for your patience and careful training in the lab, and your helpful ideas (including on how to restore all the data I had lost on the EQE!...). I hope we get to meet again some day. Marc, thank you a million times! You are such a nice person - in the beginning of my project I was quite nervous in the lab, and not too sure of myself on some of the technical pieces of equipment - you were always there, super patient and present for those who needed your help. You made me feel way more comfortable in the lab than I originally was, and for this I really thank you. You're also very fun outside of work, and I'm happy we could share beers at many of the group events! Tianyi, cheers for your remarkable memory, which was very helpful as I was starting out in this crazy perovskite field with 1000+ papers a year. I enjoyed our chats about Chinese cooking a lot. Benjamin, thank you for your great help in the lab and with any Mathematica or plotting issues I was facing - you were always super patient and generous. I'm happy we shared the HOPV conference in Rome together, as well as the conference in Paris. Eline, you have been such a role model for me! Your way of looking at science, finding the most interesting and intricate questions to ask, and then deeply immersing into them, but also your incredible sense of planning and top-notch intuitions. I'm glad I got to work with you and got inspired by you, and I hope I will grow to be a successful leader like you are. Gianluca, how lucky I have been that you joined the group. You were so helpful with every question that I had that you soon got

involved into all of my projects! You are such a kind person, it was great to be able to have such nice conversations. I also won't forget your presence after the fire at my place, which really made me feel cared for in Amsterdam. I've also shared with you some of the rocky behind-the-scenes frights at being scooped on a paper or being tired of the stress of research, and your reassurance was always precious. Silvia, thanks for your patience taking the elevator with me after my bike crash, and for our nice chats on how to shift the patriarchy in science. I'll keep a fun memory of double zooming in with you at the conference. Imme, you had a rough start with your PhD, starting only 4 days before lockdown... This only makes your energy to make the group a fun and lively place stand out even more! Thanks for all the movie nights you organised, for staying on the phone with me when I couldn't log into the virtual room, and for helping me balance myself on the ice skates! Hanging out with you at Oerknal or for a falafel night was always very fun. I wish you many "real" conferences in the second half of your PhD, and lots of fun and success with your project. Maria, I'm happy we got to chat more during the group trip to Germany, and lucky we could save Loreta's bag a few times! Thanks for the nice conversations about science, grant proposals, and dream jobs. Jeroen, how nice that you joined from the dark side of the lab to ours (haha)! We certainly made you feel like you had to make a choice, but you ended up in the team that won at VR Ping Pong, so I hope we made it worth it :) With you I got to learn many fun things about dutch culture (including the 'moetjes'), and how and when to schedule fun jokes. You saved me many times by allowing me to go on the back of your bike, and you were also kind enough to propose to translate my sammenvatting. Hartelijke dankjewel! Moritz S., what to say? You're simply the most friendly, kindest and most fun person to hang around with. Meeting you definitely was a huge part of my happiness at AMOLF. Your presence while I was applying for my dream job (and I did spend *hours* talking about it!...), and comforting smile when I felt super stressed went straight to my heart. I'm also deeply thankful for you reminding me to backup my thesis (woopsie!) and for your numerous latex helpline sessions - truly the latex part of this thesis owes a lot to you. I'll certainly miss our daily Spar adventures in my new job, but I'll keep lots of sweet memories too, from your patience while we were hiking in Bavaria to the super fun movie nights and games nights (yes, you may have won at poker, but I won at pool, so let's say that it's a 1-1 for France-Germany :))

Now comes the time for me to thank two more special people from the Hybrid Solar Cells group. Dear Isabel, dear Rens, we've each spent almost a year working together, and I look back very happily at these moments. Isabel, I can tell you now, before meeting you -the first master student I was about to supervise for almost a year- I was kind of nervous. And then you came along! Not only were you bright and very motivated (which made my job so much easier!), but you were also friendly, chatty, and witty, and I thoroughly enjoyed both working with you and chatting about your lovely 5 brothers and sisters in Germany. You continued your hard work and kept your motivation even when the pandemic hit, going to the lab alone to finish experiments, and working from home fitting transients with your super slow laptop and your slow wifi. Next to your Master's project, you were also working as a bartender, and I can tell you that I admire your courage to take on Friday evening shifts after having spent the daytime installing a new device in the TID sample holder. You did amazing, and I'm very proud of you. Rens, you were the second master student I supervised, and again, what a combo! You were motivated, intelligent, and so much fun to hang around! Your passion for Lord of the Rings gave rise to quite a new decoration vibe to the setup, which I thoroughly enjoy -I also believe Moritz enjoys it a lot, super lucky the 3 of us are LOTR fans ;) You overcame a set of tough challenges, and never gave up on fitting these tricky transients! While studying in our group, you too were also working - you were a cook in a Spanish restaurant. Your level of energy and motivation to handle these 2 projects, and also your literature thesis at the same time, was very impressive. I hope you have a lot of fun in your next steps, and that we'll soon have another beer with the capacitance team.

There are many more that made the Hybrid Solar Cells group so special. In no specific order... Thanks Toon for your endless energy, and your super cool magic tricks! You are an inspiration to work up towards a better and greener future. Emil, it was always great to chat, thanks for sharing your restaurant suggestions ("Boi boi" is one of my faves now!) and also for sharing the puzzle vibe during lockdown. Weiyi, thank you for helping me cycle with the plates for my housewarming party, this was crazy! I'm also glad for all the personal chats we shared. Menke, it was great to share some artistic and theatre hype together, and how cool it was to be dancing while you were the DJ! Your encouragements and understanding while I was applying for my dream job were very precious. Oscar and Floris, it was really nice to have the super late

drinks in Munich and to go see the wave (thanks for agreeing on this late-night decision...). And I'm sorry Oscar that I tried to eliminate you 4 or 5 times during the game in Bavaria!... Cedric, thanks for the nice bouldering sessions we shared, and all your tips and tricks. Cheers David for the nice coffee break chats, and it was cool to share one more round of drinks in Oost! Georg, I'm super happy we decided to go to Lory's defense in Groningen together! May the power of Burger King save you many more times from lockdown-dinnerless-cities. Joris I'm happy about the cool tea breaks and discussions about sports. Arnoud, I'm glad we got to share our first scientific conference trip together. Your excitement for science and for meeting with new people was always great. Marnix, cheers for all the nice coffee chats, and for organizing such a nice AMOLF Christmas party with the PV - the photo of the HSC group as a rock band is epic! Stefan, I'm super happy that you came back to AMOLF again, and I hope we can still share at least one LMPV Spring dinner together! Koen, it was cool to share the EQE, probe station and evaporator setups during long afternoons in the lab, that got more fun thanks to your presence. Andrew, it was great to have you at AMOLF as a guest, and super nice to bump into you again at MRS!

The positive energy that I got from AMOLF is also linked to a few more people that I would like to acknowledge here. Juliette, your morning smile at AMOLF always lightened up my mood and set a positive tone for the day. Gerda, your smile is very contagious, and I'm happy we could enjoy a few chitchats here and there. Petra, you were always so enthusiast and chatting with you was always a pleasure.

During my time as a PhD I have had the chance to interact and collaborate with great scientists, whom I'd like to thank here. Thanks Sandy for your time in Amsterdam teaching the group how to make super nice perovskites, it was great fun to be 5 people watching you through the glovebox window. I also keep a fond memory of your warm welcome in Lausanne. Thank you Jovana for being such a wonderful scientist to collaborate with. I admire your work as much as I admire your way of doing research. You are always very encouraging towards the younger generation of scientists, and simply such a generous and kind person to work with. I will keep being inspired by your great leadership in my future projects. I also want to say cheers to Maarten for the nice scientific discussions we've shared. Our project together was in a completely new scientific direction for me, and this was very enriching. I wish you lots of fun during the rest of your PhD!

I'm also thankful for my time at AMOLF on a personal level, as it is a place where I made some beautiful and dear friends. Nasim, for you I want to use only the best and most qualitative words (and we both agree these are the emotional words). My loving, caring, Iranian-Amsterdam bestie, you have been my sunflower in this new city. Anytime I was lost, I would look up towards you to find my direction. And as a true flower, when looking at you, I always saw you rooting yourself and growing to new beautiful cycles of life. You bring such passion, intensity and understanding to my life, and I simply love our deep and psychological conversations. I'm honored to have your painting as the cover of my thesis and I thank you for being my paranymf (and in the process accepting to bow to science!). I already look forward to many more chapters together. Susan, you bring the **combo** of glamorous and nerdy smart-cookie together to a whole new level, my curly bestie! I'm deeply thankful for your daily presence in my life, and for our chats regarding just about 1000 topics (though we have our faves of course, from how to smash the patriarchy to how to best take care of our curls). You speed-biked to my place in literally 6 minutes the night that you also called the fire department for me, and you took such beautiful care of me this evening, for which I will eternally be grateful. Tonight you will be my smashing partynymf, and I'm lucky to have you by my side. Jenny - my greek beautyyy! You welcomed me in your life, and I still feel so lucky about our friendship. Your amazing laugh, that I still recall filling all of AMOLF's second corridor (and which occasionally helped locate you at the other end of Flevopark!), and your generosity, true open-mindedness, willingness to celebrate life in all its beauty and also your presence for those you love - you are a vibrant soul my dear, *και σε αγαπω φιλε μου*. All of Amsterdam misses you, but we love you from here, and I can't wait to *finally* visit your village and your home - coming soon! Carolyn, from the "AMOLF masters" generation to the "AMOLF PhDs" generation, we did it all, and we even did it so well that we became the submitter sisters! Thanks for enlightening so many AMOLF borrels, Veldhoven parties (and many many more parties) with your dance moves, and for your sweetness and thoughtfulness, dropping by surprise chocolates on my desk in the last months of writing. You kick ass dear, so go team tiny! Mareike, as soon as I saw you, I felt like we would share a vibe and I wanted to be your friend. I barely knew you that you were already present at my 25th birthday and we were partying together. I'm super happy about our deep conversations, our movie nights, and this time you made the most beautiful Halloween makeups for the two of us - I'm

still impressed about your many skills and energy, and glad to have you present on this special defense day. Giorgio! When you asked me if I wanted to be your office mate, I told Lucas that "the most cool and smiling person at AMOLF" just asked me if we could share an office together- I was so excited! You are such a caring and sweet friend, and also a crazy one when it's party timeeee! (aka Gasolina time)! Thanks for being the most fun dancer I know, and for all the life advice chats we had. I hope to see you again super soon dear ragazzo. Robin, I'm happy we got to meet in my last PhD year! From the classic "lunch & working" sessions we shared together with Nasim and Susan, we grew and evolved and are now launching a sect together ;))) It was fun to spend time together, and I thank you for your pep talks and the sweet Sinterklaas poem. I won't forget running from your place with the mevrouwen just before the curfew kicked in, nor will I forget your delicious vegetarian recipes. Laura, thanks for welcoming me at your place in Berlin for your defense and for your defense parties! You are both so much fun to hang around and a thoughtful and sweet friend. The fact you also worked on perovskites made going to conferences so exciting. Magda and Verena, you were such a beautiful duo. Thank you Magda for making me discover Yagoy - I'm happy about the yoga sessions we shared, and the one-off bouldering time -we should definitely do this again! In my mind you'll always be part of my "PhD generation", and I'm glad to see you successful and happy in Amsterdam. Also cheers for the midnight grapes at New Year's Eve :) Verena, I hope you realise everyone looked up at you in LMPV and admired you - I know I did! I'm glad for all the nice conversations we've shared, and also the dinners together with Magda, Kevin and Nasim. Cheers Augustin for letting me in on the perfect Mexican traditions for NYE (I won't forget what the black stands for), and for all the colorful parties you organized. Parisa, I'm glad our PhD times could overlap, even if just for a tiny bit! I admire your way of following your heart and not taking no for an answer. You're an amazing mevrouw. Marloes, you are such a beautiful person inside and outside. I know our levels of nervousness can sometimes match, so I wish us both all the comfort and acceptance yoga can bring, and the optimism to know that everything will always be all right. Roel, I definitely feel like I met you for real at Nasim's party! The thug/gangster moves were amazing, and I'm glad we could dance all night long. Daphne, your humor is a bulldozer, and your kindness has no equal! I loved your sheer energy when discussing any topic, big or small. Ruslan, I'll never forget you invited me to my first AMOLF party :) We've now shared evenings out in Paris, Amsterdam,

and Munich, so I wonder which city will be the next! Let's finally have this poker rematch then! Eitan, thank you for bringing your wisdom in the most dry humorous way, and for the philosophical 360 degrees chats about friendship or living abroad. Sven, your passion for science and combined desire to live a well-balanced life have been super inspiring to me. I also want to say the warmest thank you for having been such an encouraging proof reader for all of my papers. Jesse, it was always great to chat, and I had a lot of fun preparing all the OR sessions together! Thanks to you I know what the Groningen flag looks like and will hopefully stop confusing it with the frisian one - this will avoid me getting kicked out from my own defense at RUG ;) Lukas, thank you for hosting some of the most dramatic parties I've ever been to (the smoke machine is just beyond this world!) and your friendliness. I am very grateful for your help with the cover of this thesis. Ruben, my first ARCNL friend! I loved the beer-making session together with Lucas, and all the nice chats at dinners, Veldhoven parties and NWO sports days. You are talkative and open-minded, and I hope to see you next time you're in Amsterdam.

I also want to thank the Frenchies at AMOLF who made me feel at home! Merci Kevin pour m'avoir rassurée tant de fois au début de ma thèse, et de m'avoir dit que ca allait le faire ;) Je garderai longtemps en tête notre participation à la karaoké night... Alexandrie, Alexandra... aaah! (pas sûr qu'on ait fait honneur à la culture française ce soir-là haha). Anastassia, c'était tellement chouette de te rencontrer, de parler autant de danse, et de partager cette soirée magique à Odessa - elle reste gravée dans mon coeur. Anna, quelle office mate de choc pour mes 3 mois d'écriture de thèse. Je crois que tu m'as vu au pic de l'intensité ;) entre la soirée poker, toutes les soirées Le Seigneur des Anneaux, et les sessions bouldering, j'ai kiffé les moments passés ensemble!

There are also so many others that made AMOLF such a warm place to work at. Andrea, Tom, Giada, Isabelle, Nick, Sophie, Hugo, Nika, Kelly, Matthias, Harshal, Julia, Hongyu, Biplab, Eliane, Manuel, Chris, Linde, Sarah, Francesca, Mees, Yorick, Yuha, Pascal, Ilan, Javier, Federica, Giulia, Sanghamitra, Luuk, thanks for all the nice moments we shared. Many cheers also go to the great people I met from AMOLF's "sister-institute", ARCNL. John, Zoi, Stephen, Lars, Yahia, Joris, it was always great to see you and share a beer at Foeders or Poesiat & Kater.

I also made some other beautiful friends in the Netherlands. Léa and Lars, meeting you two was the best gift 2020 could offer! I will always keep super fond memories of the time spent the 4 of us together in your tiny house - I love the way you imported us by car and how we spent entire weekends cooking, tanning, chilling, painting, and enjoying the "à la Lars" brunch with perfectly-cooked eggs. You two beautiful souls made the word "house" rime with "home", and going to yours always felt like a holiday. Visiting you again in Jena warmed my heart. L'après-demain collectif, my dear French theatre group in Amsterdam! I'm so lucky we met and shared the same passion for drama, and all had a burning desire to play in French. Patrick, Morgane and Ferdinand, I'm so happy for this more-than-2-year-long adventure, and that our show came to life! From costume design to acting, directing, and producing, we took the 360 full-view on this "God of Carnage". I had a blast, and will keep the weirdest Tugela rehearsal memories with me for a long time! :) Along the way I was also so happy to meet your wonderful partners, Cristina and Filippo, and happy for all the raclette evenings and live-free dance sessions with us all. I'm also excited for possible new filming adventures with you Léa!

During these 4 years, I spent quite some time on the Thalys moving between Paris and Amsterdam. I have two home cities now, and I want to express all my love to my beautiful crew from Paris. Je vous aime à la folie. Chloé, je suis trop heureuse de te savoir à mes côtés aujourd'hui. Depuis les bancs de l'ENS et la fameuse L3/M1, nous sommes toujours restées proches (malheureusement pas toujours géographiquement, mais toujours dans le coeur). Tu es une amie très à l'écoute, fidèle et très sincère, et je suis heureuse qu'on ait pu faire la meilleure coloc du monde ensemble. Je chéris nos longs coups de téléphone et notre nouveau rituel de vacances estivales ensemble. Merci pour ton soutien bienveillant et encourageant pendant toute la durée de ma thèse. Lucie, chaque fois que je te vois, je suis inspirée et je me sens pleine d'énergie. Tu es une force de feu et tu gravis des montagnes avec détermination - j'ai tellement hâte de découvrir ton one woman show bientôt! J'ai toujours admiré ton courage de faire les choses même quand elles te faisaient peur, et je suis pleine de confiance pour tes projets actuels et à venir. Love you lots xxx Laure, ma bella chiqua! Nous partageons bien sûr un amour fou et brûlant pour D.D. qui nous a permis de nous rencontrer, mais aussi le même terre-terre de l'est Parisien, et surtout une vision commune de la valeur de l'amitié. Je suis tellement heureuse de t'avoir dans ma vie,

et incroyablement touchée d'avoir le VIP pyjama party treatment au 66 rue René Boulanger quand je viens à Paris. Suzanne, ma chérie. J'adore quand tu racontes l'histoire de notre rencontre, à la nuit blanche de Paris, en train de danser à cœur et bras ouverts toutes les deux. Tu es très précieuse dans ma vie et je suis heureuse d'avoir découvert tant de choses avec toi, depuis la ville de Toulouse au festival de l'Huma jusqu'à la couture de coussins. Tu es pleine de talents créatifs et une vraie geek passionnée quand tu plonges dans quelque chose. Je t'admire beaucoup, et j'adore la présence de tout un tas d'objets faits par toi dans ma maison. Chère Juliette, notre amitié date du lycée maintenant, et je suis heureuse de te retrouver au moins une fois par an pour les retrouvailles et la longue session de débrief des grands et petits événements de la vie. Je t'embrasse fort. Félicien, que de temps depuis nos premiers cours de L1 ensemble et nos soutenances de thèse maintenant! Je vous souhaite plein de bonheur à toi et à ta très chère Quiterie pour la plus belle des aventures qui vous attend bientôt. Je sais que vous serez formidables. Lénaïg, comme je suis contente d'avoir choisi de suivre le cours de dramaturgie de l'ENS! On s'est rencontrées peu de temps avant que je parte à Amsterdam, mais je me suis tout de suite sentie bien avec toi, et tellement vivante dans nos conversations sur la vie et la littérature. Les quelques jours à Berlin avec toi étaient formidables. Merci aussi à mes amis de la fac Elsa, Estelle, Hugo, Justine, Louis, Tim, Elia, et Philippe que j'ai moins vu ces dernières années, mais avec qui chaque retrouvaille est toujours un vrai plaisir. Je fais aussi des bisous à toute la dream team de Maisons-Alfort: Benjamin, Etienne, Tess et Fabien, Anne et Maxence, Antoine, et Cédric et Nicole. Merci pour votre accueil dans votre super bande d'amis.

There are two more friends across the world I would love to share my love with here. Ma chère Tanya, comme je suis heureuse de savoir que tu vas tenir cette thèse entre tes mains, et quelle émotion de penser que ma thèse va voyager jusqu'au Canada. Je suis heureuse de te savoir dans ma vie, et ça me touche de penser que tu as été la première à voir mon appartement à Amsterdam. Hope to see you soon dear. Dear Elisa, my sweet friend. It still makes me laugh so much that I didn't realise until after 6 months of knowing you that Antwerp was in fact no place else than "Anvers"... I'm grateful for all the great times we shared together, and for your presence at every single one of my housewarming parties. Sending you hugs.

None of this would have been possible without the beautiful, loving and caring support of my family since day 1.

Papa et maman, je sais que vous ne voulez que le meilleur pour moi. Vous m'avez toujours encouragé à donner le meilleur de moi-même et à progresser, tout en équilibrant le tout avec des vrais temps de vacances et en prenant soin de soi. Merci pour tous nos voyages en famille qui m'ont fait découvrir le monde, merci pour vos encouragements toujours présents, et merci de m'avoir enseigné qu'apprendre et comprendre rend libre! Je ne suis pas (encore?) sur les billboards à l'aéroport mais aujourd'hui votre grande petitou devient Docteur Mc Govern, so let's celebrate and let's go McGogos! Alice, ma (petite) soeur qui est déjà bien grande, et aussi une Dr Mc Gogo/ Dr Biboundé en chef! Je suis tellement fière de toi et de tous tes big steps, et je suis heureuse de te voir grandir et choisir une vie qui te passionne. Ton ambition et ton amour de faire les choses bien pour tes patients m'inspire, et j'ai vraiment hâte de visiter votre home sweet home à toi et Paul. Merci d'être ma partynymf sister d'amour. J'embrasse aussi Paul de tout mon coeur, tu fais partie de la family maintenant et j'ai tellement hâte de te montrer chez nous à Amsterdam!

Ma chère Mamie Coco, merci pour ta présence et ton amour à chacun de mes pas. Tu ne cesses de m'inspirer. Mon cher papi Paul, toi qui te souvient de la neige le jour où je suis née. Je te remercie pour l'ambition que tu as insufflé en moi, et pour la passion pour la politique dont j'ai hérité de toi. J'embrasse aussi très fort Françoise et j'ai hâte de célébrer avec vous 2 à Montpellier. Des gros bisous à mes cousines chéries Lyla et Pauline, et à mes oncles et tantes dont j'ai la chance d'être entourée aujourd'hui, Eudes, Elizabeth, Emmanuel et Sylviane.

My dear Granny and Grandad, I hold so much love for you both. Grandad, I'm so grateful for our time together when I was living in London, and for your love and support at every step. Granny, you will forever be in my heart. And lots more love to my whole English family! Your presence live and online today means the world to me. Many kisses to my cousins Katy, Josh, Alex, Ashleigh, Eve, Kyle, Bridget and Zack, and to my aunts and uncles Carmel and Tom, Hugh and Doreen, Clare and Bernie, and Marc and Sandra.

One last family loving note goes to the "Americans" of the family (some of whom I have had the chance to visit during my PhD conferences, and the others whom I hope to meet or see very soon again!): Richard, Ginny, Emilie, Andrew, Laszlo, Olive, Caroline, Annalise, Eskender, Jason and Korinna.

Je souhaite aussi remercier la famille de Lucas. Merci à Joëlle et Jean-Yves de m'avoir si bien accueilli parmi votre famille, et pour les nombreux séjours à l'Alpillonne où j'aime vous retrouver avec Gabriel, Gilberte, Laurence, Philip, Isabelle, Gilles, Aurélien, Hélène, Tristan, Elie, Victor, Anna, Rose et Alice. Votre présence à tous les deux pour ma défense de thèse me touche beaucoup.

Ces prochaines lignes sont pour ma meilleure amie. Ma Clémence d'amour, je remercie le ciel que nos chemins se soient croisés à cette pièce de théâtre. Et quel chemin depuis notre rencontre et nos 14 ans! Tu as vu toutes les phases et toutes les transitions, tous les doutes aussi, et t'avoir aujourd'hui à mes côtés me rappelle d'où je viens, car j'ai l'impression d'avoir grandi à tes côtés. Tu es un trésor et tu ne cesses de m'émerveiller. Merci d'avoir accepté d'être ma paranymphe aujourd'hui.

Ces dernières lignes sont pour mon amoureux et partenaire Lucas, que j'aime de tout mon coeur. Après Paris, Villejuif et Montréal, je suis tellement heureuse qu'on ait décidé de poser nos valises à Amsterdam pour cette nouvelle aventure ensemble. J'aime ta façon d'aimer la vie et j'aime notre quotidien. Merci pour tout ton amour et ton précieux soutien, et pour tous les innombrables bons plats que tu m'as mijoté pendant l'écriture de cette thèse -le monde est plus beau à tes côtés.

ABOUT THE AUTHOR

Lucie Mc Govern was born in Paris on December 28, 1993. After completing her high school studies in 2011, she wanted to keep on exploring multiple fields, and felt a strong curiosity for discovering how the world works, with a taste for multidisciplinary approaches. She obtained a double Bachelor's degree in Chemistry and in History, from the universities *Pierre et Marie Curie* and *La Sorbonne* in Paris, in 2014. During this double Bachelor's program, she spent one year at the University College of London.



Desiring to deepen her understanding of Chemistry, she continued her studies at the *Ecole Normale Supérieure*, in Paris. There, she specialised in Physical Chemistry and obtained her Masters jointly from the *Ecole Normale Supérieure* and from the university *Pierre et Marie Curie* in 2017, with a minor in History and Theory of Dramatical Arts. During this Masters, she completed two long research internships projects, at McGill university in Montréal, and at AMOLF in Amsterdam.

She further pursued as a volunteer in the government-agency of the *Agence Parisienne du Climat*, where her mission was to co-organize a Parisian-wide challenge for families to reduce their environmental footprint.

In 2018, she started her PhD in the Hybrid Solar Cells group under the supervision of Prof. Bruno Ehrler, where she worked on ion migration processes in perovskite solar cells. The results of these scientific investigations are presented in this thesis. Next to her thesis, she participated in the work's council international committee and in the Green Sustainability group of AMOLF.

Lucie also enjoys the theatre and has acted and co-directed in amateur plays in Paris, London and Amsterdam. During her PhD she collectively directed and played in "Le dieu du carnage" by Yasmina Réza, which was performed in December 2020.

